# AIR JET IMPINGEMENT FOR LEVITATION

by

JAMES HUBER

Presented to the Faculty of the Graduate School of

The University of Texas at Arlington in Partial Fulfillment

of the Requirements

for the Degree of

MASTER OF SCIENCE IN MECHANICAL ENGINEERING

THE UNIVERSITY OF TEXAS AT ARLINGTON

May 2006

ACKNOWLEDGEMENTS

I would like to extend special thanks to my supervising professor, Dr. Raul Fernandez. He is responsible for hiring me as a Graduate Research Assistant at the Automation and Robotics Research Institute (ARRI), where I was introduced to the topic of air jet impingement levitation. He acquired all the necessary equipment for testing and has spent countless hours reviewing impingement studies and assisting me in my analysis. His knowledge and insight has given me great direction.

Without the hard work and dedication of my predecessor at ARRI, Roberto Torres, who built many of the prototypes we tested in the course of this project, and my coworker Neel Chatterjee, who assisted in machining some of the necessary test equipment, my thesis work would not be possible.

My special thanks to Jimmy Dufinetz, Carlos Mandujano, Miguel Mata, and Brian Witkowski for their work in the senior design project that produced the prototype end effector tested in this paper. Their work is in large part responsible for my introduction to the air levitation project. Their project was directed by Dr. Robert Woods, who played a key role in the development of the levitation prototypes and also served on this thesis committee.

Finally, I would like to thank Dr. Kent Woods for being on the graduate committee and for his dedication to teaching ANSYS and finite element methods.

April 12, 2006

ABSTRACT

AIR JET IMPINGEMENT FOR LEVITATION

Publication No. _____

James Huber, M.S.

The University of Texas at Arlington, 2006

Supervising Professor: Dr. Raul Fernandez

Traditional part acquisition methods such as vacuum cups and robotic grippers do not meet the handling needs of truly fragile materials, because both of these methods require surface contact. An alternative to these traditional approaches is the use of air jet impingement for levitation. This technique confines impinged air to a thin disk above the target to form radial diffuser. The Bernoulli Effect causes a pressure difference between the fast-moving impinged air above the surface and ambient air below it. The net pressure difference is sufficient to lift objects weighing more than one kilogram using standard shop air. This method of lifting is self-stabilizing and the impinged surface is contacted only by air.

The analytical, numerical, and experimental results are presented for an end effector prototype constructed to test the impingement lift effect. A first-order

analytical approximation is given based on convergent-divergent supersonic flow incorporating shockwave energy losses. A numerical simulation of the end effector was obtained using the computational fluid dynamic software, ANSYS CFX. The results show transonic air flow and the formation of large stationary structures. Two experiments were conducted to provide quantitative measurements of the actual pressure profiles realized and to relate the net force of the impinging jet as a function of the distance from the surface. The data shows a linear relationship between the input pressure and the maximum net lifting force. These experiments prove that a nozzle flange fixture powered by compressed air can be implemented as a material handling solution.

TABLE OF CONTENTS

LIST OF ILLUSTRATIONS

LIST OF TABLES

Table Page

# CHAPTER 1

# INTRODUCTION

## 1.1 Need for Advanced Handling

Modern invention requires advanced technologies, and these technologies require sophisticated components and processing as an integral part of functionality and design. Each new device requires special procedures to facilitate efficient production, and the development of automated handling methods and techniques is necessary for affordable manufacture. Handling techniques should allow diverse implementation without costly custom fixture design, and gas jet impingement offers a unique solution to these handling requirements. It is the purpose of this research to provide an analytical, numerical, and experimental foundation to the understanding and use of this physical effect.

### *1.1.1 Wafer Handling Requirements*

The use of fragile wafer structures has become more common in recent research activities, especially related to the electronics industry. Typically made from very thin slices of silicon-based compounds, wafers can be more brittle than glass and sensitive to contamination. The useful potential of a silicon wafer is typically determined by its surface area, and not by its thickness. Wafers are sliced from a large silicon ingot, and it is desirable to minimize the wafer thickness to increase yield. Wafers can currently be cut as thin as 100 microns—the average width of a human hair. Unfortunately, these

ultra-thin wafers have greatly increased potential for fracture throughout the various processing steps in manufacturing. Large scale production must accommodate the gentlest of handling techniques.

One of the ways wafer stress is reduced in the treatment process is by using a conveyor system to gently carry the wafers through the required stations. This efficiently moves the wafers through etching and coating treatment sites, but it is still necessary to load and unload the wafers from the conveyor. An appropriate fixture attached to an industrial robotic arm must pick and place the wafers without causing contamination or excessive stress. It must also be able to stack the wafers for shipment or storage. A minimal-contact method is required at these transfer points. Air levitation is a possible solution to sensitive transport.

Air levitation is accomplished by creating a pressure difference between the top and bottom surfaces of the wafer. This pressure difference causes a net upwards force to act on the wafer, supported by the pressurized air beneath it. This allows minimal-contact acquisition and can be achieved in several ways. One method is to supply compressed air from below the wafer. This creates a region of higher pressure air beneath the wafer and results in the wafer being forced away from the nozzle. This is commonly called an air bearing. Air bearings provide a safe and gentle method of transfer, but require clearance beneath the wafer. While resting on a conveyor, a wafer does not have clearance for an air bearing to go beneath it, and further, an air bearing cannot remove wafers from a stack. Air bearing style lifting does not provide an acceptable solution.

Wafer production requires minimal contact lifting from the top side of the wafer, and a contact free method is preferred. This is not possible with vacuum cups because the rubber cups must touch the wafer surface, but it is possible with confined jet impingement. When a confined jet impinges on a wafer at narrow range, the air will rush out to the edges of the confining surfaces. This radial diffuser geometry creates a region of low pressure, which, contrary to intuition, can provide a sufficient net pressure difference to lift a wafer. The net force will cause the wafer to approach the upper confining surface until it stabilizes at the point where the net lifting force is equal to the wafer's weight. The natural self-stabilization allows the same fixture to work for wafers of different sizes and weights. This method of lifting meets the demands for wafer transfer and has low sensitivity to wafer size, weight, or thickness.

*1.1.2 Large Object Handling*

Another challenge for automation is the handling of oversized objects. Sheets of cardboard, for example, are difficult to pick up with a mechanical gripper. Contact is allowed, but a gripper cannot easily separate sheets from a stack and is limited to grasping at the edges. A traditional vacuum pump would also fail in applications with excessive dust, because the pump filters would clog. A similar case exists for sheets of glass, tiles, thin sheets of metal, plastic panels, etc. Automated stacking for these large, planar objects can be difficult and require custom-designed equipment. A single confined impinging jet operated with standard shop compressed air can create vacuum sufficient to lift over a kilogram without costly vacuum accessories. Additionally, one end effector can pick up any planar object without modification. For planar objects, jet

impingement is a powerful alternative to conventional vacuum and mechanical gripping approaches.

## 1.2 Impingement Applications

Air jet impingement is widely used for heat transfer and a great number of studies have been published describing the associated Reynolds and Nusselt number values. Most applications have been developed for heating and cooling operations, but STOVL aircraft demonstrate impingement used for thrust. The use of jet impingement for object levitation other than thrust, however, has not been widely used. The few exceptions typically rely on impingement from beneath a surface in the fashion of an air bearing.

One example of a commercial use of air jet impingement for levitation is the large continuous dying oven manufactured by the J. Rostron Engineering Corporation [1]. This oven impinges hot air from above and below the surface of the processed material for the purpose of drying or heat treating the material. The lower set of jets is intended to act as an air bearing and prevent excessive contact, and the upper set of jets is intended to increase convection. This design uses impinging jets for levitation, but only in the traditional method with the jets below the object's surface.

Though not strictly by impingement, certain techniques for paper handling make use of jets of air and the Bernoulli Effect to separate sheets of paper and move the pages into position. These devices typically use a jet of air blown across the surface of the page, rather than down onto it, to create an area of low pressure. The use of the Bernoulli Effect has similar results as the jet impingement method described in this

paper, but the technique is quite different and the potential vacuum generation is greatly reduced.

## 1.3 Patent Review

Because the use of air jet impingement for levitation is so limited, there is very little research published explaining the subject. Despite the deficiency of analytical investigation, however, several devices have been developed that use the impingement technique for levitation. For this reason, it is informative to look into the history of impingement related patents in order to understand the historical development of the concept (a review of the analytical literature is presented in the following chapter).

One of the first fixtures to generate lift through the Bernoulli Effect is US patent 2905768 (1959), an air head that uses both positive and negative pressure ports to draw air across the top of a surface. The center port expels pressurized air through a series of holes and two adjacent ports apply vacuum to receive air. The purpose of this device is to bring a magnetic tape very close to a recording head while maintaining a small gap. The vacuum brings the tape close, while the positive pressure impingement maintains a finite gap width. According to the patent, the gap can be modified by adjusting the positive pressure at the center port. The device does not rely on impingement for lift—the patent states that the vacuum ports provide lift—but it combines Bernoulli lift and air bearing effects, similar to the impingement lift concept.

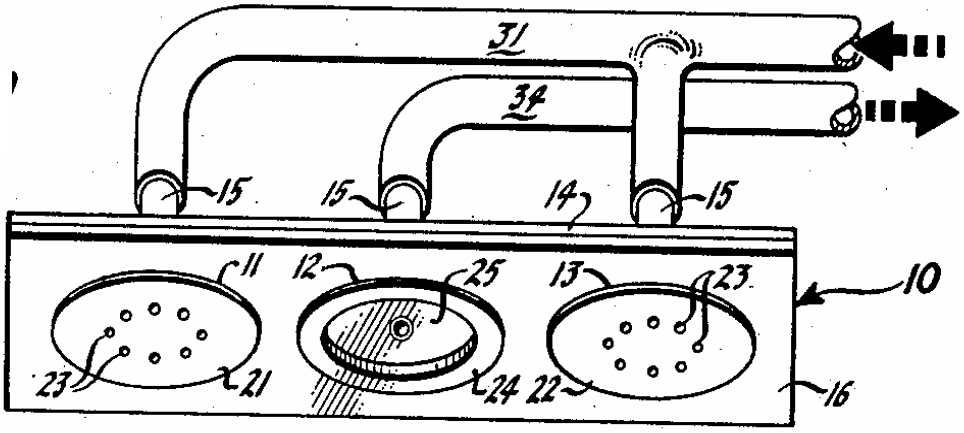


Figure 1.1 Excerpt from U.S. Patent 2905768

A patent for a pneumatic sheet separator was approved in 1964, claiming that the device may be operated with either positive or negative air pressure to the nozzle. Any pressure difference, whether positive or negative, will result in the development of fluid flow across the surface of the paper. Because of Bernoulli's principle the fluid stream moving at higher velocity will exert less pressure on its surroundings and create lift. Similar prototypes have been successfully developed for use with silicon wafers. Non-impingement or minimal-impingement devices such as this can generate lift, but require more complex fixtures to preclude imparting a horizontal velocity to the wafer.

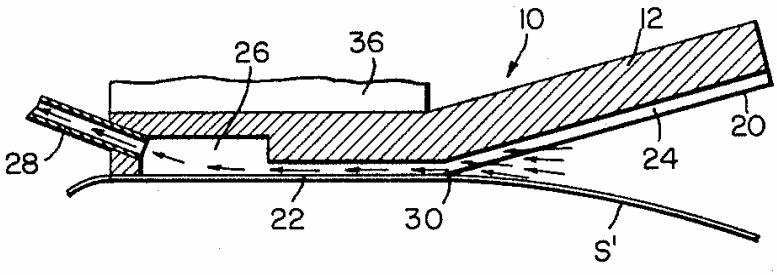


Figure 1.2 Excerpt from U.S. Patent 3158367

Another early pickup head was patented in 1965 and was named “Suction Pickup with Air Bearing”. This device uses both positive and negative pressure sources as described above, again stating that lift is generated by the negative pressure sources only. Similarly, the positive pressure source is intended to repel the target as an air bearing and prevent contact between the pickup head and the target surface. The patent writer admits the inefficiency and does not mention the presence of Bernoulli lift, leaving the reader to judge its contribution. Air is impinged in this device, but not for the purpose of levitation. It meets the demands of impingement lift, but is inefficient at doing so.

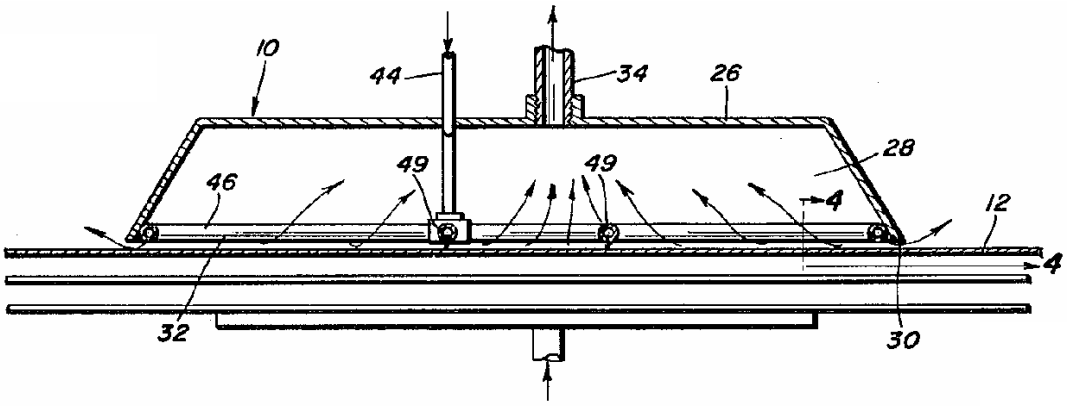


Figure 1.3 Excerpt from U.S. Patent 3220723

A centrally ported Bernoulli style lifter was patented by R. G. Olsson. This device makes claims of contact-free lifting by the use of pressurized air flowing over the surface, but it does not impinge the air directly onto the surface. The air is redirected outward by a small centrally attached disc. This allows redirection of the air

without impinging the target surface. It is another form of a contact-free impingement lift device.

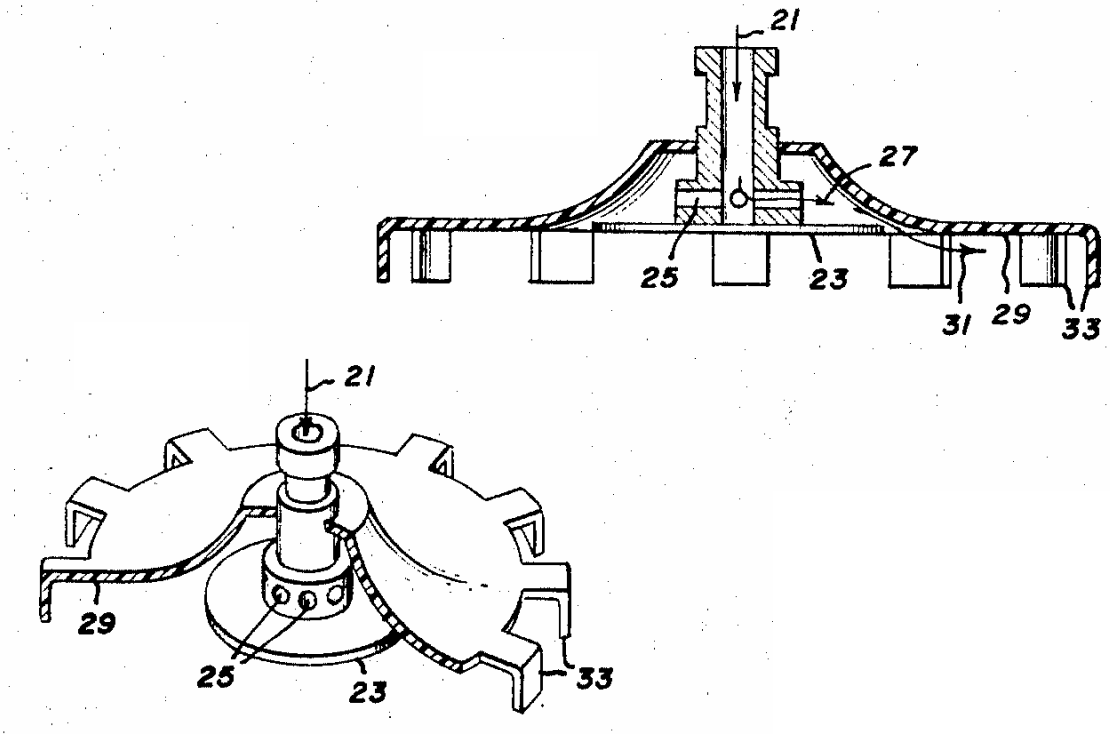


Figure 1.4 Excerpts from U.S. Patent 3438668

Following the previous patent application by only a month, W. K. Mammel patented a true impingement lift device in 1969. This “Pressurized Fluid Pickup” utilizes a valve-controlled pressurized impingement jet and uses only the impingement properties to generate lift. The patent suggests the use of this device for the handling of silicon wafers, and describes the Bernoulli and air bearing effects described in this

paper. This is one of the first authentic uses of air jet impingement for levitation purposes.

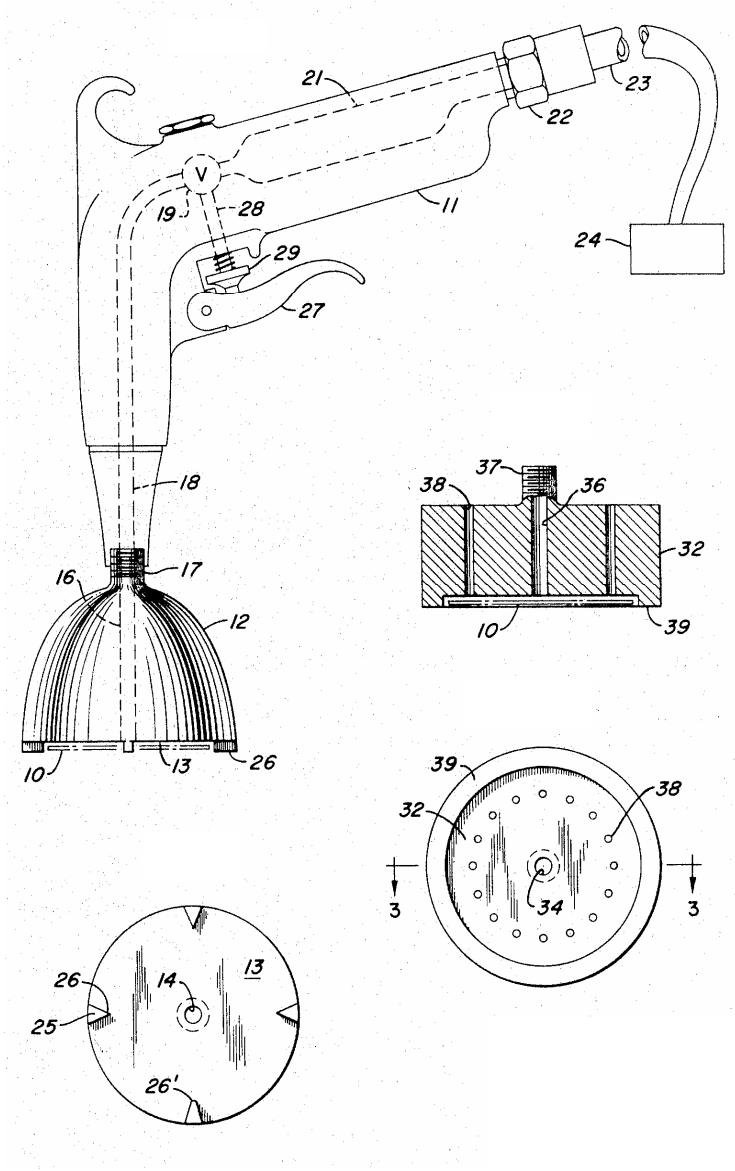


Figure 1.5 Excerpts from U.S. Patent 3466079

Another variation on the Bernoulli pickup head, also published in 1969, utilizes jet impingement with fluidic logic type gate instead of traditional valve. Mechanical

stops are placed around the edges of the device to prohibit the wafer from slipping off of the impingement surface. The patent figures depict a simplified nozzle and flange design.

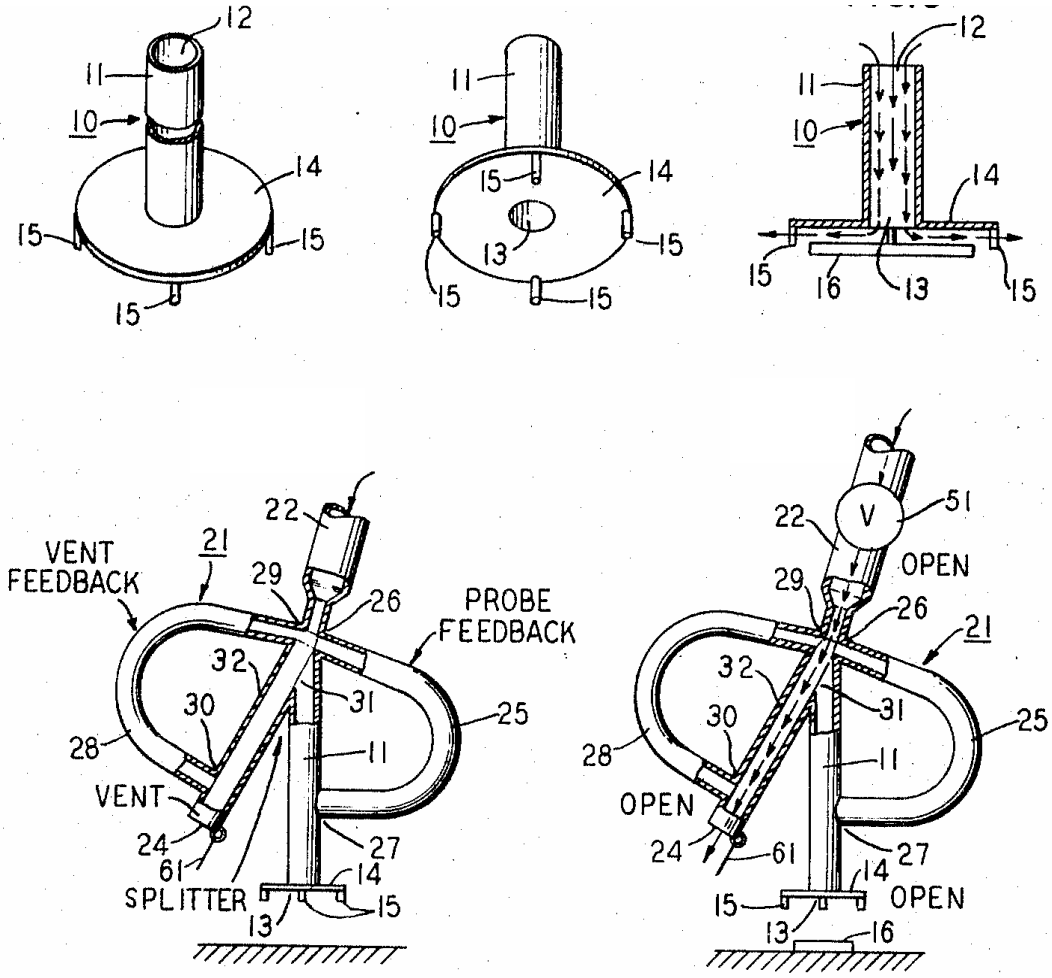


Figure 1.6 Excerpts from U.S. Patent 3425736

Below are two Bernoulli pickup head variations. The first is referenced to moving glass sheets, but the variations of the heads are similar to other pickup heads

intended for moving all planar objects. It is one of the most recent patents on the subject, approved in 2003. The second patent uses a series of fringes on the outer portion of the flange to reduce noise. At high pressure an impingement device can cause a whistling sound in the range of 90dB. This device attempts to minimize the unwanted noise.

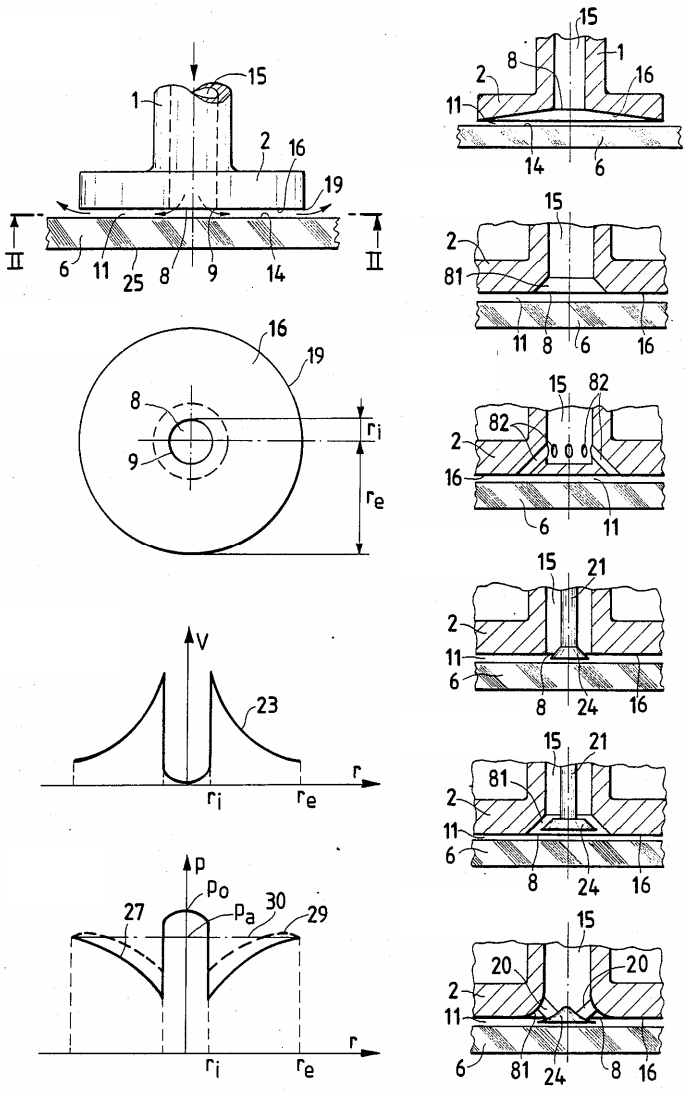


Figure 1.7 Excerpts from U.S. Patent 4921520

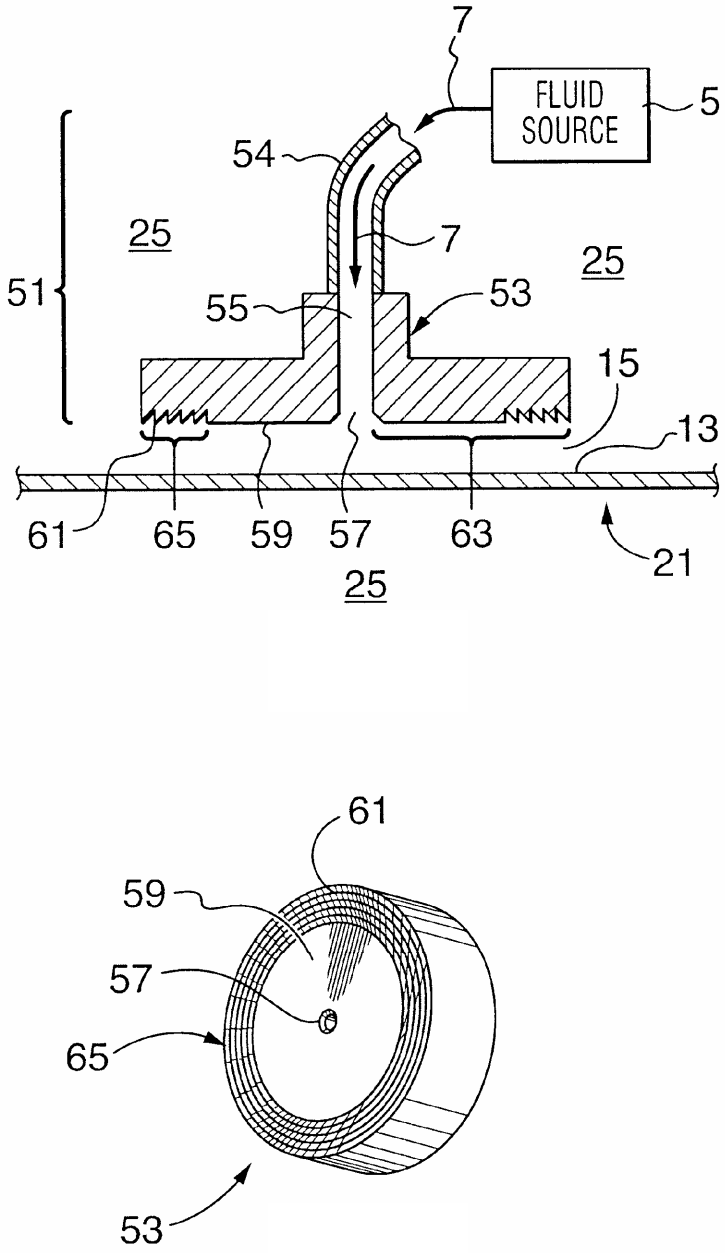


Figure 1.8 Excerpts from U.S. Patent 6601888

A 1991 patent is of great interest because it includes the pressure profiles for several variations of the impingement nozzle design. This is very similar to the data acquired in the later portion of the paper, and is useful for comparison.

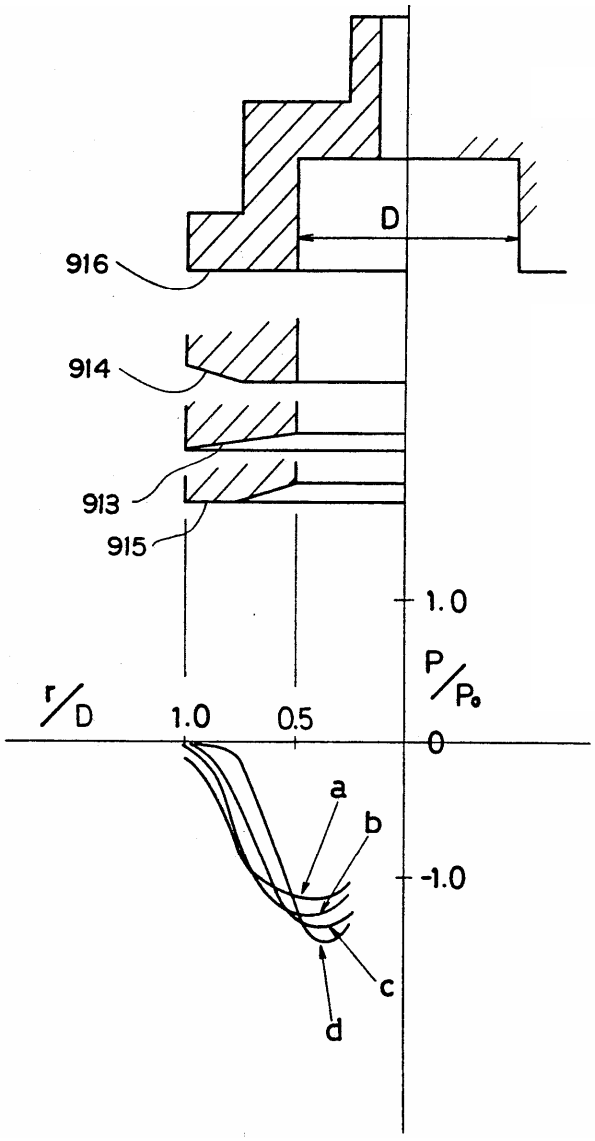


Figure 1.9 Excerpt from U.S. Patent 5067762

Despite the invention of air jet impingement levitation devices, there is little research describing the mechanisms by which this physical effect is possible. In addition to the lack of explanation, there is little quantitative measurement of the potential of this technique. The goal of this research is to present analytical, numerical, and experimental approaches to explain and measure the impingement lift effect that has already been implemented in prior patented devices.

# CHAPTER 2

# LITERATURE REVIEW

There are two common divisions of fluid dynamic studies available: studies involving generally incompressible fluids—often water or oil, and studies involving highly compressible fluids—typically gases such as air, nitrogen, etc. This division is made because the effects of compressibility have a large effect on the fluid's behavior. Similarly, jet studies can be separated into free jet studies and impingement jet studies, depending on whether the jet is positioned to strike a surface. There are two types of impingement jet studies: free impingement and confined impingement. Both types position the jet to strike a surface, but confined impingement requires a bounding surface parallel to the impinged surface with a small distance between. The bounding plate tends to cause the fluid to flow across the impingement plate for a greater distance.

This paper studies the effects of a well-formed compressible air jet impinged at close range into a confined planar volume. It is useful to study compressible flow and shockwave interaction to describe the behavior of supersonic jets. It is also useful to study other impingement research, even outside the compressible, supersonic, confined impingement category. These studies establish basic principles and identify common terminology.

## 2.1 Relevant Compressible Flow Studies

The analysis of jet impingement has at its foundation certain fundamental laws of fluid mechanics. Hydrodynamics relates specifically to the dynamics of incompressible fluids, but incompressible theory forms the basis of compressible fluid theory as well. One of the most important milestones in Hydrodynamics came in 1738 when Daniel Bernoulli published the work *Hydrodynamica* [2]. In this text he presented a hypothesis that has become known as the Bernoulli principle. This principle is central to the study of fluid dynamics, and foundational to the success of impingement levitation.

Another milestone in fluid dynamics came from Gustave De Laval. De Laval is responsible for the discovery of the supersonic nozzle, and the primary investigations in supersonic flow. Since De Laval's discovery, there have been many studies examining the thermodynamic relationships of compressible fluid flow. These basic principles are textbook material, including supersonic flow and normal shockwave calculation techniques [3-5]. Research also describes how shockwaves interact when encountering other shockwaves or rigid surfaces [6]. These texts provide reliable analytical derivation of compressible flow characteristics and shockwave theory.

The study of air jet impingement is closely related to supersonic jets flow. One such study, by Handa, Masuda, and Matsuo, details the normal shockwave interaction just beyond a constriction in a contained channel [7]. Their research highlights the presence of reflected shocks and multiple normal shockwaves. It also points out the location of a discontinuity between thermodynamic properties, called the *slip line*, as

shown in the figure below. The slip line marks the border of the most intense portion of the jet, the *jet core*. Similar fluid effects are observed in air jet impingement flow.

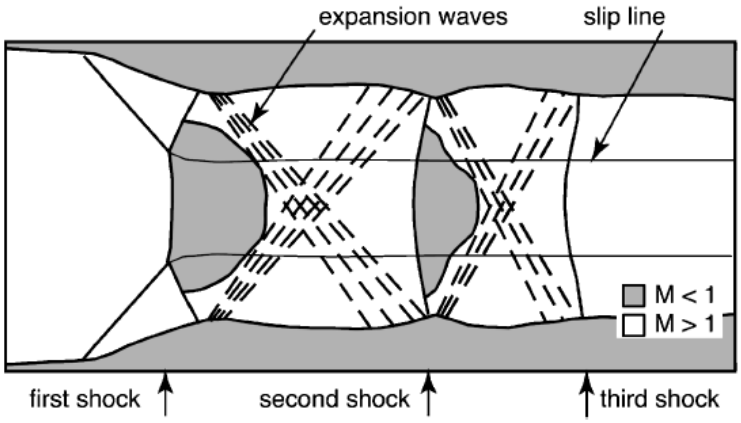


Figure 2.1 Interaction of shockwaves in a channel [7]

The interaction of shockwaves following a free jet is studied in a paper by Michael Norman and Karl-Heinz Winkler [8]. This paper describes the thermodynamic relation of the incident and reflected shocks, and explains the behavior of the triple shock point. A confined impinging jet behaves similar to a free jet near the nozzle exit, and the crisscrossing pattern of shockwaves is applicable in both cases.

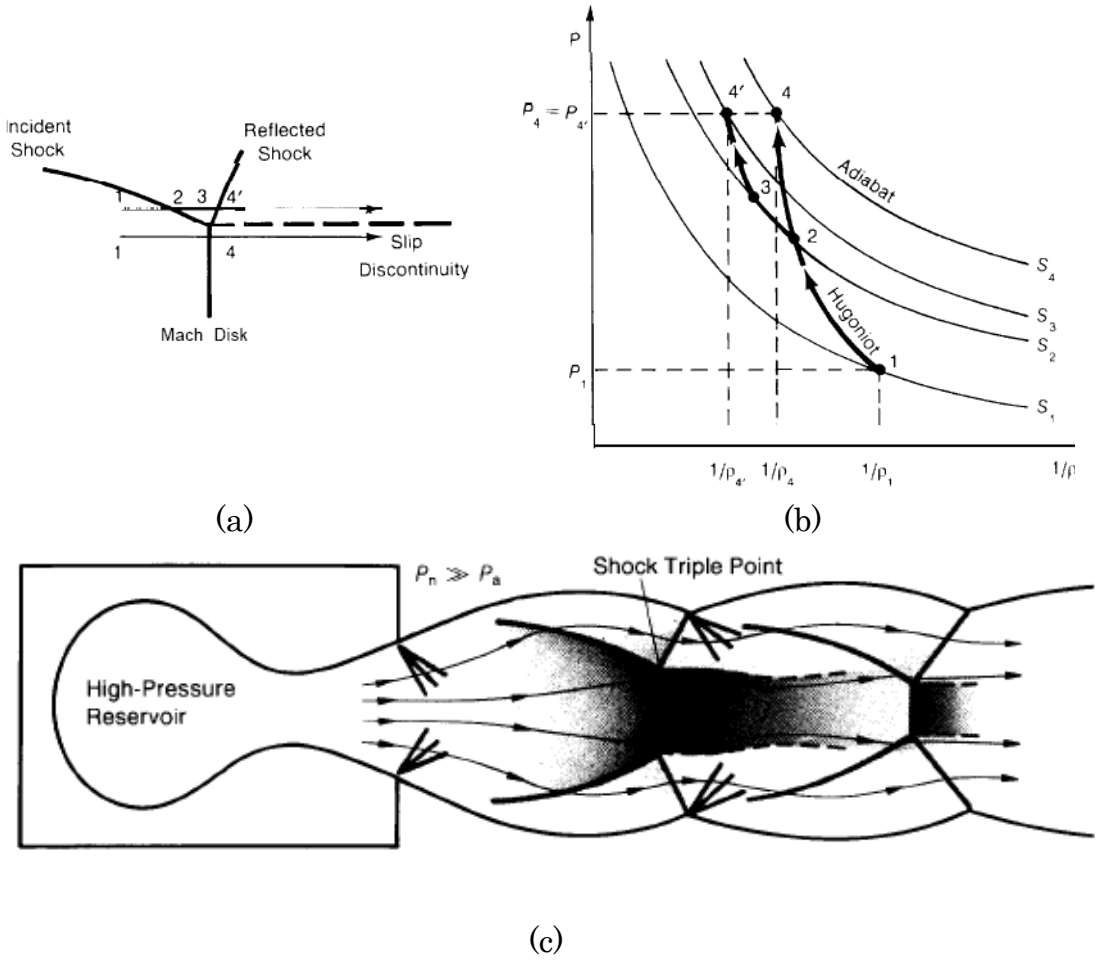


Figure 2.2 Interaction of shockwaves in a free jet; (a) shock triple point (b) thermodynamic history (c) free jet shock interaction [8]

## 2.2 Relevant Impingement Studies

The majority of the existing research in jet impingement is dedicated to the effects of heat transfer, rather than levitation. Osama Al-aqui, for instance, investigates the heat transfer at the walls of a narrow channel with jet impingement and cross flow [9]. Another typical heat transfer study is the one conducted by Angioletti, Nino, and Ruocco, who used Particle Image Velocimetry in conjunction with CFD numerical code to study the effects a turbulent impinging jet [10]. These types of impingement studies

are not directly useful to explain levitation by impingement because they do not report the distribution of pressure on the impingement surface.

There is a more closely related study that investigates a similar confined impingement case by computing a mathematical model [11]. The result shows large scale eddy formation and the development of contrasting impingement activity regions (see figure 2.3 below). This study covers confined compressible impingement, but only reports the heat transfer effects.

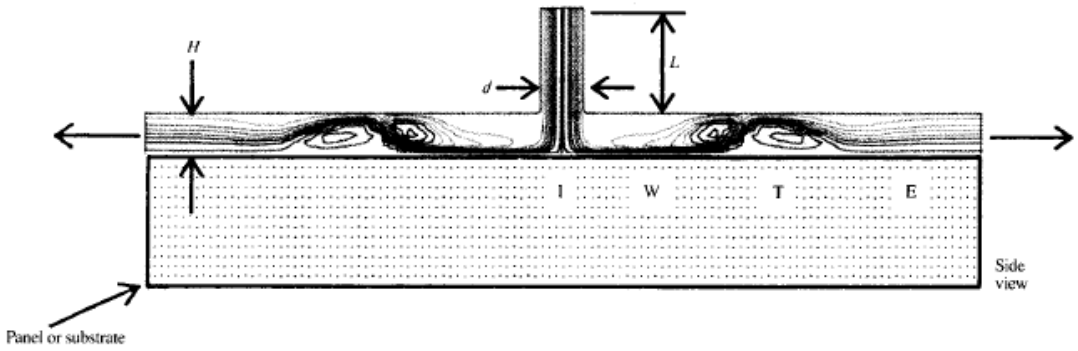


Figure 2.3 Numerical study of a confined impinging jet by Moreno, Katyl, Jones, and Moschak, where I = Impingement region, W = Wall Jet region, T = Transition region, and E = Established flow region [11].

Another two studies have been identified which give results supporting impingement for levitation, but neither expressly declares levitation as an objective. The first study reports the coefficient of pressure for various Reynolds numbers at an array of nozzle diameter to plate ratios [12]. This non-dimensionalized data represents a pressure profile similar to the type collected in the research presented herein (see

figure 2.4 below). This data records the existence of a vacuum region from positive pressure impingement for several parameter combinations. The paper does not mention, however, that this vacuum is significant enough to overcome the positive impingement pressure and to levitate objects. The author concludes that the sub-atmospheric region strengthens for increasing Reynolds numbers and decreasing nozzle to plate ratios. The second study records a similar profile, though by numerical simulation only, and also does not indicate any levitation effects [13]

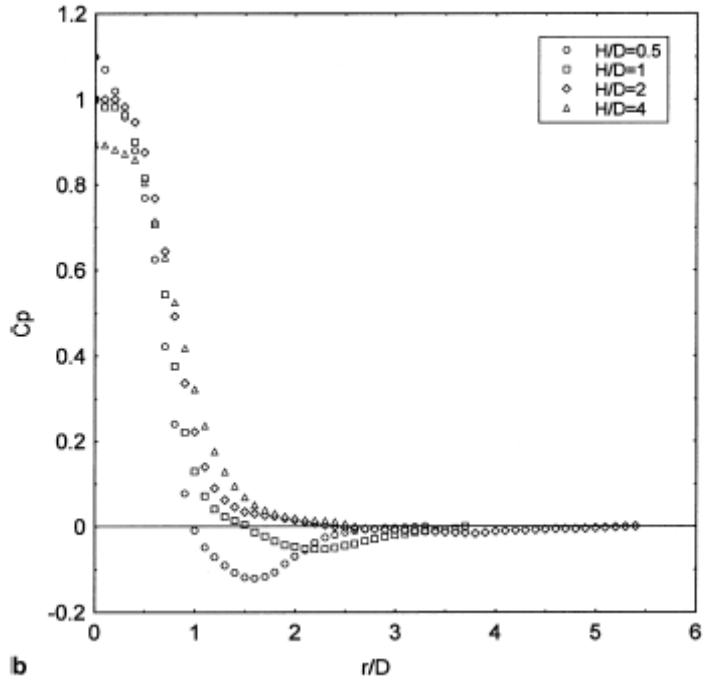


Figure 2.4 Coefficient of Pressure from confined air jet impingement [12]

Coleman Donaldson and Richard Snedeker studied three types of impinging jets, in various configurations [14]. Based on the ratio of atmospheric to inlet pressure, air jets were classified as subsonic, moderately under-expanded, and highly under-

expanded, for respective $p^{\infty}/p^{0}$ pressure ratios of 0.800, 0.372, and 0.148. The jets were impinged onto a variety of surfaces, including a flat plate. These pressure ratios were chosen for comparison in this paper's flat plate experiment. This study also confirms the existence of vacuum development from impingement and does not explore the use of this vacuum for levitation purposes.

The last paper to review describes the effects of an unconfined supersonic impinging jet [15]. This numerical study provides the best representation of what happens to the impinging jet, highlighted in figure 2.5. The *impingement bubble* is described as the region of recompression on the impinging surface immediately below the impinging jet. This can be seen in figure 2.5 (a) by the lines separating the red and blue Mach areas at the center of the impinging jet. The triple point mentioned above is also notated, seen in figure 2.5 (b). This study is particularly useful for estimating the position of the shockwaves in the case of air jet impingement at close range. Though this study offers a thorough look at the flow effects of a supersonic impinging jet, there is still no indication in the research that this jet would actually attract the impinging surface toward the jet.

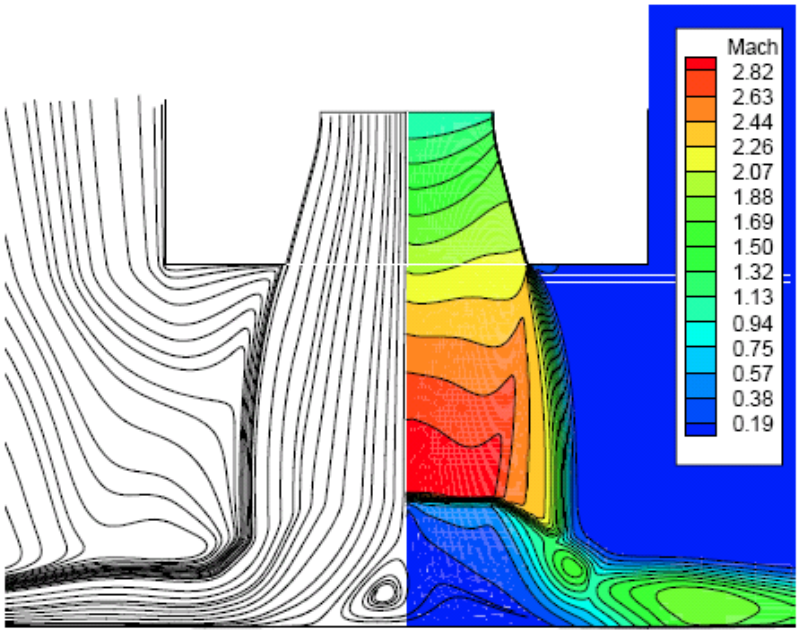


(a)

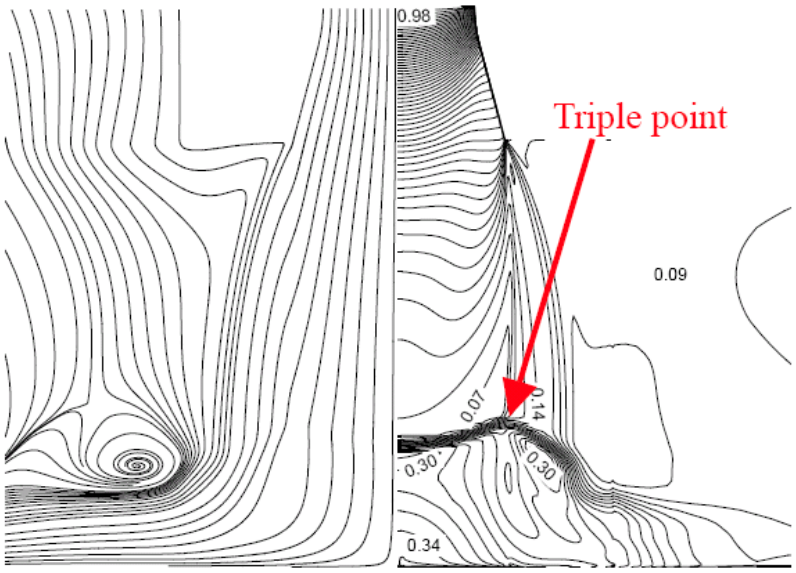


(b)

Figure 2.5 Velocity streamlines and Mach contours illustrating (a) the impingement bubble and (b) the triple point [15]

## 2.3 Research Objective

Despite the large body of research concerning jet impingement, there is little relevant information describing its use for object levitation. It is the object of this research to explain the mechanism by which air jet impingement for levitation is possible. It is also the object of this research to provide quantitative data about the pressure profile produced from confined air jet impingement and its useful net effect. This will be achieved through analysis using compressible flow theory, through a numerical model executed in ANSYS CFX software, and through two experiments using an impingement prototype.

The analytical analysis will show a first-order analytical approximation based on convergent-divergent supersonic flow incorporating shockwave energy losses. The CFD results will reveal transonic air flow and the formation of large stationary structures. The experimental data will document the pressure profile and justify a linear relationship between the input pressure and the maximum net lifting force. These experiments will demonstrate how a nozzle flange fixture powered by compressed air can be implemented as a material handling solution.

# CHAPTER 3

# ANALYTICAL APPROXIMATIONS

Closed-form analytical solutions are difficult to obtain in all but the most idealized fluid dynamics problems. Compressible fluid flow problems present an even greater challenge because of thermodynamic effects. Despite this complexity, some elementary mathematical modeling may be used to explain the phenomenon of impingement levitation. The author has not found such modeling in impingement literature, and one must rely on fluid textbooks to gain insight. In order to justify the mechanism of impingement levitation a model is developed to approximate the flow and yield a first-order prediction of pressure distribution based on first principles.

## 3.1 Review of Compressible Flow

There are several relationships to consider when choosing an analytical approach. The fluid is air, which is highly compressible, and calculations must reflect the compressibility to allow the possibility of vacuum. Standard control volume guidelines apply, including conservation of mass, conservation of momentum, conservation of energy. The ideal gas relations apply, based on the prevailing pressures and temperatures.

The Bernoulli principle applies to all fluids, and explains that as a fluid's speed increases, the pressure it exerts on the surrounding medium decreases. Accordingly, fast moving fluid above a surface will apply less pressure than the slow moving fluid

below the same surface. The result is a net unbalanced force normal to the surface in the direction of the fast moving fluid. Similarly, air can be forced to travel fast across the top side of a wafer and the wafer will be lifted by the ambient air underneath. The creation of a pressure difference in this way is called Bernoulli lift. The equation for calculation of Bernoulli lift for incompressible fluid is shown below [3].

$$\int \frac{dp}{\rho} + \frac{V^2}{2} + gz = \textit{constant along a streamline} \qquad (3.1)$$

One important fluid property is the measure of the speed at which a compression wave will travel through it, called its sonic velocity. The speed of sound for a particular fluid, *C*, is determined by equation 3.2, where *k* is the fluid's specific heat ratio, *R* is the real gas constant, and *T* is the relative temperature of the fluid. The Mach number is a ratio of the velocity of the fluid to the speed of sound in the fluid, as shown in equation 3.3.

$$C = \sqrt{kRT} \qquad (3.2)$$

$$M = \frac{V}{C} \qquad (3.3)$$

It is important to be familiar with the terminology in compressible flow calculation. A *static* or *relative* property refers to the measurement of that property at

any specific point in the flow. A *stagnation* or *total* property refers to the particular property's energy plus whatever additional energy would be contributed from the fluid's kinetic energy should it be stopped. Air moving at 100m/s with a relative temperature of 300K would have a total temperature of 305K, because if it were stopped it would recompress slightly and by the ideal gas law the temperature would increase. The relative properties can be determined in relation to the total properties based upon the fluid's velocity (converted to Mach number) and the compressibility of the fluid. The equations for determining the relative pressure, temperature, and density are shown below.

$$\frac{P}{P_o} = \left[ \frac{1}{1 + \left( \frac{k-1}{2} \right) Ma^2} \right]^{\frac{k}{k-1}} \tag{3.4}$$

$$\frac{\rho}{\rho_o} = \left[ \frac{1}{1 + \left( \frac{k-1}{2} \right) Ma^2} \right]^{\frac{1}{k-1}} \tag{3.5}$$

$$\frac{T}{T_o} = \left[ \frac{1}{1 + \left( \frac{k-1}{2} \right) Ma} \right] \tag{3.6}$$

*3.1.1 Laval Nozzle Theory*

In 1897 Gustav De Laval noticed that the efficiency of steam turbine was increased when the steam first passed through a small constriction in the nozzle, and this phenomenon prompted further experiments that led to the discovery of supersonic flow. Supersonic flow occurs in air when the ratio of outlet pressure to inlet pressure is below 0.528. When air flows through a properly shaped converging nozzle it will be isentropically compressed and will accelerate to the speed of sound. The narrowest region, called the throat, will always be exactly sonic. Past the throat, in the diverging portion of the nozzle, the air will continue to accelerate above sonic velocity. De Laval's research explains the breakdown of Bernoulli's principle in a diverging throat because it explains that the compressible fluid is expanding as it accelerates [3].

Laval nozzle calculation is based on the minimum cross-sectional area in the nozzle, called the *critical area* and designated by $A^*$. The *area ratio* is the ratio of each cross section's area to the critical area. For a given Mach number, the area ratio is calculated by equation 3.7 below. A table showing the thermodynamic properties for one-dimensional isentropic compressible flow based on area ratios is shown in Appendix B.

$$\frac{A}{A^*} = \left[ \frac{1 + \left( \frac{k-1}{2} \right) Ma^2}{1 + \left( \frac{k-1}{2} \right)} \right]^{\frac{k+1}{2(k-1)}} \tag{3.7}$$

As noted above in equations 3.4 through 3.7, all of the properties of the flow through the nozzle are a function of the Mach number. Once the velocity and speed of sound are known, the other properties can be directly determined. In a typical Laval nozzle problem, the area profile and the inlet conditions are given. The area profile is calculated by dividing each cross-sectional area by the critical area at the throat. The Mach number can be calculated based upon the area ratio. Once the Mach number is known all the other thermodynamic properties can be solved for at every position in the nozzle. This is the typical method of calculation for supersonic nozzles.

*3.1.2 Review of Normal Shockwave Theory*

When the supersonic air encounters a region of higher pressure it will begin to pile up, forming what is known as a shockwave. A shockwave is an area of extreme turbulence and mixing, where fast moving supersonic air will be re-pressurized and will continue flowing at subsonic velocity. Figure 3.1 illustrates this phenomenon. Shockwaves are located at the intersection of the Fanno and Rayleigh lines, and cause a rise in entropy of the gas [3].

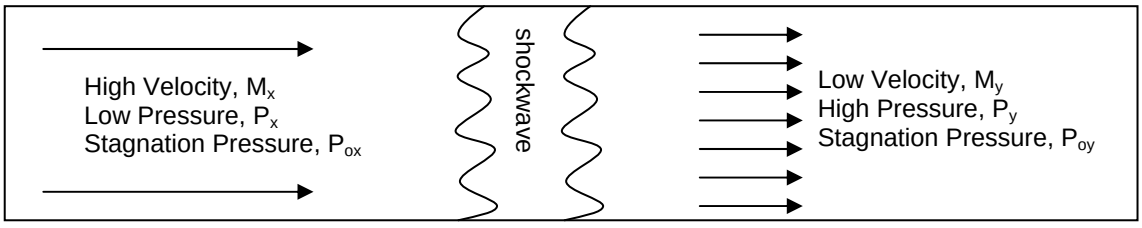


Figure 3.1 Shockwave schematic

Calculation of properties before and after a shockwave is widely agreed upon and techniques are found in most fluid mechanics texts. The thermodynamic properties are identified by the subscript *x* before entering the shockwave and by the subscript *y* after the shockwave. Variables with the subscript *0* refer to the stagnation property and variables without the subscript *0* refer to the relative property. For a normal shockwave, the Mach number after the shockwave, $M_y$, is a function of the Mach number entering the shockwave. All the other properties are a function of these two values. The typical normal shockwave equations are shown below.

$$M_y = \sqrt{\frac{M_x^{\,2} + 2/(k-1)}{2M_x^{\,2}k/(k-1) - 1}} \tag{3.8}$$

$$\frac{P_{0y}}{P_{0x}} = \frac{M_x}{M_y}\left[\frac{1 + M_y^{\,2}(k-1)/2}{1 + M_x^{\,2}(k-1)/2}\right]^{\frac{(k+1)}{[2(k-1)]}} \tag{3.9}$$

$$\frac{P_y}{P_x} = \frac{1 + kM_x^{\,2}}{1 + kM_y^{\,2}} \tag{3.10}$$

$$\frac{T_y}{T_x} = \frac{1 + M_x^{\,2}(k-1)/2}{1 + M_y^{\,2}(k-1)/2} \tag{3.11}$$

$$\frac{\rho_y}{\rho_x} = \frac{Py/Px}{Ty/Tx} \tag{3.12}$$

## 3.2 Boundary Conditions and Assumptions

There are several boundary conditions that must be accounted for in the air jet impingement problem. The most important plenum inlet condition is the stagnation pressure. This can be calculated from the relative pressure, the temperature, and the velocity of the fluid. The inlet temperature is assumed to be room temperature. Assuming a sufficiently large inlet, the fluid has zero velocity there, making the relative inlet pressure equal to the stagnation pressure. Prototype testing reveals that the air exits the gap between the flange and the impingement surface at very low velocity. This implies that there must be some stagnation pressure loss between the inlet and the outlet. At inlet/atmospheric pressure ratios above three to four, stagnation pressure losses approach 75%. This loss is assumed to be associated with the formation of stationary shockwaves.

The geometry of the fixture is known, and the gap width can be specified. In order to simplify the calculation of energy transfer, the adiabatic boundary condition is applied at the fixture wall. Heat transfer is possible, but it is not expected to produce a significant effect on the outcome of the solution. Traditional steady-flow conservation of mass equations apply.

## 3.3 Analytical Impingement Model

An air jet impingement fixture is similar to a Laval nozzle (see figure 3.2 below), where the cylindrically diverging portion of the nozzle is replaced with a radial disk diffuser. At sufficient inlet pressure, the air will reach sonic velocity at the throat and become supersonic at the nozzle exit just before impinging onto the target surface

below. Upon impingement the air will be redirected radially outwards. The diverging air will have velocity sufficient to drop the relative pressure below atmospheric level, thus creating a region of vacuum.

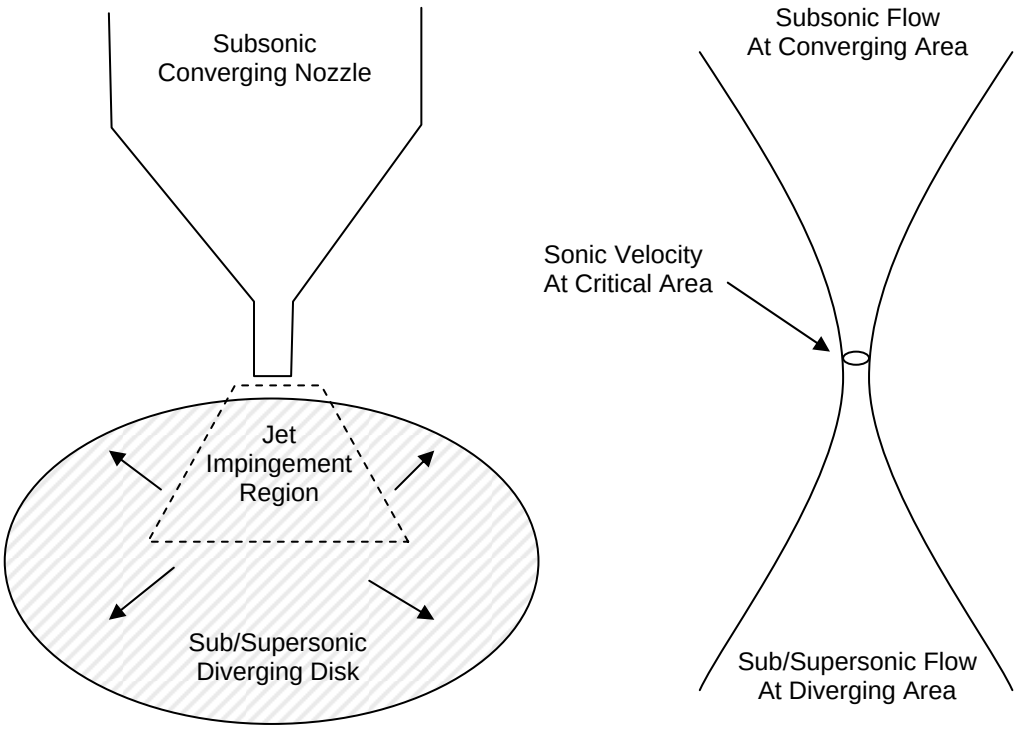


Figure 3.2 Comparison of impingement nozzle to Laval nozzle

There are two places where a shockwave might form. The first place is just past the nozzle throat, directly above the area of impingement. A shock disk in this location decelerates and recompresses the air to cause a small area of high pressure in the center of the impingement region. This *impingement bubble*, as named by Kim and Park [15], yields an accurate impingement pressure, but it does not entirely account for the loss of total pressure between the inlet and the outlet.

Outside the impingement bubble the flow reaccelerates through the *jet impingement throat*, again reaching supersonic velocity. This effect is produced by the pressurized air rushing out from the impingement center and simultaneously being forced down by the momentum of the impinging jet. The throat forms a disk, and though the disk height remains constant, the cross-sectional area will increase with radial position, allowing for continued expansion of the air.

When the effects of both sonic throats are included the nozzle actually resembles a double throat Laval nozzle. Figure 3.3 below illustrates the suggested approach. The jet impingement region must be solved as non-isentropic to reflect the total pressure losses from the first shockwave as described above. Standard shockwave theory describes the total pressure loss, and the downstream properties act as the initial conditions for the next section of the nozzle.

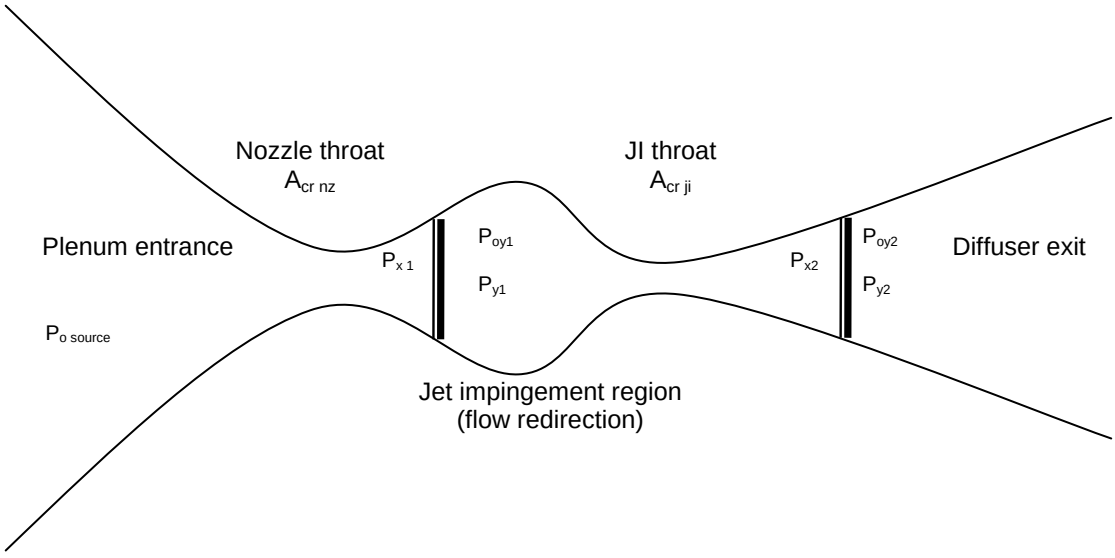


Figure 3.3 Double-throat Laval nozzle

*3.3.1 Calculation Techniques*

Calculation of the converging portion of the nozzle is based entirely on the inlet condition and area ratio. The nozzle throat is sonic for pressure ratios above the critical pressure ratio. Past the nozzle throat some assumptions must be made about the jet path. The actual prototype has a cone-shaped diffuser section. The cone angle is 82°—much larger than the expected jet expansion. This produces what is known as an *under-expanded* supersonic jet. Because the angle is so large, the jet will detach from the nozzle wall and temporarily become a free jet, until it reaches the impinging surface. Using the Kim and Park [15] study as precedent, an assumption can be made about the jet expansion rate to yield an area profile to solve for other thermodynamic properties. This area profile can be adjusted to correlate the analytical model with experimental data.

The position of the first shockwave is estimated based on an estimate of the total pressure loss and the presence of a stationary impingement bubble with the associated constant pressure. The narrow transition region where the air is accelerated into the jet impingement throat is lumped into the impingement bubble region. The jet impingement throat is located on the edge of the impingement bubble, at the same radius as the impingement jet maximum radius. The air from the jet impingement throat flows out as a disk, hugging the impinging wall. This wall jet is calculated as isentropic flow based on a constant height and increasing circumference. The second shockwave is positioned appropriately to return the air to near atmospheric stagnation pressure, as required by the exit boundary condition.

All calculations were done using MATLAB. A chart describing compressible flow through an isentropic Laval nozzle for k = 1.4 is shown in Appendix B. A routine called tableValues.m was created to interpolate values from this chart, and it is included in Appendix C. Each region was calculated individually and the results were combined. The complete MATLAB code is displayed in Appendix D.

*3.3.2 Model Results*

Executing the above procedure for calculation yields the fluid properties for each region of the nozzle. The regions of interest are the regions in contact with the impingement surface, including the impingement bubble, the jet impingement throat, and the diverging disk. The estimated pressure distribution from each of these regions was compiled into a single pressure profile, and is displayed below in figure 3.4 for the case of a 300 kPa relative inlet pressure and 0.5 mm gap width. The impingement bubble pressure is represented by approximately half of the inlet pressure. There is a region of extreme vacuum in the 1-4 mm radius region and a discontinuity at 4 mm where the second shockwave would fall. Finally, there is a slight vacuum produced as a result of the Bernoulli Effect which decays to nearly atmospheric conditions by 7 mm.

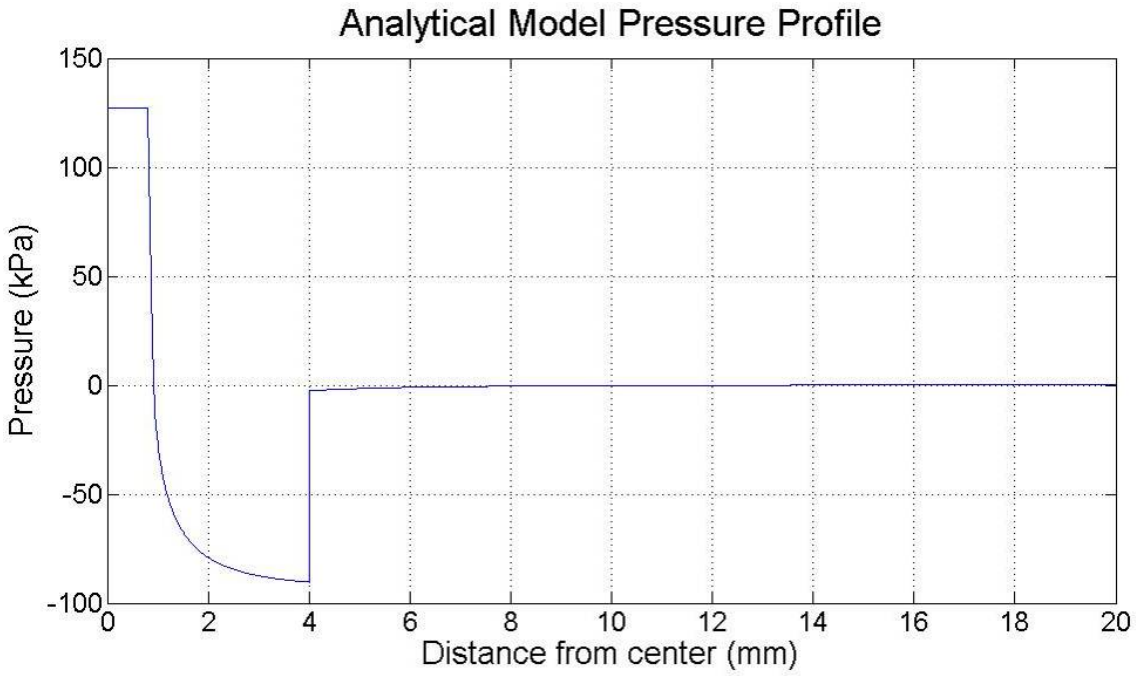


Figure 3.4 Analytical model result for 300 kPa relative (401 kPa absolute) inlet pressure 0.5 mm gap width case

*3.3.3 Evaluation of Analytical Model*

This model is not intended to yield exact numerical correlation with experimental data, but rather to suggest some basic mechanisms of the flow and demonstrate an approximate calculation. The experimental data described in chapter 5 of this paper is superimposed over the plot of the analytical model in figure 3.5, below. These are both for the case of 300 kPa relative inlet pressure (401 kPa absolute) and 0.5 mm gap width.

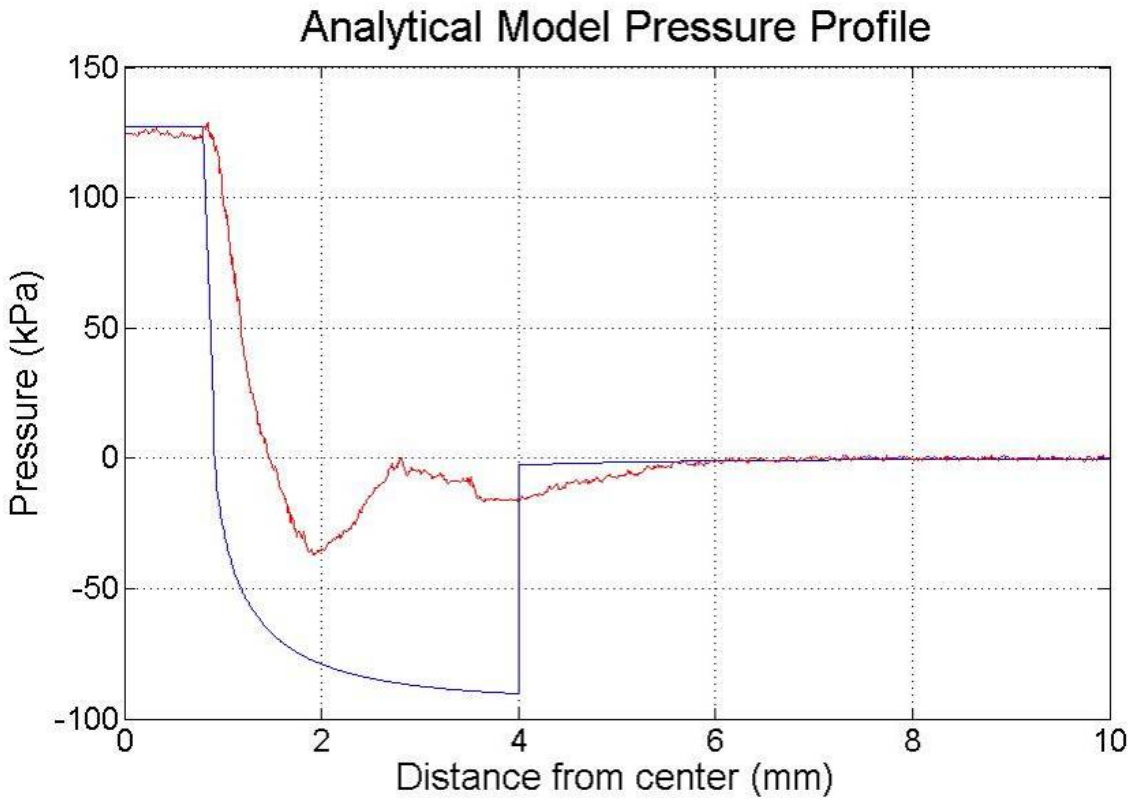


Figure 3.5 Comparison of Analytical model result and experimental data for 300 kPa relative (401 kPa absolute) inlet pressure 0.5 mm gap width case

There are several things to observe from the pressure profiles above. First, the pressure values at the center of impingement are very closely matched. This pressure is based upon the normal shockwave calculations in the impinging jet. Second, the vacuum between 1 and 4 mm radius is exaggerated. The model predicts twice the observed vacuum. Third, there is too large a discontinuity from the shockwave. The shockwave is an area of mixing and must occupy some region of space, which would yield more distortion between 3 and 5 mm. Finally, the Bernoulli Effect region of the flow underestimates the vacuum observed.

The analytical approximation presented is an approximate first-order model to describe the flow through the impingement nozzle with standard fluid equations. While it is not an exact match, it explains the possible mechanisms of the flow and predicts levitation. The author did not find any comparable mathematical description of the flow in the literature that would explain the possibility of levitation. Nonetheless, a more detailed model could better predict the phenomenon. A numerical study using FEM techniques would confirm the properties of the flow and give a better illustration of how impingement levitation is possible.

# CHAPTER 4

# NUMERICAL STUDIES

Even with good assumptions in place, the results of the analytical model presented in the previous chapter do not closely match the experimental data. Using a finite element method (FEM) removes some of the conjecture and provides a wealth of information about the properties of the impingement flow. In addition to providing pressure data, FEM automatically determines other features of the flow which are useful for understanding levitation impingement. The velocity, temperature, and turbulence can all be plotted in an easy-to-understand three-dimensional view. The streamlines illustrate the path of the flow. These visual aids make a numerical FEM study valuable.

## 4.1 Introduction to CFX Modeling Technique

The computational fluid dynamic (CFD) module of the ANSYS software package, called CFX, was chosen for this numerical model. CFX is accessed through the ANSYS Workbench software suite, which provides a solid modeler and a user-friendly interface. The appropriate geometry must be built or imported and must represent the actual fluid space—not the container. Once the geometry is finished a mesh must be created. A mesh is viewed as a net-like collection of lines that cover the entire geometry space. Each line represents the border between two elements, and is typically drawn between two nodes. The CFX meshing utility allows several options for meshing and refinement to ensure appropriate element coverage of the fluid space.

The meshing utility also allows the creation and naming of regions to simplify the problem setup step.

Once the mesh is finalized CFX-Pre is started. This interface controls the problem definition and boundary conditions. The fluid domain must be specified, as well as any solver controls and other important bounding conditions. With all relevant information assigned, the problem definition file is written to the solver, and CFX-Solver opens. This screen tracks the progress of the solver, plotting the RMS residual value as each iteration is processed. The results file is stored when the RMS residual values fall below the chosen minimum.

The results are viewed in CFX-Post. Post-processing allows for the creation of several visualizations, including streamlines and shaded planes. A line can be created and any chosen property can be plotted on the chart viewer. These values can be exported for further analysis. Post-processing allows three-dimensional interaction with the fluid flow solution.

## 4.2 Problem Definition

A representation of the prototype impingement end effector was constructed in the ANSYS Workbench geometry modeler. The chamber and the sub-flange areas were partially reduced to decrease the size of the model. This does not affect the area of interest, which is the impingement area. A second model was created using a twelve degree axis-symmetric slice of the original model to reduce time in repeat calculation and to allow for more refinement in the mesh. The figures shown in this document are based on the full model, shown below, to aid in visualization.

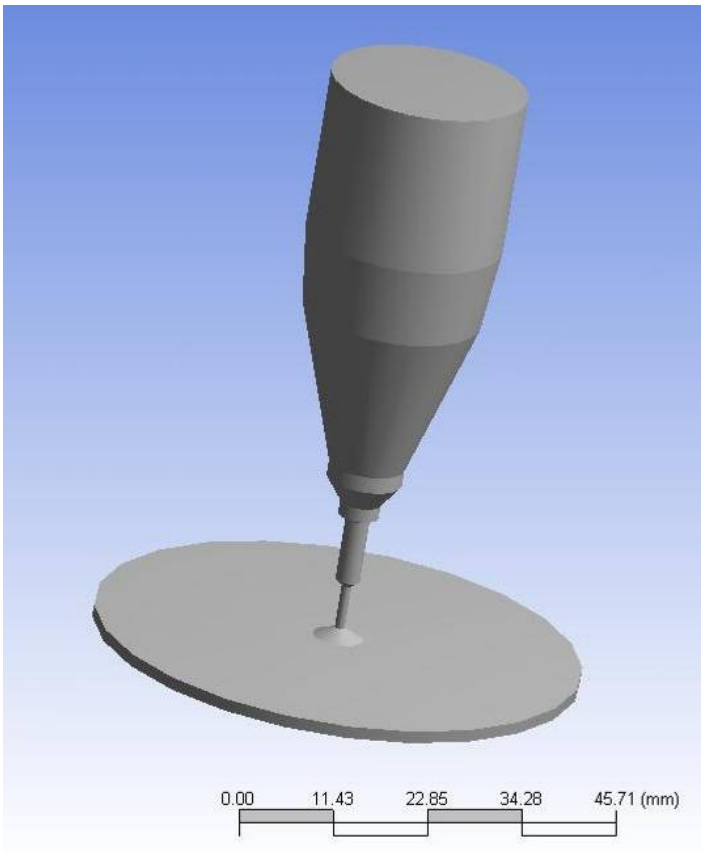


Figure 4.1 Prototype geometry

*4.2.1 Meshing Considerations*

With the impingement area constructed the boundary was meshed. One of the goals of the meshing is to ensure there are sufficient elements to avoid discontinuities between nodes. This was done by reducing the edge length reference and increasing the minimum number of elements between surfaces. The impingement region was further refined to ensure an accurate representation of that critical area. The area of refinement is shown below.

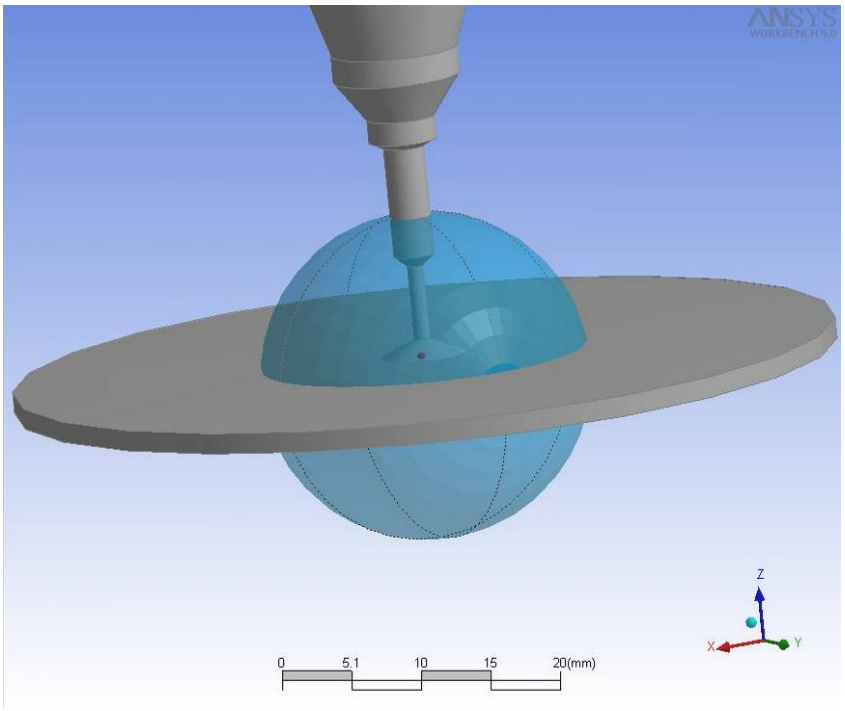


Figure 4.2 Region of refinement

*4.2.2 Boundary Conditions*

The fluid domain was chosen as “Air at 25°C,” and the “Total Energy” option was set to reflect the contribution of compressibility to the problem. The outlet boundary condition was set at 101 kPa to reflect standard atmospheric conditions, and the inlet boundary condition was set for the appropriate case, in absolute pressure values. The bounding walls were assigned the “no slip” condition, typical of fluid problems. The maximum number of iterations was increased in the solver control dialogue box to ensure that the solution converges acceptably, within the allowed RMS residual.

## 4.3 Results and Discussion

The results are particularly useful for providing a three-dimensional illustration of the properties of the flow. The streamlines for the problem are shown below in figure 4.3. The twisting of the streamlines is due to turbulence and accumulated error.

There are several things to observe relating to the jet. The model confirms sonic flow at the throat of the nozzle. Just past the throat there is an area of expansion where the flow goes into the supersonic range. This is typical after passing through a constriction for pressure ratios below the critical sonic ratio of 0.528. The velocity of the impingement jet reaches a maximum of about Mach 1.3, which is much lower than the mathematical model predicted. Further, the fastest velocity is shown in the center of the jet, at the jet core.

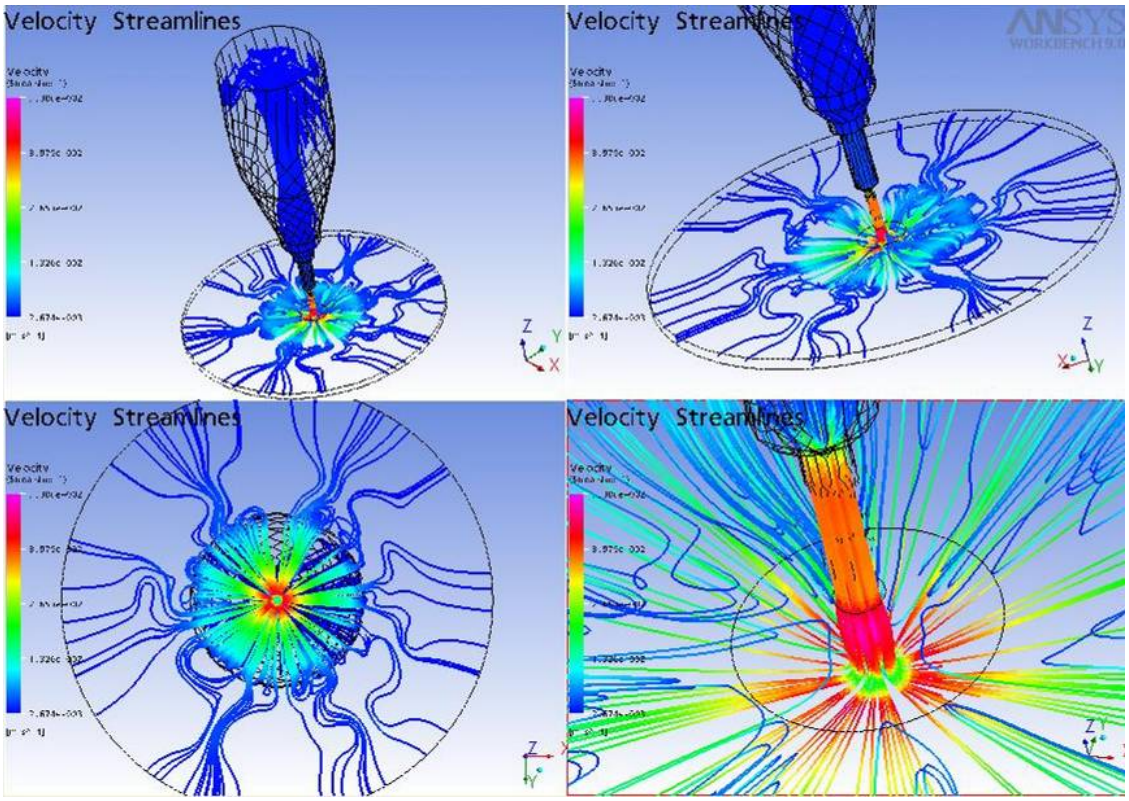


Figure 4.3 Velocity streamlines

There are several important features to note in the impingement region. The jet shows a sharp decrease in velocity just before hitting the impingement surface. This velocity reduction corresponds to an increase in static pressure. This means the air is being partially stagnated, causing the kinetic energy of the air to be partly converted back into potential energy. Immediately outside the region of higher pressure there is a second area of supersonic flow. Again, the velocity reaches a maximum around Mach 1.3, which is less than the mathematical model prediction. Approximately 10 mm from the center there is a sudden turbulent disruption. This disruption is consistent with the turbulence seen in a shockwave. This location is highlighted below in figure 4.4.

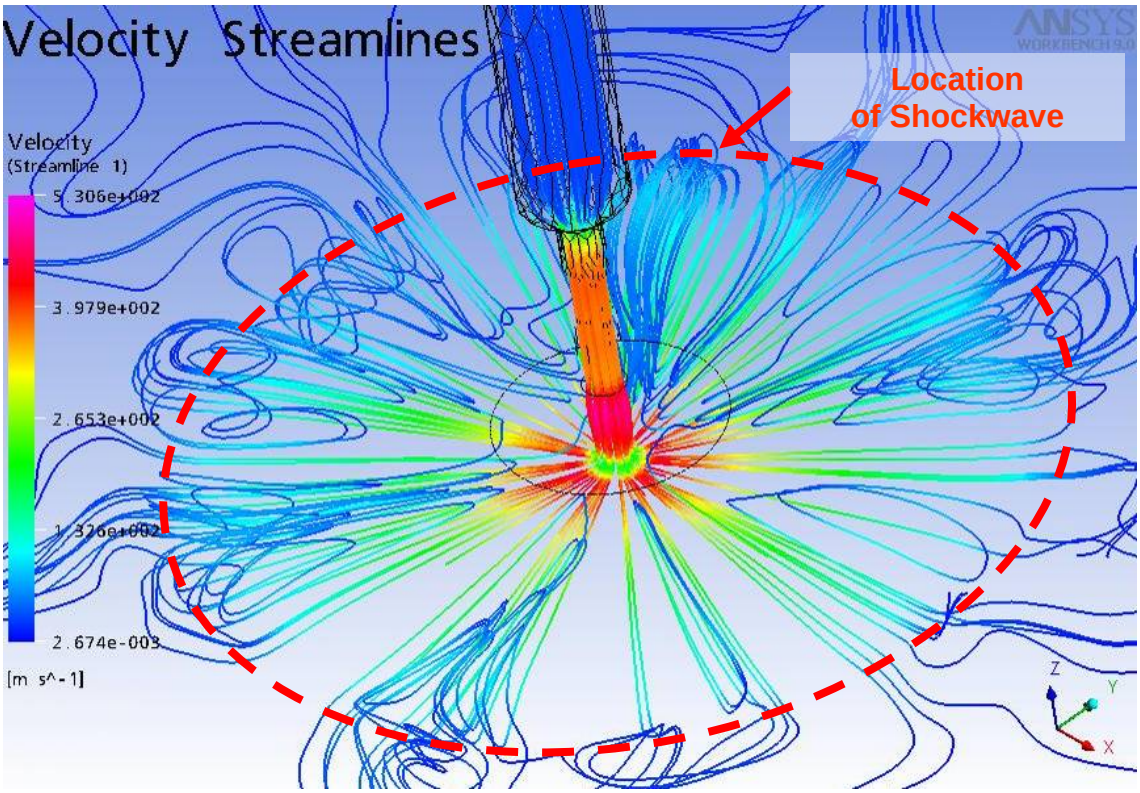


Figure 4.4 Location of shockwave

The supersonic jet tends to stick to the wall, leaving a void in the upper area of the gap. When the wall jet hits the shockwave the flow is redirected upwards and back toward the center, so that a large stationary eddy is created. Figure 4.5 shows a cross section of the streamlines with the supersonic flow shown in white.

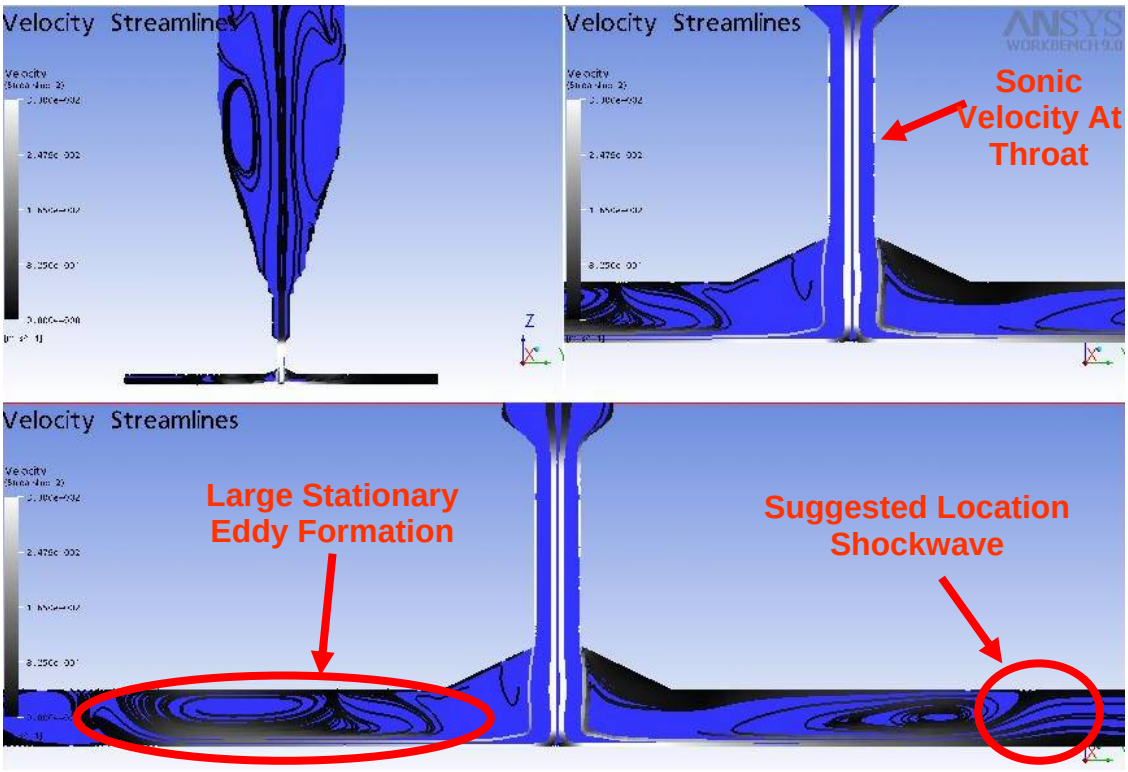


Figure 4.5 Cross sections of streamlines with stationary structures identified (supersonic streamlines in white)

In addition to the streamlines, the CFX model determines the relative pressure distribution. A cross section is shown below in figure 4.6. The color bands clearly illustrate the formation of a half sphere of high pressure at the center of impingement. The pressure diminishes further away from the center, and drops to low pressure (dark blue color) at the corresponding supersonic flow regions. One particularly interesting feature is the area of vacuum in the jet immediately past the throat. This pattern replicates the rarefaction fans mentioned in figure 2.1 and 2.2 in the Literature Review section. This suggests that the initial jet flow follows the pattern of a free jet.

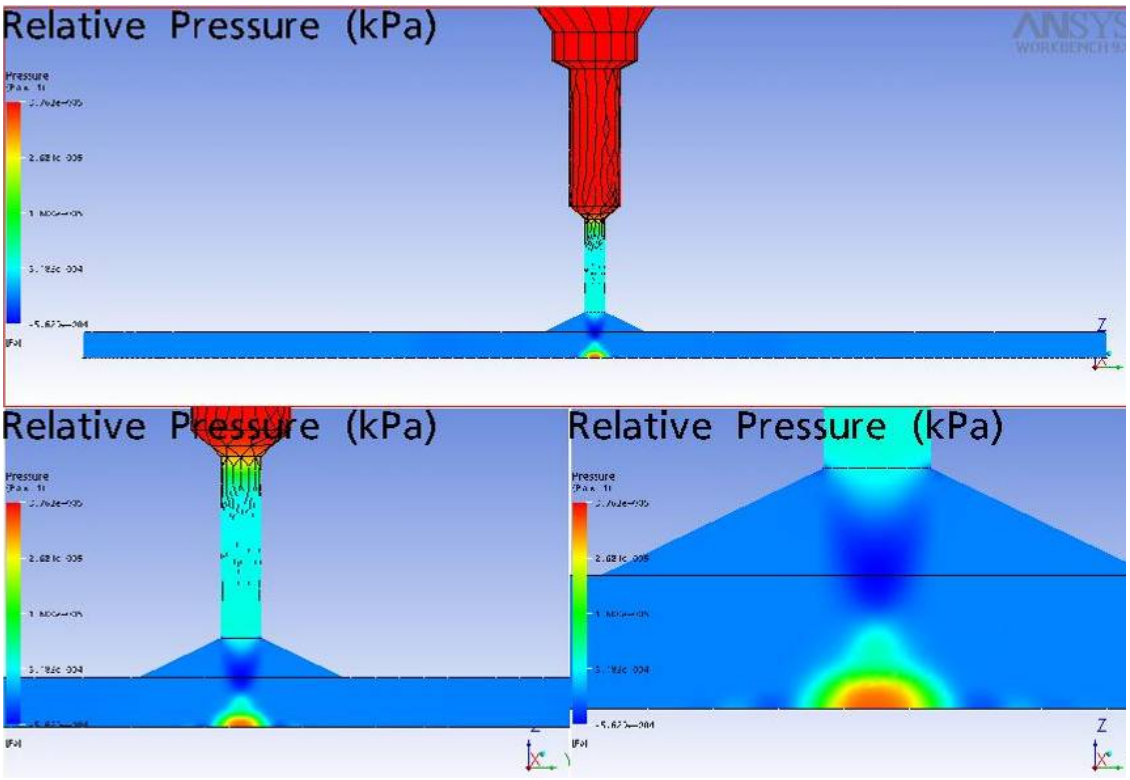


Figure 4.6 Relative pressure cross sections

The nodal solutions bordering the impingement surface on the cross section were exported and plotted to gain the numerical representation of the pressure profile. The pressure profile is shown with the corresponding experimental data set for 0.5 mm gap width 100 kPa inlet pressure. There is some discrepancy between the datasets in the centerline impingement pressure region. CFX predicts a higher impingement pressure, and does not account for any pressure loss between the inlet and the outlet. There is also some difference in the vacuum region. This is attributed to extra turbulence in the actual end effector. It could also be due to the disruption of air flow in the pressure port experiment.

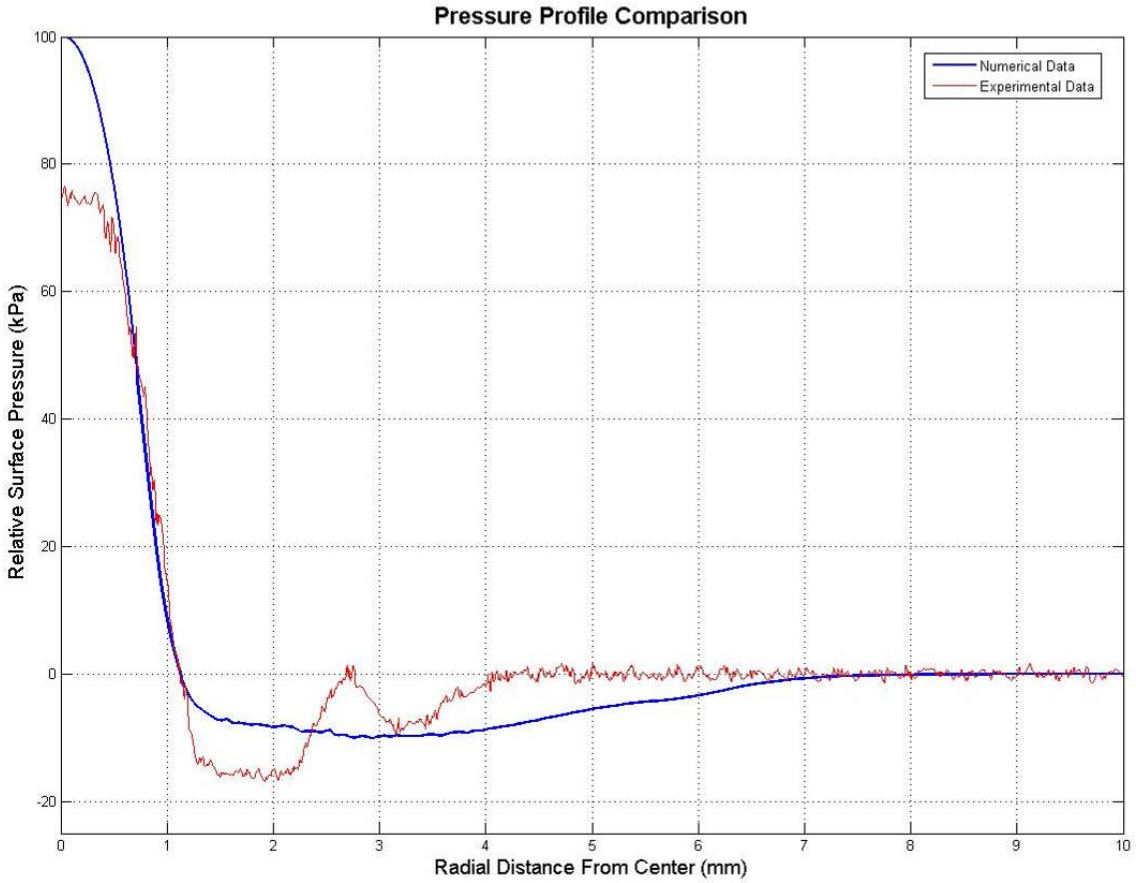


Figure 4.7 Pressure profile comparison

## 4.4 Evaluation of Numerical Model

The CFX solution offers insight into the impingement flow properties. The streamlines reveal the path of the flow, and the velocity values confirm that there are regions of supersonic flow. The results show the formation of large stationary structures, and the presence of a central highly compressed core. Most of all, there is good data to represent the pressure distribution on the impingement surface.

Despite the convincing visual presentation, there are some limits to the benefits of a numerical study. It requires a great deal of time and computing power to process

the results of each simulation. The fluid element meshing technique is poorly suited to accommodate problems with changing geometry, as the case of a changing flange to surface gap. This makes it difficult to obtain data relating the net impingement force to a changing gap distance, which would require multiple runs of geometry regeneration, meshing, and solving. In addition to the required computing power, there is a limited credibility to FEM fluid studies. For these reasons, it is appropriate to conduct an empirical study with traditional lab techniques and a physical prototype, the results of which are shown in the following chapter.

# CHAPTER 5

# EXPERIMENTAL STUDIES

It is difficult to precisely model fluid flow due to the random mixing of fluid particles, such as in turbulence and eddies. Because of this difficulty, closed-form theoretical solutions are typically not available for real-world applications. Hydrodynamic and Thermodynamic equations predict the general trends, but typically rely on correlations and statistical coefficients to estimate the large-scale effects. An alternative to mathematical modeling and statistical averages is a numerical approach. Using computer software, the actual fluid geometry of a theoretical prototype can be constructed and the flow can be predicted, but the results must typically be verified with a physical prototype to gain respect. Further, it is very difficult to implement FEM for changing geometry, as in the case of the impingement nozzle being lifted off the surface of a plate. For these reasons, it is appropriate to use experimental techniques.

To verify the results of the analytical impingement model and the CFX numerical solution previously presented, two experiments were performed. The experiments quantify the phenomenon previously discussed and provide more complete understanding of how impingement levitation works. An experimental prototype was constructed as shown below in figure 5.1. This radially symmetric prototype consists of a pressurized plenum, a converging channel, a diverging exit port, and a flange. It was designed to allow attachment to a robotic arm as an end effector.

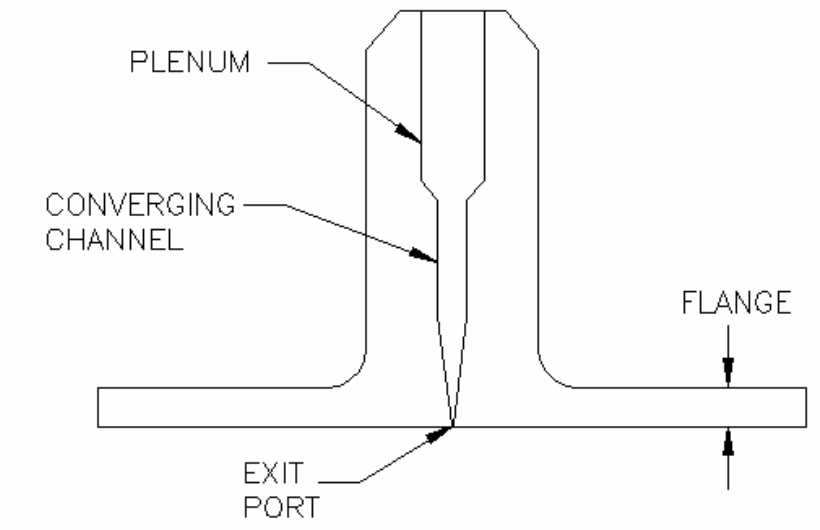


Figure 5.1 Impingement prototype concept

(a) (b) (c)

Figure 5.2 Impingement prototype end effector shown (a) as the CAD rendering, (b) as produced, and (c) mounted to the robot arm

## 5.1 Pressure Profile Experiment

The goal of this experiment was to record the pressure profile developed by the air impingement end effector at various input pressures and gap distances. Recording

the pressure profile was accompanied by recording quasi-static pressure at various points across the surface of impingement. This was achieved by using a robotic arm to move the impingement end effector slowly across a flat plate. A pressure port located in the center of the plate was connected to several pressure gages, and a data acquisition system recorded the gage output.

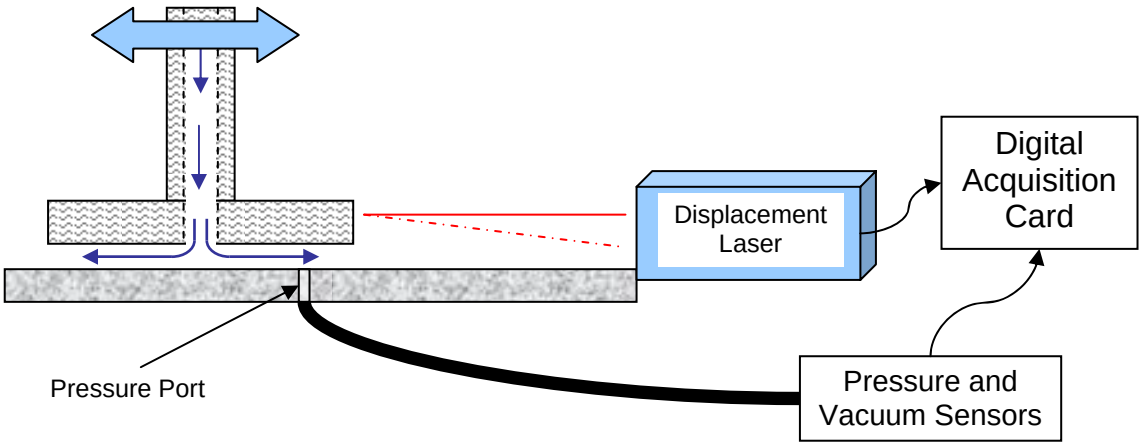


Figure 5.3 Pressure profile experiment schematic

*5.1.1 Apparatus*

A flat 30x20x2 cm aluminum plate was fashioned with a 1.5 mm diameter hole in the center. This hole served as the pressure port and was connected to the pressure sensors via pneumatic tubing. Three different sensors were used to record the port pressure: a pressure sensor, a vacuum sensor, and a differential sensor. For this experiment the high end connection of the differential sensor was left open to atmosphere. Each of these sensors was connected to a CyberResearch PCCDAS 1616AO 16-bit data acquisition card. The redundancy of pressure sensors is necessary

due to the characteristics of each sensor. The pressure sensor will measure both vacuum and positive pressure, but it is quite noisy. The vacuum and differential sensors use output a higher quality signal, but cannot measure the complete positive pressure range.

The impingement end effector was connected to the robotic arm for positioning over the plate. The end effector inlet pressure was measured by a fourth sensor. A Micro-Optronic NCDT 1400 laser interferometer was used to measure the horizontal position of the end effector. A data acquisition system and laptop computer recorded the signals of the sensors.

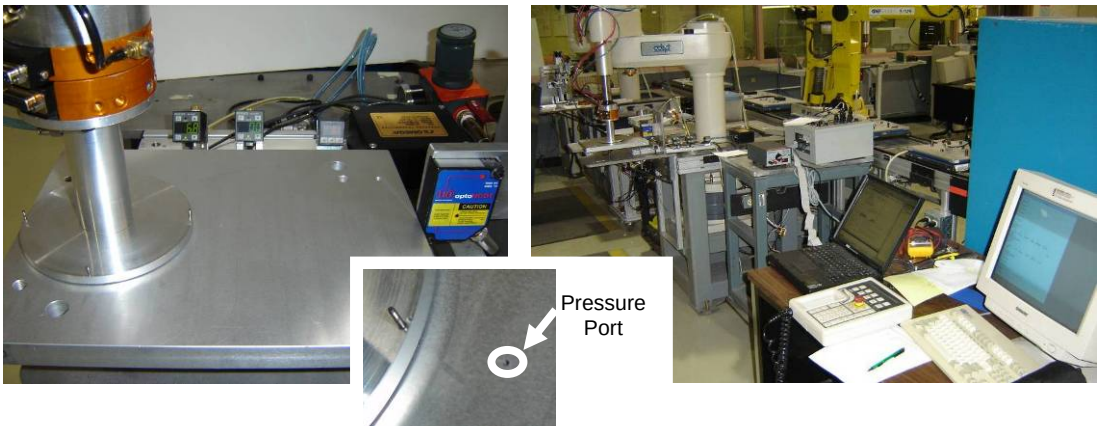


Figure 5.4 Pressure profile experiment apparatus

*5.1.2 Procedure*

The laser was mounted to the robot's work table and was positioned to point along the direction of the robot's global X axis. X-axis alignment was verified by

moving the arm several inches along the X axis and visually confirming that the beam position on the end effector remained stationary on the end effector.

After the laser was aligned and firmly attached to the table, the plate was put into position. The plate was leveled by pressing it tightly into the end effector and then tightening four alignment screws on the corners. This step ensured that the plane of the plate was parallel to the XY plane of the robot, so the Z distance would remain constant. The port on the plate was positioned on the path of the beam to intersect the center of the end effector.

Once the sensors and plate were in place, the robot was programmed for the required motion. The initial gap width was created by placing a stack of paper 0.5 mm think on the plate and then positioning the end effector against it. This gives an accurate Z value to the robot for reference. The subsequent Z values were accomplished through the robot's coordinate system. The pressures and gap widths tested are listed in table 5.1 by experiment number.

Table 5.1 Pressure Profile Experiment Number Chart

| Gap Width (mm) \ Relative Chamber Pressure (kPa) | 50 | 100 | 200 | 300 |
|---|---|---|---|---|
| 0.5 | 1 | 2 | 3 | 4 |
| 1.0 | 5 | 6 | 7 | 8 |
| 1.5 | 9 | 10 | 11 | 12 |
| 2.0 | 13 | 14 | 15 | 16 |

The end effector was more finely centered onto the port by changing X and Y until the maximum pressure was reached at the sensors. This ensured that the center of the end effector passed directly over the port. After the center point was established in the robot's coordinates, beginning and ending X-values were chosen to pass the edge of the effector over the port and go completely past the center. The laser range is limited to 100 mm so measurements were taken from the leading edge to the center. Testing only half the profile is acceptable because the profile is symmetrical.

For each data set, the robot was moved to its initial position at the appropriate Z value. The inlet pressure was adjusted to the desired level. The DAC was set to record the appropriate channels at 250 Hz for 100 seconds. In all, two million data points were collected. The robot was commanded to move across the center to the ending point as the DAC was started. The +/- 10 Volt signals were filtered and converted to distance and pressure readings in MATLAB. These pressure profiles are plotted in Appendix E.

### *5.1.3 Results*

A grid of the pressure profiles is shown below in figure 5.5. Sixteen variations were tested. The pressure profile for data set 12 is plotted in figure 5.6, which is representative of the other data sets. The complete plots are included in Appendix E, where all the data sets are referenced according to Table 5.1, above.

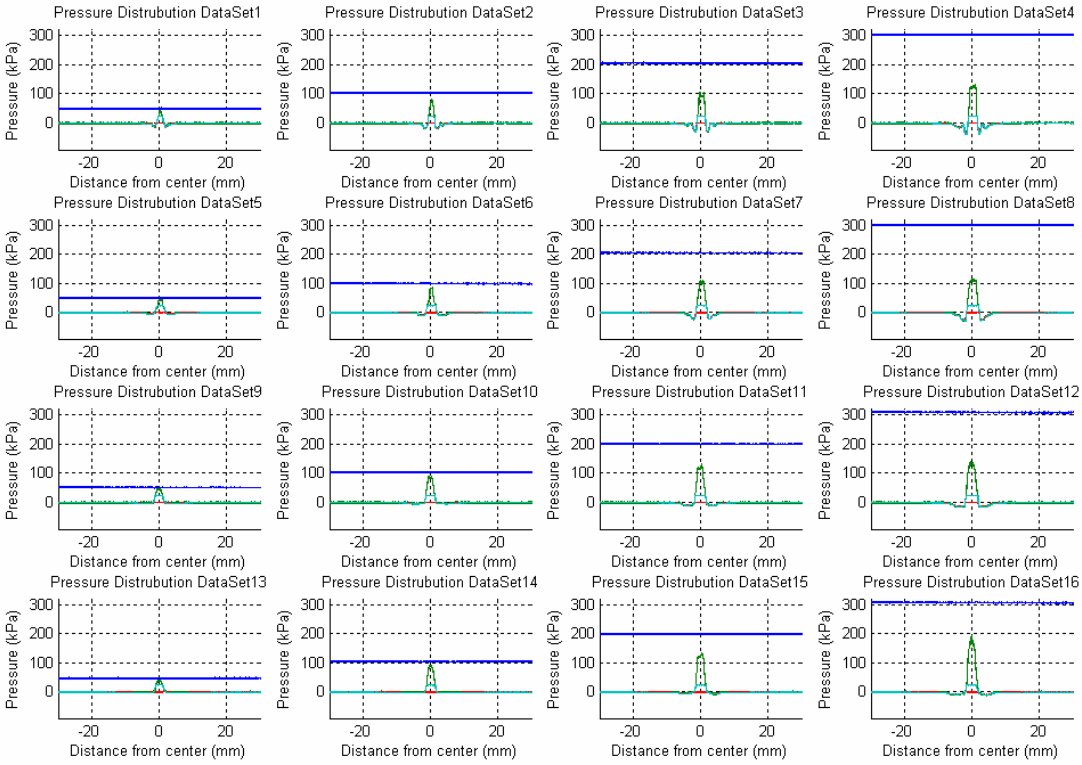


Figure 5.5 Pressure profile experiment results

There are several features to recognize in each profile. The center rise of positive pressure values is the region of impingement. This is the area where air will be recompressed and redirected. This represents a disk approximately 4 mm in diameter. Adjoining the positive pressure impingement region is the region of vacuum. This typically extends from 2 to 5 mm radially and diminishes to atmospheric pressure around 8 mm radially. Note that the surface area of this washer-shaped vacuum region is 5-8 times greater than the surface area of the disc. The result is that a slight vacuum can overcome an impingement pressure several times larger, resulting in a net lifting force.

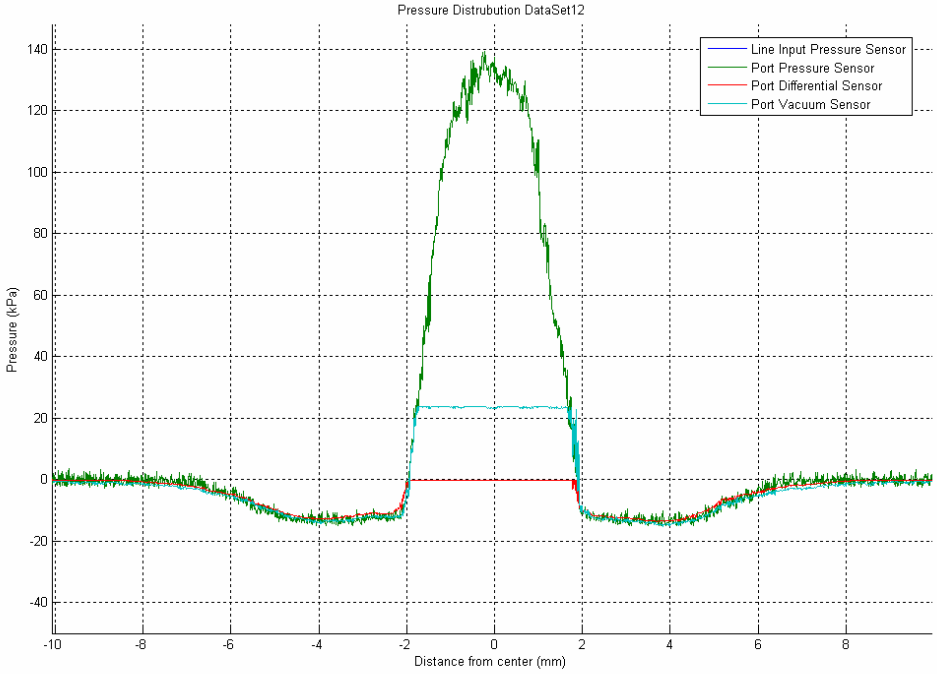


Figure 5.6 Pressure profile for 300 kPa input, 1.5 mm gap

Once the pressure profiles were recorded and filtered, a routine was created in MATLAB to estimate the total lifting force over the entire surface of the end effector. A numerical integration routine was created using the trapezoid method, and is outlined in equations 5.1 through 5.3. For verification, the net force was tracked as a function of the radial area integrated and is shown below in figures 5.7 and 5.8, sorted by gap width, and then by chamber pressure, respectively.

$$F_{NET} = \int dF = \int_{center}^{outside} PdA \qquad (5.1)$$

$$dA = 2\Pi\, rdr = 2\pi X \Delta X \tag{5.2}$$

$$F_{NET} = \sum_{i=0}^{30mm} \frac{(P_1 + P_2)}{2} \left(\pi (X_i + X_{i+1})(X_{i+1} - X_i)\right) \tag{5.3}$$

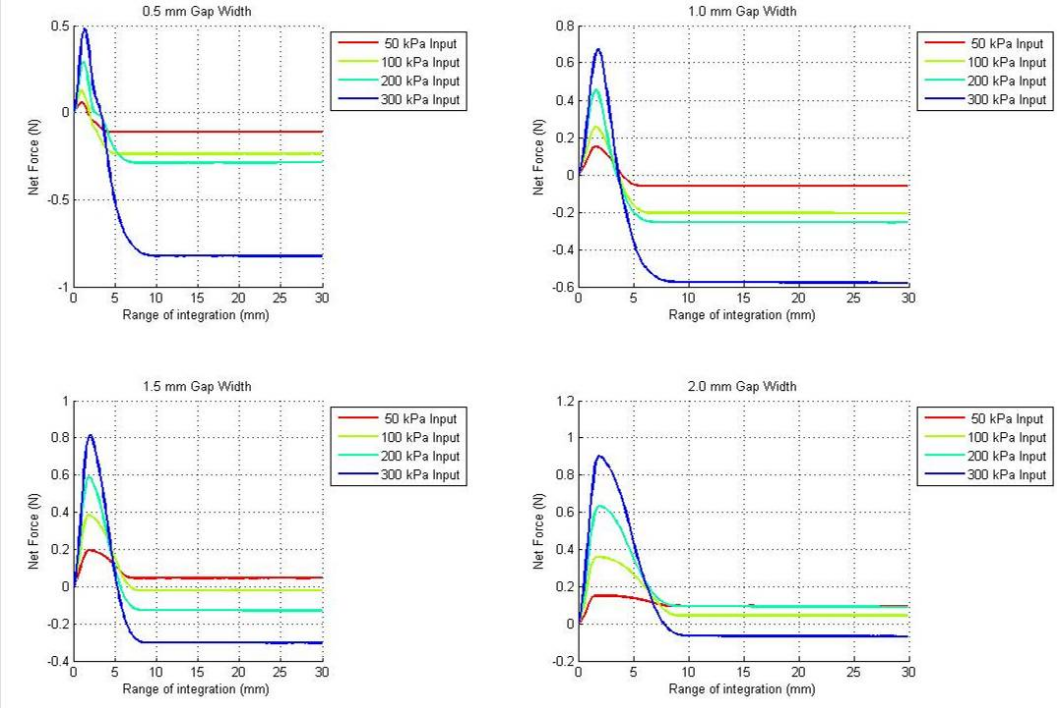


Figure 5.7 Integrated net force as a function of range of integration sorted by gap width

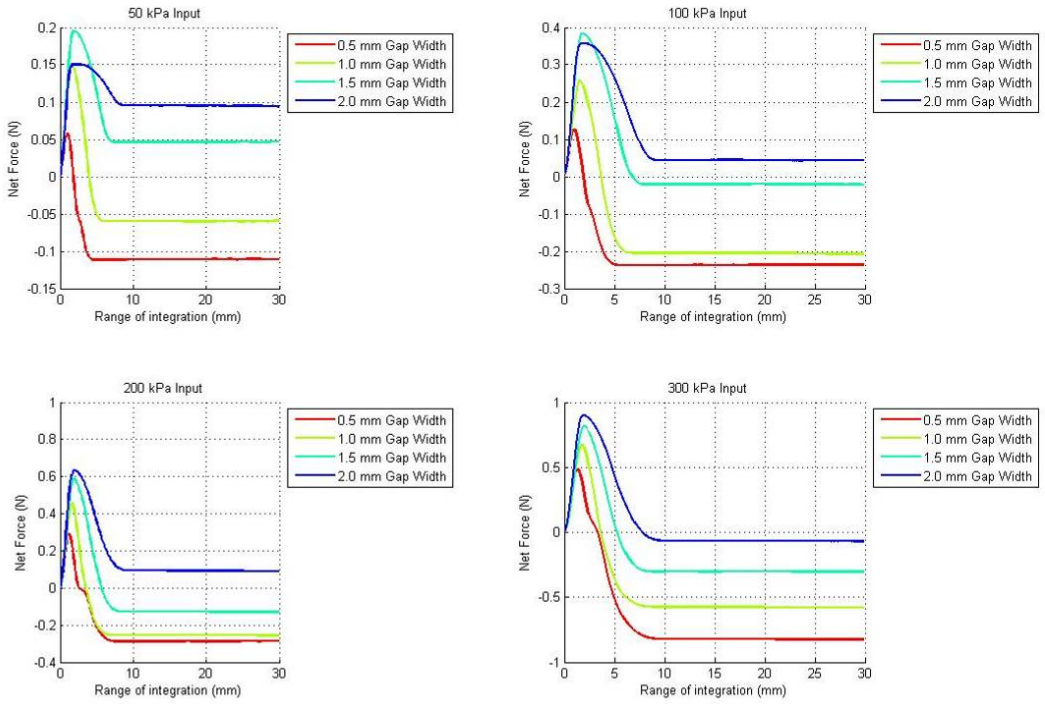


Figure 5.8 Integrated net force as a function of range of integration sorted by pressure input

*5.1.4 Conclusions*

The results of this experiment confirm that there is a central disk of impingement, surrounded by a region of high vacuum. That region of high vacuum diminishes to atmospheric pressure at a radius of approximately 8 mm. This is consistent with the analytical model presented and the numerical studies. The integrated pressure profile illustrates that the flow contributing to the lifting force is fully developed within the vacuum region. The data suggests that the flange need not be any larger then 2 cm in diameter to develop the full lift capacity.

## 5.2 Net Force vs. Gap Experiment

The goal of this experiment was to record how the net force generated from a confined impinging jet changes as the gap width is varied from near zero to 10 cm. This was accomplished by measuring the force on a flat plate from the confined impinging jet as the end effector was moved along the range.

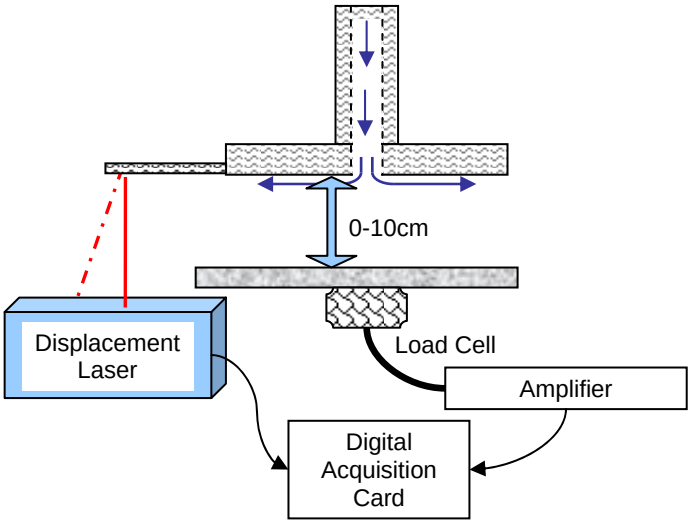


Figure 5.9 Net force vs. gap experiment schematic

### *5.2.1 Apparatus*

The impingement end effector was used in conjunction with an Adept SCARA type robotic arm. A small bracket was rigidly attached to the flange on the end effector to extend a surface for the laser to read from. A silicon wafer was attached to a 14 cm square plate to provide a smooth surface for impingement. The plate was mounted to an Omega LCAE-1KG platform type load cell, and the load cell was connected to an Omega DP41 amplifier and calibrated. An electronic pressure regulator was used to

supply the input pressure, and a pressure sensor was attached to the line input for verification. Spacer blocks were constructed with screw holes to mount the load cell, and the setup was placed on a large aluminum plate for alignment to the robot's workspace plane. Extra aluminum blocks were inserted under the impingement plate to give sufficient preload for reading in compression only.


Figure 5.10 Net force vs. gap experiment apparatus

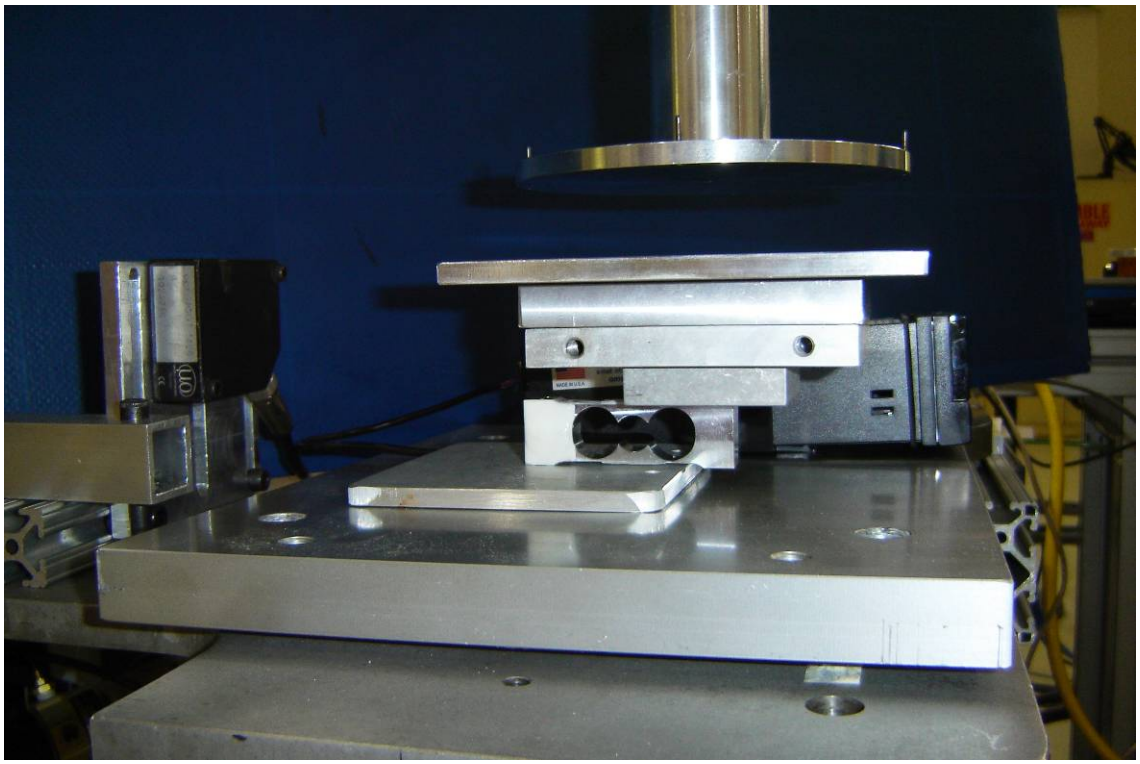

Figure 5.11 Net force vs. gap experiment apparatus side view

### *5.2.2 Procedure*

The impingement surface was visually leveled to the plane of the robot workspace by adjusting the four supporting screws at the corners of the base plate. The end effector flange and the impingement surface were made parallel within visual accuracy. Once this was accomplished the initial position of the end effector was determined. With the air turned off, the robot was commanded to approach the surface in 25 micron increments until a contact force was recorded from the load cell. The position preceding contact was stored as the initial point. A second point was stored 10 cm above the surface to mark the ending point.

Once the points were correctly stored the end effector was brought to the beginning point, and the air was turned on and adjusted to the appropriate level. With the data acquisition card enabled, the end effector was stepped from the beginning position to the ending position in small increments. To ensure time for air structures to form, a delay was added between steps. A list of input pressures tested is shown below in table 5.2. The force on the platform and the relative end effector position were recorded at 250 Hz for 600 seconds while the motion took place. The sensors output a 0-10 V signal, which is converted into the appropriate units and filtered using MATLAB.

Table 5.2 Line Input Test Pressures

| Experiment Number | Line Input Pressure (kPa) |
|---|---|
| 1 | 25 |
| 2 | 50 |
| 3 | 100 |
| 4 | 170 |
| 5 | 200 |
| 6 | 300 |
| 7 | 400 |
| 8 | 500 |
| 9 | 575 |

### *5.2.3 Results*

The data from each of the experiments is complied below in figure 5.12. The distance between the flange surface and the impingement surface is referred to as the *gap distance.* The initial readings are positive pressure because the end effector is acting as an air bearing. This *air bearing region* extends from near contact to 0.3-0.5 mm. There is a region of extremely high vacuum in the 0.4-1 mm gap range. This region will hereafter be referred to as the *region of attachment,* because it is in this narrow region where an object would typically attach itself to the end effector. There is a much larger region, the *diminishing vacuum region* extending from approximately 1-17 mm, where a significant vacuum is formed. All input pressures tested go from net vacuum to net positive pressure approximately 17 mm above the impingement surface. Beyond 17 mm the net force is positive, referred to as the *free jet repulsive region.*

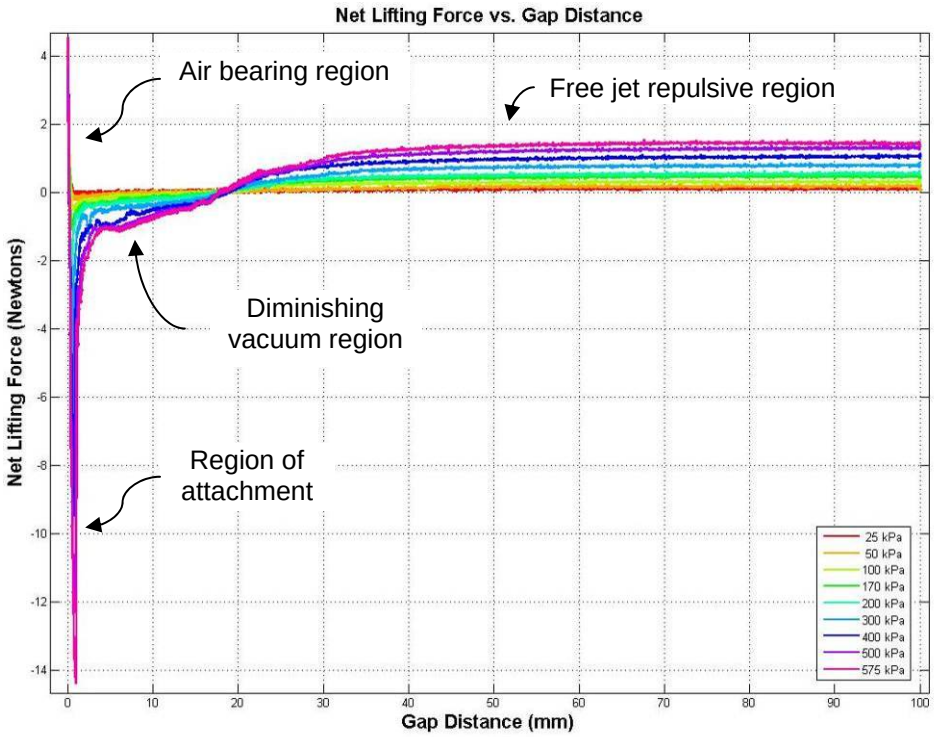


Figure 5.12 Net force vs. gap experiment results

The range of testing was limited to 100 mm because the laser available for the experiment shares this range, as does the Z-axis of the robot. It is not the subject of this research, however, to study the effects of jet decay, so this is sufficient. The positive pressure region of the plot suggests that the maximum repulsive pressure is reached around 50 mm. If the experiment were extended over a larger range, the positive pressure would eventually decay to zero, such that no effect of the jet could be felt from a very large distance. Other studies [7,8,14] have been published detailing the jet decay, but the vacuum and attachment regions are of interest for this paper, shown below in figures 5.13and 5.14 respectively.

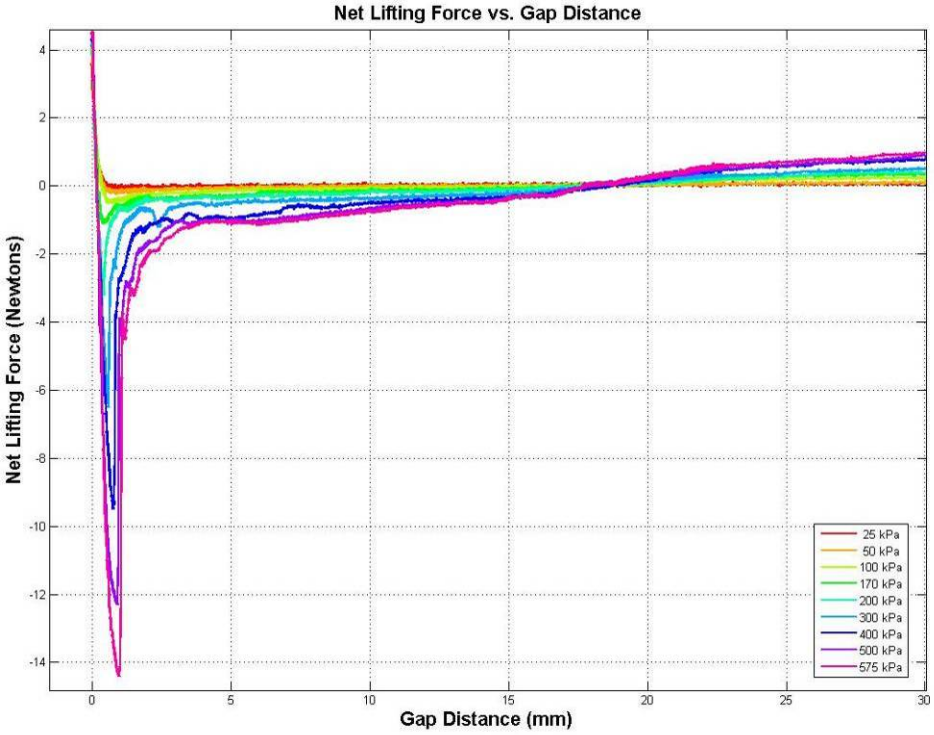


Figure 5.13 Diminishing vacuum region

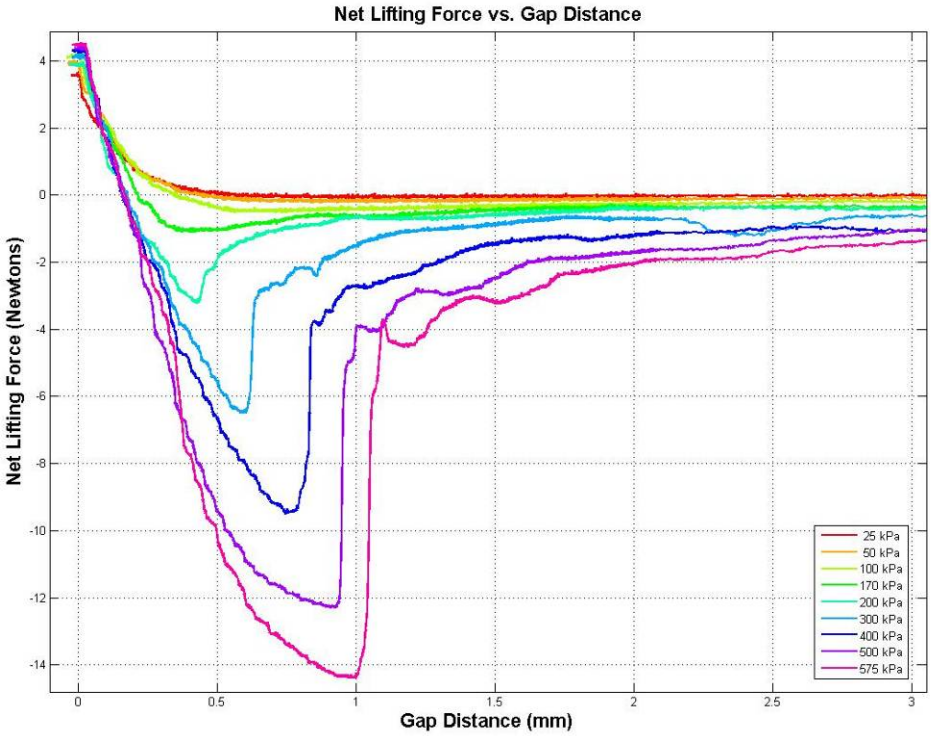


Figure 5.14 Attachment region

It is important to understand how this data is relevant to part acquisition, specifically how a planar object would react when approached by the impingement end effector. Consider a 150 g aluminum plate approached by the end effector supplied with 300 kPa input pressure. A net downward force of approximately 0.75 N would be applied to the plate as the end effector descended from 100 mm. At 17 mm there would be no net force on the plate. As the end effector entered the vacuum region, a net upward force would begin to be applied to the place, but a 1.5 N force is required to overcome the effects of gravity. The vacuum region for 300 kPa input generates only 1 N of lifting force, so the plate would remain at rest on the surface.

As the end effector approaches the region of attachment the net lifting force would begin to increase until sufficient lift was generated to overcome the plate's weight. The net unbalanced force would cause the plate to accelerate toward the surface of the end effector, which in turn causes an even greater unbalanced force. The plate will accelerate toward the surface of the end effector until it reaches a distance where the lifting force is balanced with the weight of the plate. For a 150 g plate, this would occur at approximately 0.3 mm from the surface of the end effector. The plate will remain attached at this point unless a force greater than the maximum lift force for 300 kPa is applied. Because 1.5 N is required to levitate the object, a 5 N force would be required to overcome the 6.5 N maximum lift force for 300 kPa. This is the self-stabilization mechanism of impingement lift.

The maximum net lifting force for each input pressure was compiled and is plotted below in figure 5.15. The 25, 50, and 100 kPa input pressures are subsonic jets because the inlet/outlet pressure ratio is below what is necessary for supersonic flow. Lift is still generated, however, through the Bernoulli Effect. The 175 kPa and 200 kPa input pressures are considered transitional, and a free jet at these input pressures would be considered "moderately underdeveloped." Above this range a free jet would be labeled "highly underdeveloped" [14].

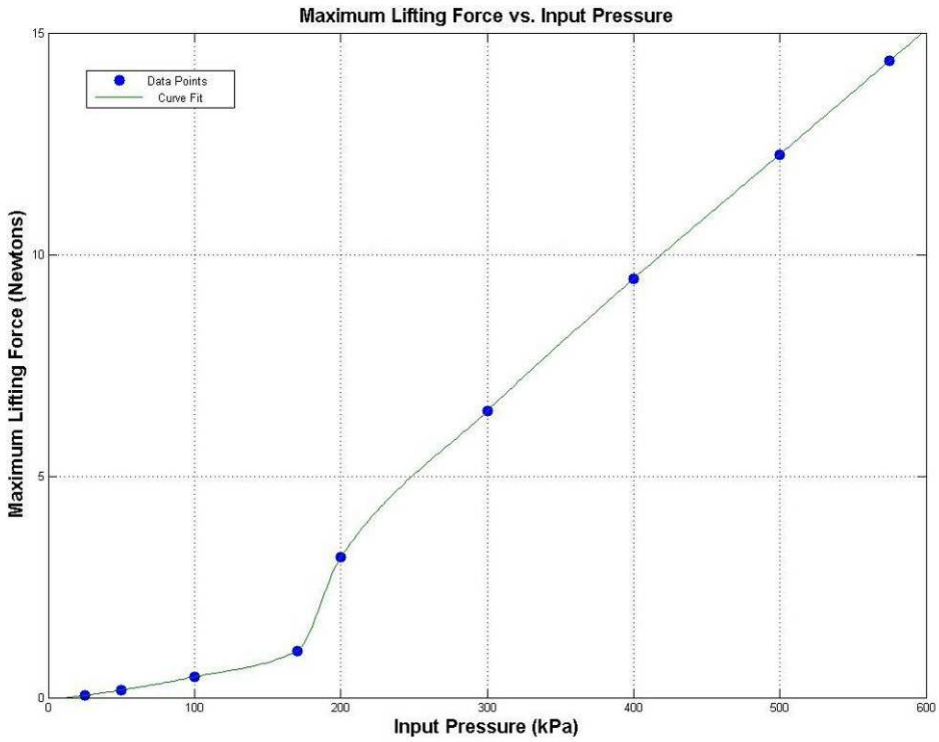

Figure 5.15 Max net lift values

A second graph was compiled to compare the diminishing vacuum region net lift values. This is the net lift just past what was previously defined as the region of attachment. There is not a clear point in the data to record immediately past the drop in net lift, so the net lift was recorded for each pressure at a gap distance of 2 mm, safely within the diminishing vacuum region. The values are compiled below, shown with the maximum net lift values, in figure 5.16. A quadratic curve fit is shown. Notice that this curve coincides with the portion of the maximum lift values previously identified as subsonic. This indicates that the lower curve reflects the lift generated from the Bernoulli Effect and the upper curve reflects the effects of supersonic flow. The region

of attachment is actually the region where the gap width is narrow enough to force supersonic flow.

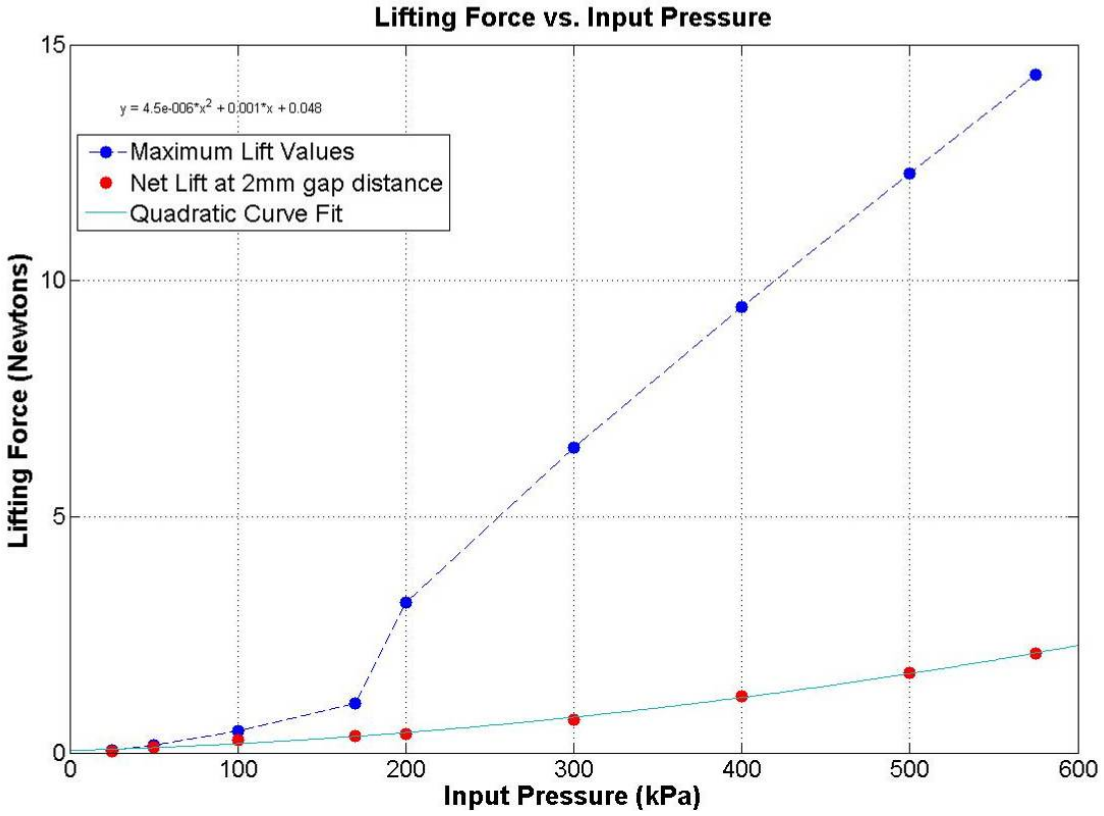


Figure 5.16 Maximum net lift compared with net lift at 2 mm gap

### *5.2.4 Conclusions*

The data establishes a region of maximum vacuum development, or region of attachment, for very small gap distances—typically less than 1 mm. This region is where supersonic flow would occur. It demonstrates that the transition between air bearing and vacuum generation is different for different air pressures, between approximately 0.3 and 0.5 mm, but the transition between the vacuum region and the

free jet repulsive region is fixed at a gap distance of 17 mm. The maximum repulsion force is fully developed at a gap distance of approximately 50 mm, and eventually will diminish to zero. The establishment of each of these regions provides data necessary for implementation of this device in a part acquisition application.

This experiment also supports the theory that there is a transition between subsonic and supersonic flow development, depending on the input pressure. Figure 5.15 shows a very clear relationship between input pressure and max net force. The 25, 50, 100, and 170 kPa input pressure points show a linear relationship, and the input pressures 200 kPa and above fall very tightly into line with a different slope. This implies a transition between 170 kPa and 200 kPa, and we conjecture that this transition is the development of supersonic flow. Further, the necessary pressure input for part acquisition can be read off the chart.

Figure 5.16 shows that the flow at 2 mm gap distance coincides with the net lift values for subsonic flow. This implies that the region of extreme vacuum is caused by supersonic flow, and the region of diminishing vacuum is caused by Bernoulli Effect. Further, this suggests the optimum gap width for the creation of a supersonic disk diffuser, and shows the maximum gap width where the flow can remain supersonic.

# CHAPTER 6

# CONCLUSION

Heat transfer is not the only application for air jet impingement. The vacuum created from an impinging jet can be used to levitate an object. This phenomenon has been previously exploited and even patented, but there has been little direct research to explain the effect. The object of this paper is to elucidate the use of jet impingement for object levitation by utilizing analytical, numerical, and empirical techniques.

A mathematical model was derived using compressible flow theory, in conjunction with shockwave calculation techniques. The results of this calculation show similar flow features to the experimental data, but the pressure profile across the surface of impingement overestimates the amount of vacuum produced. A numerical model was constructed and run in the ANSYS CFX software package to illustrate the flow patterns. Several variations in inlet pressure and gap width were studied. The results verify the presence of a sonic throat at the nozzle and a supersonic disk surrounding the impingement region. The pressure profile of the impingement surface in the CFX model is similar to the experimentally recorded pressure profile, and both show a net lifting force from the vacuum disk region.

To verify the analytical and numerical studies, an experimental prototype was created. Two experiments were performed to provide quantitative measurement of the air jet impingement effects. The first experiment recorded the pressure as a function of

radial position. This yielded a collection of curves that show an area of high pressure in the center of the impingement, surrounded by a disk-shaped region of vacuum. This result establishes that the levitation effect is generated within a disk of approximately 2 cm in diameter, and accordingly, it allows for the production of air jet impingement levitation fixtures with a similarly sized flange area.

The second experiment tested the net lifting force as a function of gap width. The prototype end effector was moved from nearly touching a surface to 100 mm away. The net force on the surface was recorded from a load cell beneath the surface. The results show a region of extreme vacuum when the end effector flange and the impingement plate are less than 1 mm apart. From approximately 1 mm to 17 mm gap distance a weaker vacuum was present. Positive pressures resulted beyond 17 mm, leveling off around a 40 mm gap distance. The results show that air jet impingement can be used to levitate an object in excess of one kilogram.

The maximum attraction force was recorded for each pressure tested, revealing a strong correlation between the subsonic jets and the highly under expanded supersonic jets. In addition, the net lifting force was compiled at 2 mm gap width. These values correlate to a quadratic fit in line with the subsonic pressure ratios. This implies that supersonic flow is only developed at narrow gap width—less than 1 mm. The lower net lift levels result from Bernoulli lift.

The conclusions presented in this paper demonstrate the mechanics of air jet impingement levitation. Mathematical, numerical, and experimental arguments show the creation of vacuum and, therefore, lift. The experimental results quantify the lifting

potential and the size of the impingement area, and show that the levitation effect is self stabilizing. Most importantly, the relationship between impingement inlet pressure and the net lifting force is documented. It is concluded that air jet impingement is valuable as a material handling technique, and is suitable for a variety of applications with consideration to the topics presented below.

## 6.1 Practical Considerations

Air jet impingement offers many practical advantages in material handling. It offers non-contact handling, with the exception of lateral constraint. The device design is simple; end effectors are ruggedly constructed and require little or no maintenance. The levitation effect is self-stabilizing. The gap width will automatically settle where the net force is balanced without manual readjustment of the inlet pressure. Air jet impingement can be used in high particulate environments because the contaminants will not enter the fixture. The cost of a levitation end effector is less than comparable vacuum cups and vacuum generators.

There are a few disadvantages to consider as well. Air jet impingement levitation is not precise, because the object is free to float on a cushion of air. While the lateral constraints can aid in this problem, it can be less precise than vacuum cups. There is also constant air consumption while an object is being levitated. The impingement can be noisy in certain situations. Finally, similar to vacuum cups, the object requires a flat surface adhesion. These considerations should be observed when choosing a levitation method.

## 6.2 Future Work

Many aspects of the phenomenon of air jet impingement levitation are explained here, but more research is warranted. The analytical model presented in this paper is only an approximation, and should be refined to better correlate with the vacuum observed from experiment. This would give a better understanding of the impingement flow effects. Also, a more precise measurement of the pressure profiles should be taken. The pressure port used to measure the profiles in this research was similar in size to the nozzle diameter. This results in some averaging of the data and poor resolution. A more precise measurement would yield better correlation with CFD and analytical models. This research has not addressed impingement levitation for incompressible fluids; study of such effects would provide additional insight into the prevailing fluid mechanics and would be relevant to applications such as underwater lifting.

In addition to the flow effects that elicit future work, some investigation should be made into practical ancillary devices for the jet impingement lifting technique. One possible improvement would be anti-tilt mechanisms to equalize the gap across the surface of the target. Another particularly useful area of study is non-contact lateral stabilization concepts. This would make air jet impingement entirely non-contact. Study in these areas would improve the usefulness of air jet impingement for levitation.

# APPENDIX A

# LIST OF RELEVANT PATENTS

LIST OF RELEVANT PATENTS

Cronquist, D. H. Air Head. D.H. Cronquist, assignee. Patent 2905768. 22 Sep. 1959.

Tarbuck, R. R. Pneumatic Sheet Seperator. R. R. Tarbuck, assignee. Patent 3158367. 24 Nov. 1964.

Rainbow, J. Suction Pickup with Air Bearing. J. Rainbow, assignee. Patent 3220723. 30 Nov. 1965.

Olsson, Raymond G. and Earl C. Williams. Contactless Lifter. R. G. Olsson et al., assignee. Patent 3438668. 15 Apr. 1969.

Mammel, W. K. Pressurized Fluid Pickup Device. W. K. Mammel, assignee. Patent 3466079. 9 Sep. 1969.

Benjamin, J. M. Pneumatic Probe for Handling Flat Objects. J. M. Benjamin, assignee. Patent 3425736. 4 Feb. 1969.

Carlomagno, G. M. Process for Applying Forces to Glass Sheets, in Particular at a High Temperature. G. M. Carlomagno, assignee. Patent 4921520. 1 May 1990.

McIlraith, L. and A. Christie. Contactless Handling of Objects. Creo Inc., assignee. Patent 6601888. 5 Aug. 2003.

Hiroshi, A. Non-Contact Conveying Device. A. Hiroshi, assignee. Patent 5067762. 26 Nov. 1991

# APPENDIX B

## ONE-DIMENSIONAL ISENTROPIC COMPRESSIBLE-FLOW FUNCTIONS FOR AN IDEAL GAS WITH CONSTANT SPECIFIC HEATS AND MOLAR MASS, AND K=1.4

| M | $\frac{A}{A^*}$ | $\frac{P}{P_0}$ | $\frac{\rho}{\rho_0}$ | $\frac{T}{T_0}$ |
|---|---|---|---|---|
| 0 | $\infty$ | 1.0000 | 1.0000 | 1.0000 |
| 0.1000 | 5.8218 | 0.9930 | 0.9950 | 0.9980 |
| 0.2000 | 2.9635 | 0.9725 | 0.9803 | 0.9921 |
| 0.3000 | 2.0351 | 0.9395 | 0.9564 | 0.9823 |
| 0.4000 | 1.5901 | 0.8956 | 0.9243 | 0.9690 |
| 0.5000 | 1.3398 | 0.8430 | 0.8852 | 0.9524 |
| 0.6000 | 1.1882 | 0.7840 | 0.8405 | 0.9328 |
| 0.7000 | 1.0944 | 0.7209 | 0.7916 | 0.9107 |
| 0.8000 | 1.0382 | 0.6560 | 0.7400 | 0.8865 |
| 0.9000 | 1.0089 | 0.5913 | 0.6870 | 0.8606 |
| 1.0000 | 1.0000 | 0.5283 | 0.6339 | 0.8333 |
| 1.1000 | 1.0079 | 0.4684 | 0.5817 | 0.8052 |
| 1.2000 | 1.0304 | 0.4124 | 0.5311 | 0.7764 |
| 1.3000 | 1.0663 | 0.3609 | 0.4829 | 0.7474 |
| 1.4000 | 1.1149 | 0.3142 | 0.4374 | 0.7184 |
| 1.5000 | 1.1762 | 0.2724 | 0.3950 | 0.6897 |
| 1.6000 | 1.2502 | 0.2353 | 0.3557 | 0.6614 |
| 1.7000 | 1.3376 | 0.2026 | 0.3197 | 0.6337 |
| 1.8000 | 1.4390 | 0.1740 | 0.2868 | 0.6068 |
| 1.9000 | 1.5553 | 0.1492 | 0.2570 | 0.5807 |
| 2.0000 | 1.6875 | 0.1278 | 0.2300 | 0.5556 |
| 2.1000 | 1.8369 | 0.1094 | 0.2058 | 0.5313 |
| 2.2000 | 2.0050 | 0.0935 | 0.1841 | 0.5081 |
| 2.3000 | 2.1931 | 0.0800 | 0.1646 | 0.4859 |
| 2.4000 | 2.4031 | 0.0684 | 0.1472 | 0.4647 |
| 2.5000 | 2.6367 | 0.0585 | 0.1317 | 0.4444 |
| 2.6000 | 2.8960 | 0.0501 | 0.1179 | 0.4252 |
| 2.7000 | 3.1830 | 0.0430 | 0.1056 | 0.4068 |
| 2.8000 | 3.5001 | 0.0368 | 0.0946 | 0.3894 |
| 2.9000 | 3.8498 | 0.0317 | 0.0849 | 0.3729 |
| 3.0000 | 4.2346 | 0.0272 | 0.0762 | 0.3571 |
| 3.5000 | 6.7896 | 0.0131 | 0.0452 | 0.2899 |
| 4.0000 | 10.7188 | 0.0066 | 0.0277 | 0.2381 |
| 4.5000 | 16.5622 | 0.0035 | 0.0174 | 0.1980 |
| 5.0000 | 25.0000 | 0.0019 | 0.0113 | 0.1667 |
| 6.0000 | 53.1798 | 0.0006 | 0.0052 | 0.1220 |
| 7.0000 | 104.1429 | 0.0002 | 0.0026 | 0.0926 |
| 8.0000 | 190.1094 | 0.0001 | 0.0014 | 0.0725 |
| 9.0000 | 327.1893 | 0.0000 | 0.0008 | 0.0581 |
| 10.0000 | 535.9375 | 0.0000 | 0.0005 | 0.0476 |

# APPENDIX C

# INTERPROLATION PROGRAM FOR AIR TABLE

```
%tableValues.m
%
%[tableOUT]=tableValues(parameter value, columnIN, range, [colsOUT]).
%
%Description:  This function will accept a critical parameter and return the
%corresponding set of information based on the table value equations.
%Only one critical parameter can be given and is specified by a flag number.
%The range must be specified (supersonic or subsonic) by 'sps' or 'sbs'.
%The desired output is also specified as indexed by the flag numbers.
%
%   parameter--known value to locate position on chart (scalar or vector)
%
%   columnIN--the information provided as described below
%       1   Mach Number (where M=1 is sonic)
%       2   Area/A*     (where A* is the critical area at the throat)
%       3   Pressure/Po (Po is the relevant stagnation pressure)
%       4   Rho/Rho0    (Rho0 is the density at Po)
%       5   Temp/Temp0  (Temp0 is the temperature at Po)
%
%   range--'sbs' or 'sps' for subsonic or supersonic, respectively
%
%   colsOUT--the desired values from the chart.  The output will be an
%       array in the order referenced above
%       ex. colsOUT=[1 2 4] will contain Mach Number, Area/A* and Rho/Rho0
%
function [tableOUT]=tableValues(parameter, columnIN, range, colsOUT)

    %create table from equations listed on A-15
    k=1.4;
    R=287.0;    %kgm^2/s^2

    %solve for M values if col 1 not supplied
    if columnIN==1
        %skip ahead
        M=parameter;
    elseif columnIN==2
        %solve for M using A/A*
        if range=='sbs'
            M=0.001:.001:1;
            AOverAstar=(1./M).*((2/(k+1))*(1+((k-1)/2).*M.^2)).^((k+1)/(2*(k-1)));
        elseif range=='sps'
            M=1:.001:10;
            AOverAstar=(1./M).*((2/(k+1))*(1+((k-1)/2).*M.^2)).^((k+1)/(2*(k-1)));
        end
        M=interp1(AOverAstar,M,parameter,'spline');
    elseif columnIN==3
        %solve for M using P/Po
        M=0.01:.001:10;
        POverPZero=(1+((k-1)/2.).*M.^2).^(-k/(k-1));
        M=interp1(POverPZero,M,parameter,'spline');
    elseif columnIN==4
        %solve for M using Rho/Rho0
```

```
        M=0.01:.001:10;
        RhoOverRhoZero=(1+((k-1)/2).*M.^2).^(-1/(k-1));
        M=interp1(RhoOverRhoZero,M,parameter,'spline');
    elseif columnIN==5
        %solve for M using T/To
        M=0.01:.001:10;
        TOverTZero=(1+((k-1)/2).*M.^2).^(-1);
        M=interp1(TOverTZero,M,parameter,'spline');
    else
        return;
    end

    %Generate output table values based on input values
    AOverAstar=(1./M).*((2/(k+1))*(1+((k-1)/2).*M.^2)).^((k+1)/(2*(k-1)));
    POverPZero=(1+((k-1)/2.).*M.^2).^(-k/(k-1));
    RhoOverRhoZero=(1+((k-1)/2).*M.^2).^(-1/(k-1));
    TOverTZero=(1+((k-1)/2).*M.^2).^(-1);
    table(:,1)=M;
    table(:,2)=AOverAstar;
    table(:,3)=POverPZero;
    table(:,4)=RhoOverRhoZero;
    table(:,5)=TOverTZero;
    for n=1:length(colsOUT)
        tableOUT(:,n)=table(:,colsOUT(n));
    end
end
```

# APPENDIX D

# MATLAB CODE FOR ANALYTICAL CALCULATIONS

# MATLAB CODE FOR ANALYTICAL CALCULATIONS

```
%combined functions for nozzle, JI region, and two disk areas
%options for display
%1 is true, 0 is false
showNozzleShape=0;
showNozzleArea=0;
showNozzleMach=0;
showNozzleVelocity=0;

showJIshape=0;
showJIarea=0;
showJIvelocity=0;
showJIpressure=0;

showFDvelocity=0;
showFDpressure=0;

showSDvelocity=0;
showSDpressure=0;

showCombinedPressure=1;
showActualProfile=1;

%known gas constants
k=1.4;      %isentropic coefficient of expansion for air ideal gas
R=287.0;    %m^2/(s^2 K) Universal Gas Constant for air ideal gas

%---------------------
%   Nozzle Region
%---------------------
%Constants
%gemometry
nzDiaIN=.012;          %m--diameter at top of nozzle inlet
nzDiaOUT=.0012;        %m--diameter at throat of nozzle
nzHeight=.066;         %m--6.6cm height of nozzle (from top of throat)
%Thermodynamic properties
nzPo=400000;           %400kPa
nzTo=298;              %Kelvin--25 C
nzRhoZero=nzPo/(R*nzTo);%rho zero ideal gas

%
%   Model Nozzle Area below
%
nzAreaIN=nzDiaIN^2*pi()/4;       %m^2
nzAreaOUT=nzDiaOUT^2*pi()/4;    %m^2
   %   Nozzle Area will be modeled linearly between the inlet and outlet
nzAreaSlope=(nzAreaOUT-nzAreaIN)/nzHeight;
   %   Nozzle Height will be incremented so nzArea can be incremented
nzHeightProfile=0:.001:nzHeight;
nzAreaProfile=nzHeightProfile.*nzAreaSlope+nzAreaIN;
```

```
nzHeightProfile=nzHeight-nzHeightProfile;

%   Model Properties in nozzle
%         velocity at inlet is unknown
%         Laval nozzle theory for isentropic flow to determine M from A/A*

nzCrArea=nzAreaOUT;           %m^2--the nozzle critical area at the throat
%call tableValues function to determine Mach number
nzTable=tableValues((nzAreaProfile./nzCrArea),2,'sbs',[1 2 3 4 5]);
 nzMdot=(.63394*nzRhoZero)*nzAreaOUT*(1*sqrt(k*R*.83333*nzTo));

%plot nozzle shape if asked
if showNozzleShape==1
    figure(1);
    fill([-nzDiaIN/2 nzDiaIN/2 nzDiaOUT/2 -nzDiaOUT/2],[nzHeight nzHeight 0 0],'b');
    title('Nozzle Shape');
    V=(.2*nzHeight+1.2*nzHeight)/2;
    axis([-V V -.2*nzHeight 1.2*nzHeight]);
    xlabel('Horizontal Distance (m)');
    ylabel('Height (m)');
end
%plot nozzle area if asked
if showNozzleArea==1
    figure(2);
    plot(nzHeightProfile,nzAreaProfile);
    set(gca,'XDir','reverse');
    title('Nozzle Area');
    xlabel('Height above throat (m)');
    ylabel('Area (m^2)');
end
%plot parameters if desired
if showNozzleMach==1
    figure(3);
    plot(nzHeightProfile,nzTable(:,1));
    set(gca,'XDir','reverse');
    title('Mach Number increase in throat');
    xlabel('Height above throat (m)');
    ylabel('Mach Number');
end
if showNozzleVelocity==1
    figure(4);
    nzT=nzTable(:,5).*nzTo;
    nzC=sqrt(k.*R.*nzT);
    nzVel=nzC.*nzTable(:,1);
    plot(nzHeightProfile,nzVel);
    set(gca,'XDir','reverse');
    title('Velocity Increase in Throat');
    ylabel('Velocity (m/s)');
    xlabel('Height above throat (m)');
end

%report values
```

```
fprintf('\n\nResults (assuming choked flow)\n------------------------------\n');
fprintf('Mass flow rate through nozzle:\t\t\t%6.4f (g/s)\n',nzMdot*1000);
fprintf('Pressure at nozzle exit:\t\t\t\t%6.2f (kPa)\n',(.52828*nzPo/1000));
fprintf('-----------------------------------------\n');

%---------------------------
%   Jet Impingement Region (ji)
%---------------------------
%
% initial expansion in center
%

jiMinDia=nzDiaOUT;
jiMaxDia=0.0018;
jiTopHeight=.002;      %distance from throat to top of impingement layer region
jiBottomHeight=.0005;   %bottom layer distance

%first calculate free jet area profiles
jiProfile1=0:.00001:jiTopHeight;    %consider jiProfile the distance from the nozzle
jiDiaProfile=jiMinDia+jiProfile1./jiTopHeight.*(jiMaxDia-jiMinDia);
jiAreaProfile=pi().*jiDiaProfile.^2./4;
    %Recall that the elements go from the nozzle toward the impingement surface

%Thermodynamic Properties
jiTo=298;               %K
nzDischargeCoef=1;     %arbitrary constant to reduce Po
nzExitPo=400000;       %kPa
jiPo=nzDischargeCoef*nzExitPo;
jiRhoZero=jiPo/(R*jiTo);%rho zero ideal gas

jiCrArea=nzDiaOUT.^2.*pi()./4;
jiAxA=jiAreaProfile./jiCrArea;
jiXvalues=tableValues(jiAxA,2,'sps',1:5);

jiMdot=(.63394*jiRhoZero)*jiCrArea*(1*sqrt(k*R*.83333*jiTo));

if showJIshape==1
   figure(6);
   fill([-jiMaxDia/2 -jiMaxDia/2 -jiMinDia/2 jiMinDia/2 jiMaxDia/2 jiMaxDia/2],[0 jiBottomHeight
(jiTopHeight+jiBottomHeight) (jiTopHeight+jiBottomHeight) jiBottomHeight 0],'b');
   axis([-.006 .006 -.002 .010]);
end

if showJIarea==1
    figure(7);
    plot(jiProfile1.*1000,jiAreaProfile.*1000000);
    title('Area of Cross-Sectional Disk in JI region');
    xlabel('Distance from nozzle (mm)');
    ylabel('Cross Sectional Area (mm^2)');
end
```

```
if showJIvelocity==1
    figure(8);
    jiVel=jiXvalues(:,1).*sqrt(k.*R.*jiXvalues(:,5).*jiTo);
    plot(jiProfile1.*1000,jiVel);
    title('Velocity of Air in JI region')
    xlabel('Distance from nozzle (mm)');
    ylabel('Velocity (m/s)');
end
if showJIpressure==1
    figure(9)
    %hold on;
    jiPressure=jiXvalues(:,3).*jiPo;
    plot(jiProfile1.*1000,(jiPressure./1000)-101);
    title('Disk Pressure');
    xlabel('Distance from nozzle (mm)');
    ylabel('Pressure (kPa)');
end

%Normal Shockwave Calculations
jiMx=jiXvalues(end,1);
jiMy=sqrt((jiMx^2+2/(k-1))/(2*jiMx^2*k/(k-1)-1));
jiPoy=jiPo*(jiMx/jiMy)*((1+jiMy^2*(k-1)/2)/(1+jiMx^2*(k-1)/2))^((k+1)/(2*(k-1)));

%Report final values
fprintf('\nResults for the Jet Impingement Region\n\n');
fprintf('Free Jet Distance:\t\t%5.2f mm\n',jiTopHeight*1000);
fprintf('Impinged Disk Height:\t%5.2f mm\n',jiBottomHeight*1000);
fprintf('Max Diameter:\t\t\t%5.2f mm\n\n',jiMaxDia*1000);
fprintf('-->Assume a shockwave between the free jet area and the impinged disk\n\n');
fprintf('Mach number before shockwave:\t%7.2f \n',jiMx);
fprintf('Velocity before shockwave:\t\t%7.2f
m/s\n',jiXvalues(end,1).*sqrt(k.*R.*jiXvalues(end,5).*jiTo));
fprintf('Po before shockwave:\t\t\t%7.2f kPa\n\n',jiPo/1000);

fprintf('Mach number after shockwave:\t%7.2f \n',jiMy);
fprintf('Po after shockwave:\t\t\t%7.2f kPa\n\n',jiPoy/1000);
fprintf('-------------------------------------------\n');


% FirstDiskRegion
%
% This code will make appropriate calculations for washer shaped area
% outside of the JI region and inside of the outer subsonic region.
%

%Assigned values
fdMinDia=jiMaxDia;
fdMaxDia=.008;      %meters
fdPo=jiPoy;
fdTo=jiTo;
fdRhoZero=fdPo/(R*fdTo);%rho zero ideal gas
```

```
fdMdot=jiMdot;
fdCrArea=fdMdot/((.63394*fdRhoZero)*(1*sqrt(k*R*.83333*fdTo)));

% fd height calculations
fdHeight1=fdCrArea/(pi()*fdMinDia);            %meters--height near center
fdHeightReductionFactor=.68;                   %difference in first and second height
fdHeight2=fdHeightReductionFactor*fdHeight1;   %meters--height at outer edge
 fdRadProfile=fdMinDia/2:.00001:fdMaxDia/2;
fdHeightProfile=fdHeight1-(fdRadProfile-fdMinDia/2)./(fdMaxDia/2-fdMinDia/2).*(fdHeight1-
fdHeight2);
fdAreaProfile=2*pi().*fdRadProfile.*fdHeightProfile;
fdAxA=fdAreaProfile./fdCrArea;
 fdXvalues=tableValues(fdAxA,2,'sps',1:5);

if showFDvelocity==1
    figure(15);
    fdVel=fdXvalues(:,1).*sqrt(k.*R.*fdXvalues(:,5).*fdTo);
    plot(fdRadProfile.*1000,fdVel);
    title('Velocity of Air in first disk region')
    xlabel('Distance from center (mm)');
    ylabel('Velocity (m/s)');
end
if showFDpressure==1
    figure(16)
    %hold on;
    fdPressure=fdXvalues(:,3).*fdPo;
    plot(fdRadProfile.*1000,(fdPressure./1000)-101);
    title('Disk Pressure');
    xlabel('Distance from nozzle (mm)');
    ylabel('Pressure (kPa)');
end

%Normal Shockwave Calculations
fdMx=fdXvalues(end,1);
fdPx=fdXvalues(end,3)*fdPo;
fdMy=sqrt((fdMx^2+2/(k-1))/(2*fdMx^2*k/(k-1)-1));
fdPoy=fdPo*(fdMx/fdMy)*((1+fdMy^2*(k-1)/2)/(1+fdMx^2*(k-1)/2))^((k+1)/(2*(k-1)));
fdPy=fdPx*(1+k*fdMx^2)/(1+k*fdMy^2);

%Report final values
fprintf('\nResults for the first disk region\n\n');
fprintf('Inner Radius:\t\t\t%5.2f mm\n',fdMinDia*1000/2);
fprintf('Outer Radius:\t\t\t%5.2f mm\n',fdMaxDia*1000/2);
fprintf('Beginning Height:\t\t%5.2f mm\n',fdHeight1*1000);
fprintf('Ending Height:\t\t\t%5.2f mm\n\n',fdHeight2*1000);
fprintf('-->Assume a shockwave at the end of the first disk region\n\n');
fprintf('Mach number before shockwave:\t%7.2f \n',fdMx);
fprintf('Velocity before shockwave:\t\t%7.2f
m/s\n',fdXvalues(end,1).*sqrt(k.*R.*fdXvalues(end,5).*fdTo));
fprintf('Po before shockwave:\t\t\t%7.2f kPa\n\n',fdPo/1000);
```

```
fprintf('Mach number after shockwave:\t\t%7.2f \n',fdMy);
fprintf('Static Pressure after shockwave:\t%7.2f kPa\n',fdPy/1000);
fprintf('Po after shockwave:\t\t\t\t%7.2f kPa\n\n',fdPoy/1000);
fprintf('-------------------------------------------\n');

% SecondDiskRegion
%
% This code will make appropriate calculations from the second
% shockwave to the outer edge of the disk.

%Assigned values
sdZ=.0005;      %meters--gap distance or Z parameter
sdMinDia=fdMaxDia;
sdMaxDia=.120;      %meters
sdPo=fdPoy;
sdTo=fdTo;
sdMy=fdMy;

sdRadProfile=sdMinDia/2:.0001:sdMaxDia/2;
sdAreaProfile=2*pi().*sdRadProfile.*sdZ;

sdMdot=fdMdot;
sdExitRho=1.23;
sdExitVel=sdMdot/(sdExitRho*sdAreaProfile(end));
sdExitMach=sdExitVel/(sqrt(k*R*sdTo));
sdCrArea=sdAreaProfile(end)/(tableValues(sdExitMach,1,'sbs',2));

sdAxA=sdAreaProfile./sdCrArea;
sdXvalues=tableValues(sdAxA,2,'sbs',1:5);

if showSDvelocity==1
    figure(20);
    sdVel=sdXvalues(:,1).*sqrt(k.*R.*sdXvalues(:,5).*sdTo);
    plot(sdRadProfile.*1000,sdVel);
    title('Velocity of Air in second disk region')
    xlabel('Distance from center (mm)');
    ylabel('Velocity (m/s)');
end
if showSDpressure==1
    figure(21)
    sdPressure=sdXvalues(:,3).*sdPo;
    plot(sdRadProfile.*1000,(sdPressure./1000)-101);
    title('Second Disk Pressure Distribution');
    xlabel('Distance from nozzle (mm)');
    ylabel('Pressure (kPa)');
end
```

```
%Report final values
fprintf('\nResults for the second disk region\n\n');
fprintf('Inner Radius:\t\t%5.2f mm\n',sdMinDia*1000/2);
fprintf('Outer Radius:\t\t%5.2f mm\n',sdMaxDia*1000/2);
fprintf('Height:\t\t\t\t%5.2f mm\n\n',sdZ*1000);

fprintf('Mach number following shockwave:\t%7.2f \n',sdMy);
fprintf('Velocity following shockwave:\t\t%7.2f m/s\n',sdMy.*sqrt(k.*R.*sdXvalues(1,5).*sdTo));
fprintf('Po following shockwave:\t\t\t%7.2f kPa\n\n',sdPo/1000);

fprintf('Mach number at exit:\t\t\t%7.2f \n',sdXvalues(end,1));
fprintf('Velocity at exit:\t\t\t\t%7.2f
m/s\n',sdXvalues(end,1).*sqrt(k.*R.*sdXvalues(end,5).*sdTo));
fprintf('Static Pressure at exit:\t\t\t%7.2f kPa\n',sdXvalues(end,3)*sdPo/1000);

%combine pressure profiles
 centerRadProfile=0:.0001:(fdRadProfile(1)-.0001);
combinedRadProfile=[centerRadProfile fdRadProfile sdRadProfile];
centerPressureProfile=centerRadProfile.*0+jiPoy;
combinedPressureProfile=[centerPressureProfile (fdXvalues(:,3).*fdPo)'
(sdXvalues(:,3).*sdPo)'];

if showCombinedPressure==1
    figure(25)
    axes('FontSize',18);
    plot(combinedRadProfile.*1000,combinedPressureProfile./1000-101);
    title('Analytical Model Pressure Profile','FontSize',24);
    xlabel('Distance from center (mm)','FontSize',20);
    ylabel('Pressure (kPa)','FontSize',20);
    if showActualProfile==1
        hold on;
        load('PressureData.mat');
        plot(PressureData{4}(:,1),PressureData{4}(:,3),'r');
    end
    axis([0 10 -100 150]);
    set(figure(25),'position',[0 0 1280 1024]);
end

%integrate profile to deterimine net force
clear r dr dP dF;
netForce=0;
for n=1:880
    r=(combinedRadProfile(n+1)+combinedRadProfile(n))/2;
    dr=(combinedRadProfile(n+1)-combinedRadProfile(n));
    dP=((combinedPressureProfile(n+1)+combinedPressureProfile(n))/2-101000);
    dF=2*pi()*r*dr*dP;
    netForce=netForce+dF;
end
fprintf('\nNet Force in Newtons:  %2.4g N\n',netForce);
clear nz* ji* fd* sd* show* k R center*;
```

# APPENDIX E

# EXPERIMENT ONE PRESSURE PROFILES

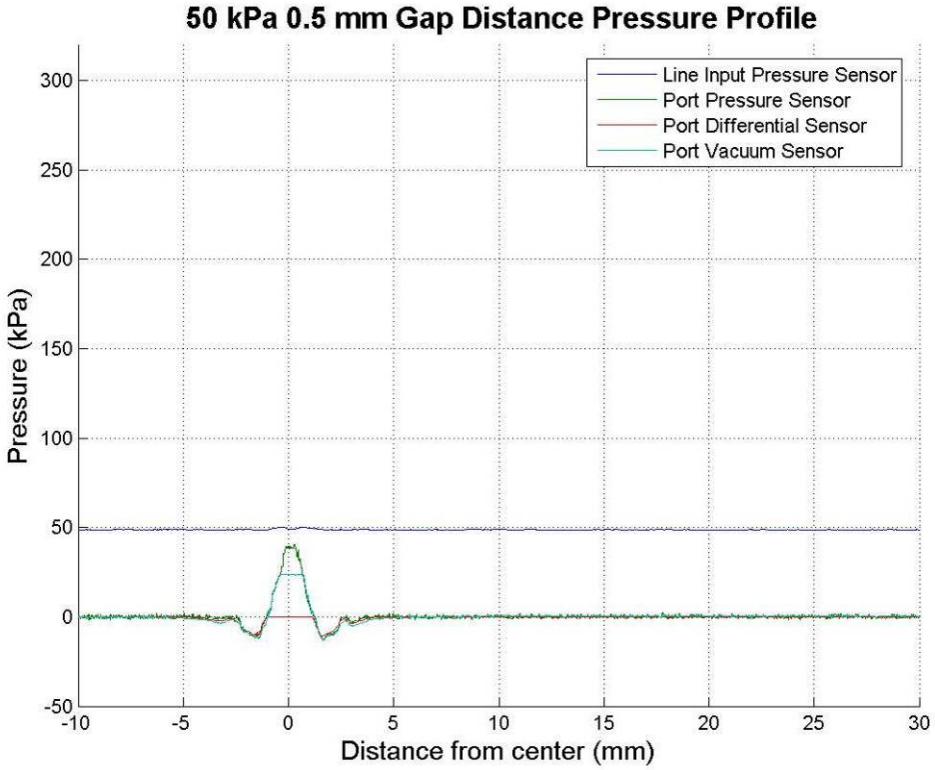
50 kPa 0.5 mm Gap Distance Pressure Profile
Line Input Pressure Sensor
Port Pressure Sensor
Port Differential Sensor
Port Vacuum Sensor
Pressure (kPa)
Distance from center (mm)
300
250
200
150
100
50
0
-50
-10
-5
0
5
10
15
20
25
30

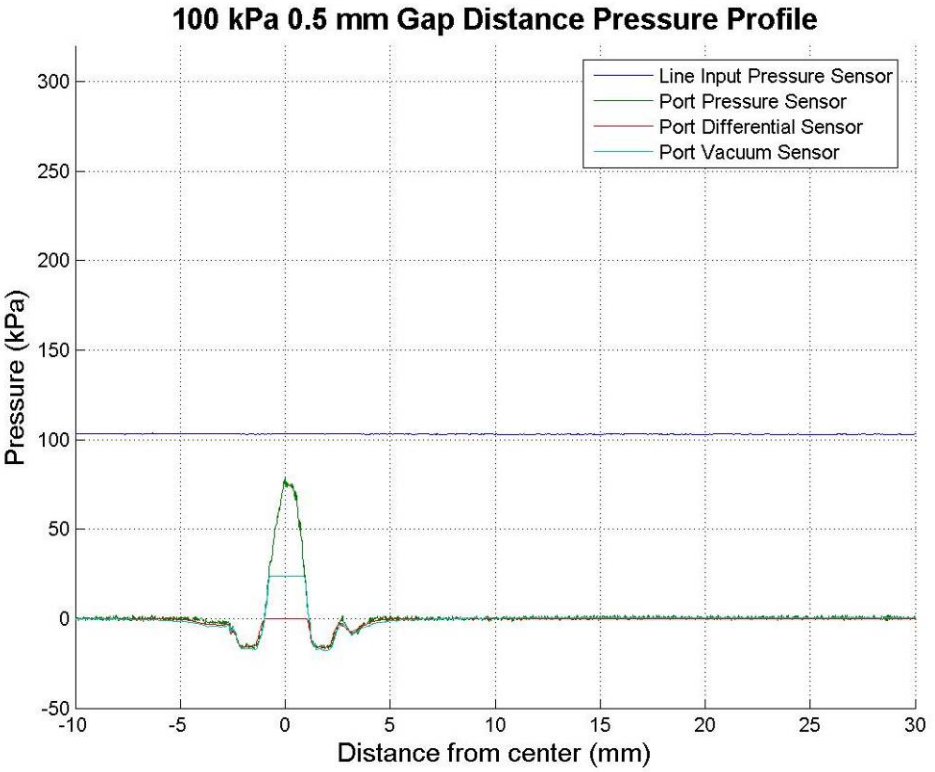
100 kPa 0.5 mm Gap Distance Pressure Profile
Line Input Pressure Sensor
Port Pressure Sensor
Port Differential Sensor
Port Vacuum Sensor
Pressure (kPa)
Distance from center (mm)
300
250
200
150
100
50
0
-50
-10
-5
0
5
10
15
20
25
30

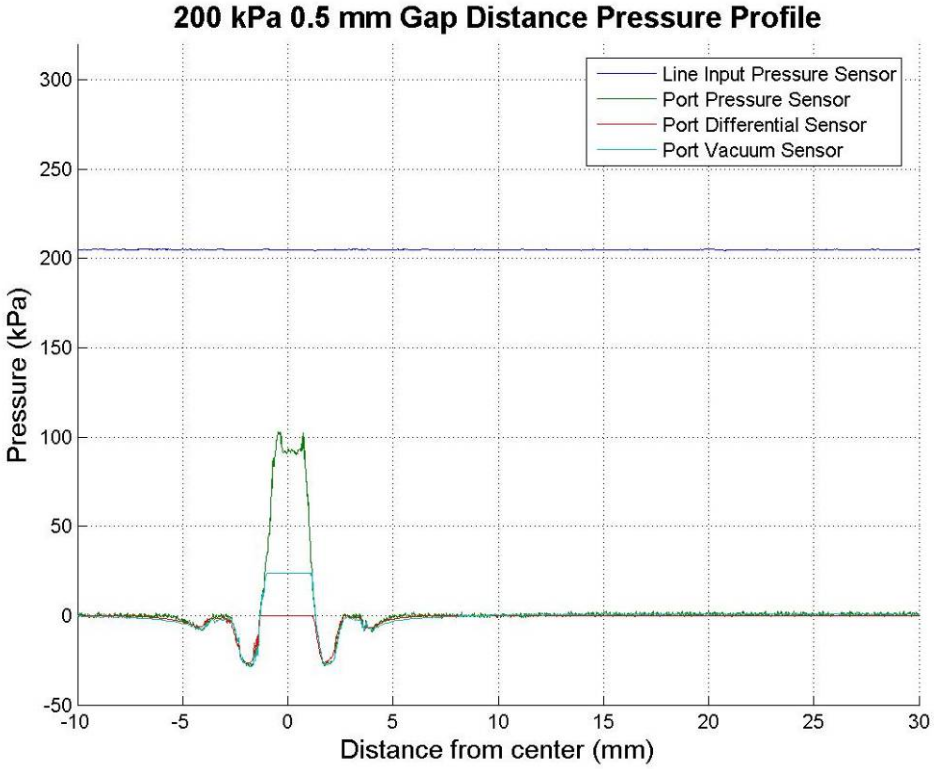
200 kPa 0.5 mm Gap Distance Pressure Profile
Line Input Pressure Sensor
Port Pressure Sensor
Port Differential Sensor
Port Vacuum Sensor
Pressure (kPa)
Distance from center (mm)
300
250
200
150
100
50
0
-50
-10
-5
0
5
10
15
20
25
30

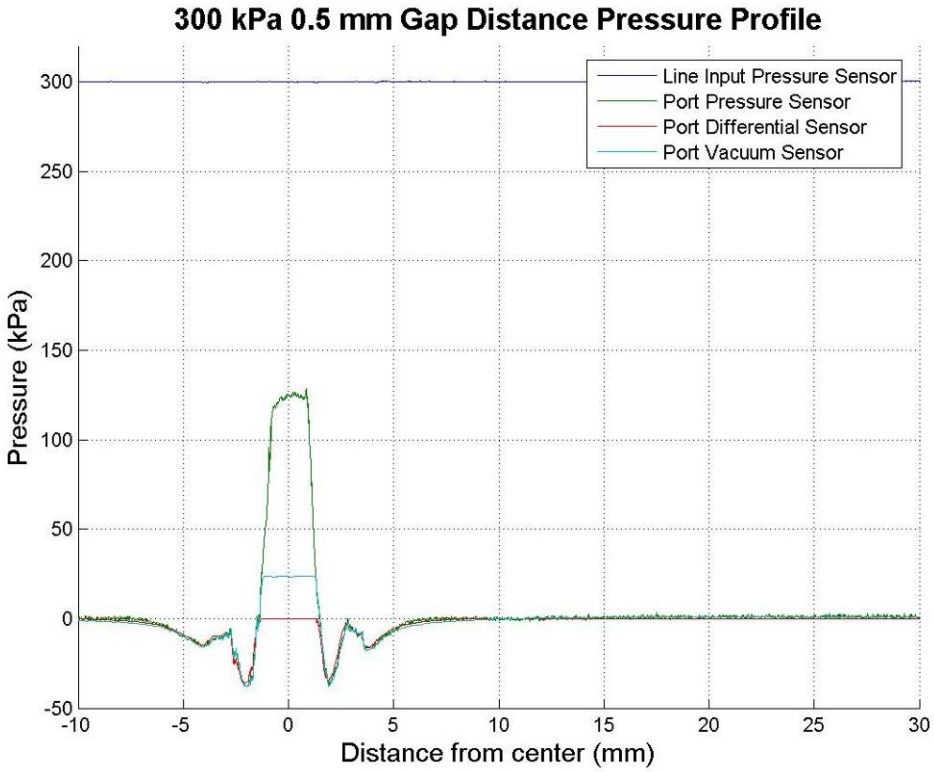
300 kPa 0.5 mm Gap Distance Pressure Profile
Line Input Pressure Sensor
Port Pressure Sensor
Port Differential Sensor
Port Vacuum Sensor
Pressure (kPa)
Distance from center (mm)
300
250
200
150
100
50
0
-50
-10
-5
0
5
10
15
20
25
30

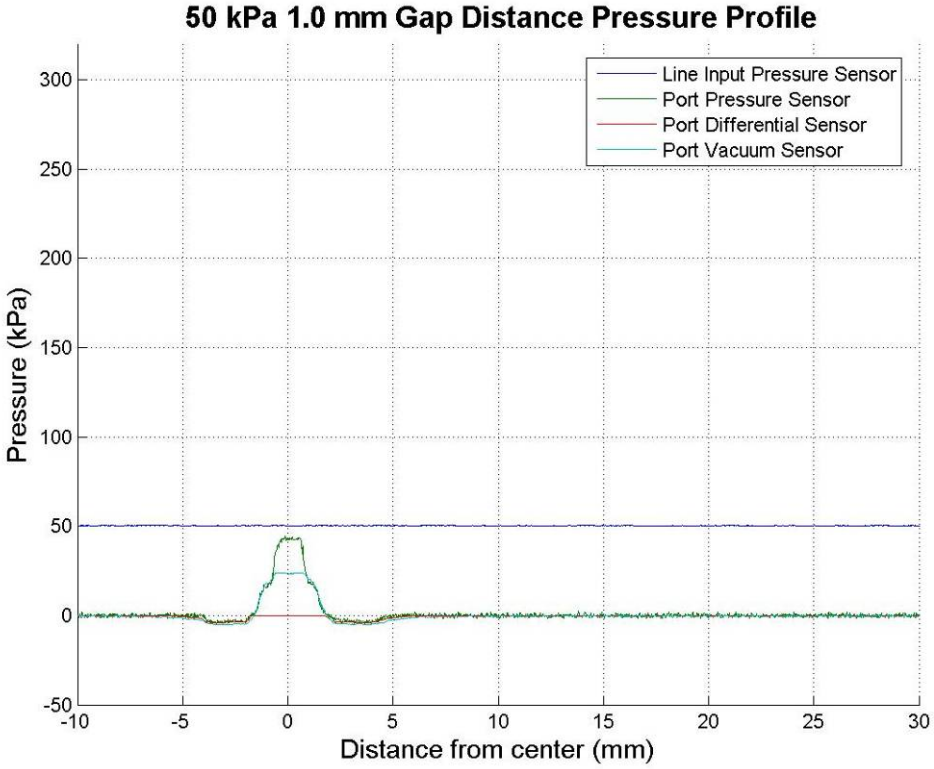
50 kPa 1.0 mm Gap Distance Pressure Profile
Line Input Pressure Sensor
Port Pressure Sensor
Port Differential Sensor
Port Vacuum Sensor
Pressure (kPa)
300
250
200
150
100
50
0
-50
-10
-5
0
5
10
15
20
25
30
Distance from center (mm)

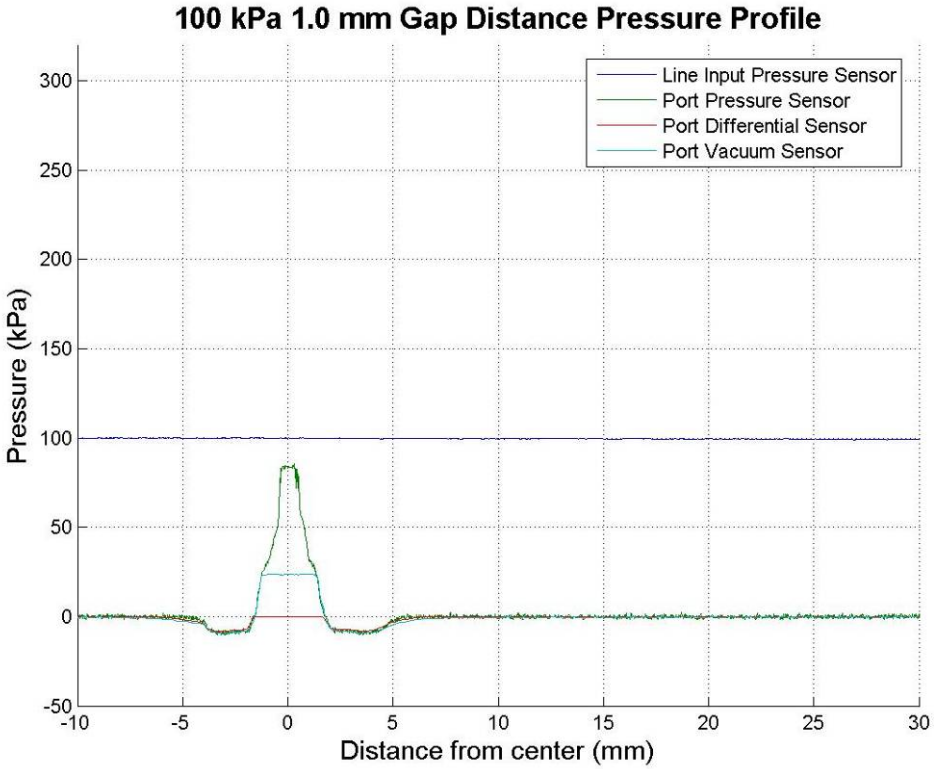
100 kPa 1.0 mm Gap Distance Pressure Profile
Line Input Pressure Sensor
Port Pressure Sensor
Port Differential Sensor
Port Vacuum Sensor
Pressure (kPa)
300
250
200
150
100
50
0
-50
-10
-5
0
5
10
15
20
25
30
Distance from center (mm)

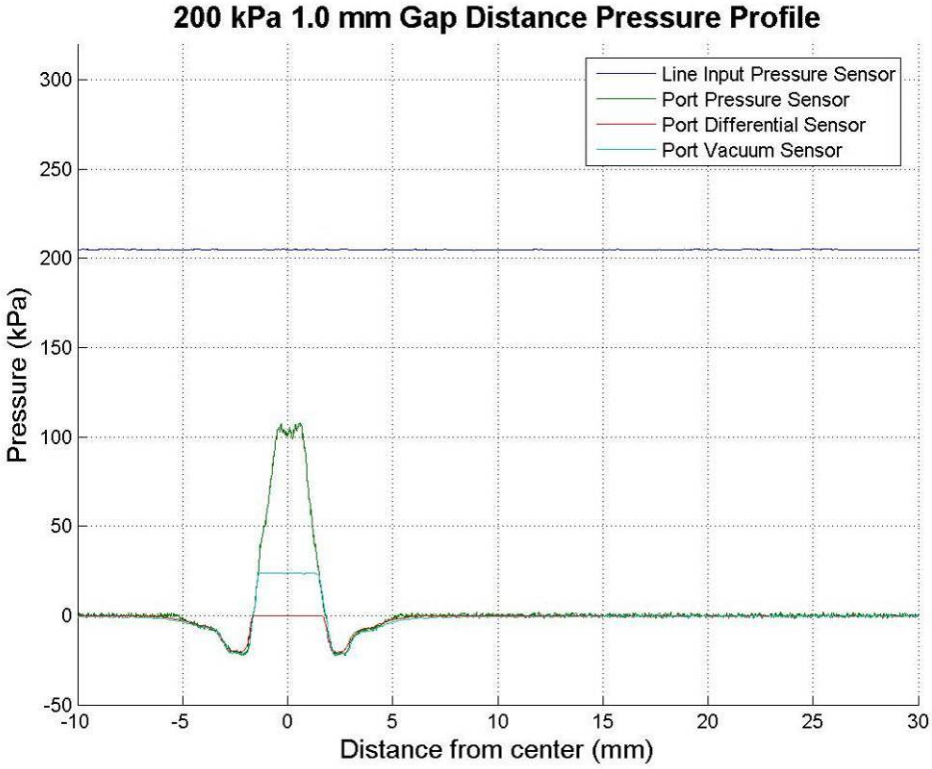
200 kPa 1.0 mm Gap Distance Pressure Profile
Line Input Pressure Sensor
Port Pressure Sensor
Port Differential Sensor
Port Vacuum Sensor
Pressure (kPa)
Distance from center (mm)
300
250
200
150
100
50
0
-50
-10
-5
0
5
10
15
20
25
30

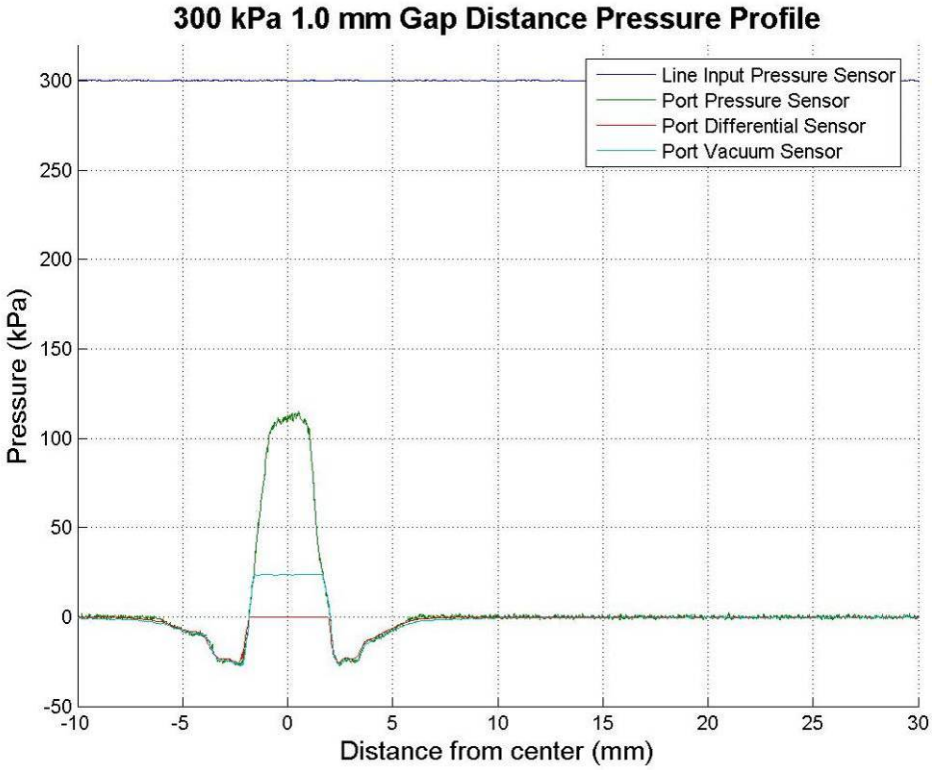
300 kPa 1.0 mm Gap Distance Pressure Profile
Line Input Pressure Sensor
Port Pressure Sensor
Port Differential Sensor
Port Vacuum Sensor
Pressure (kPa)
Distance from center (mm)
300
250
200
150
100
50
0
-50
-10
-5
0
5
10
15
20
25
30

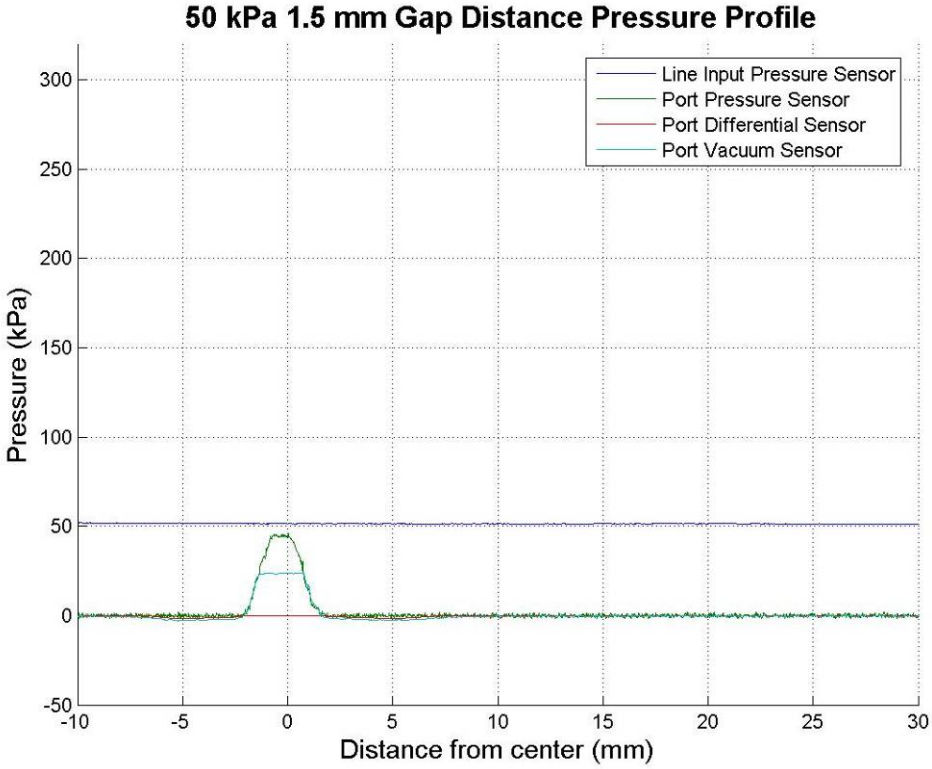
50 kPa 1.5 mm Gap Distance Pressure Profile
Line Input Pressure Sensor
Port Pressure Sensor
Port Differential Sensor
Port Vacuum Sensor
Pressure (kPa)
300
250
200
150
100
50
0
-50
-10
-5
0
5
10
15
20
25
30
Distance from center (mm)

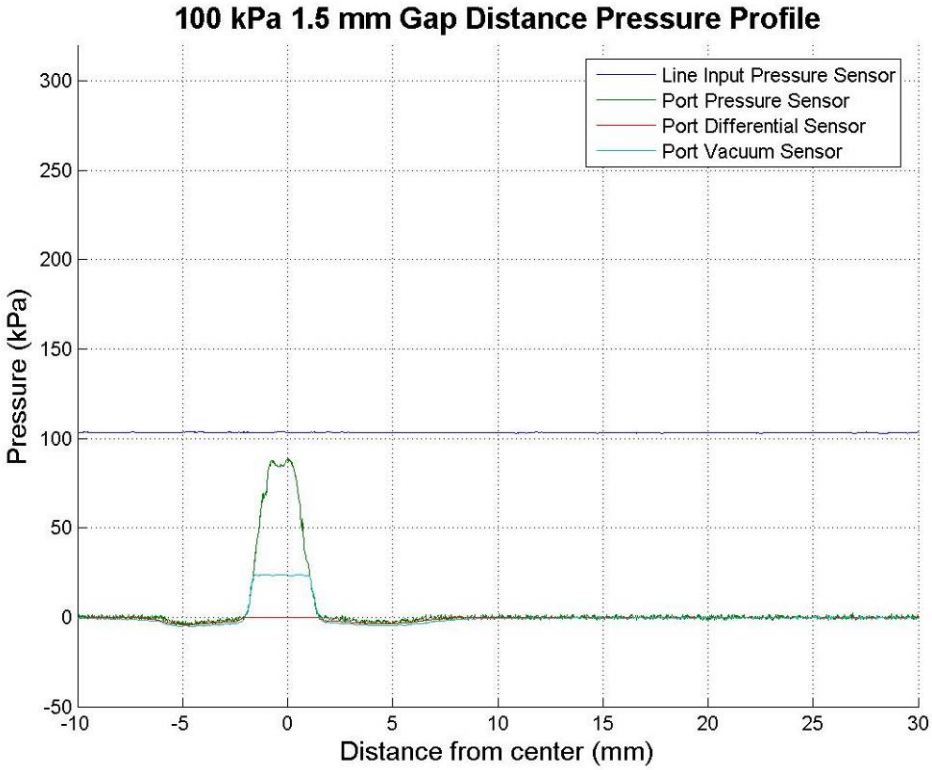
100 kPa 1.5 mm Gap Distance Pressure Profile
Line Input Pressure Sensor
Port Pressure Sensor
Port Differential Sensor
Port Vacuum Sensor
Pressure (kPa)
300
250
200
150
100
50
0
-50
-10
-5
0
5
10
15
20
25
30
Distance from center (mm)

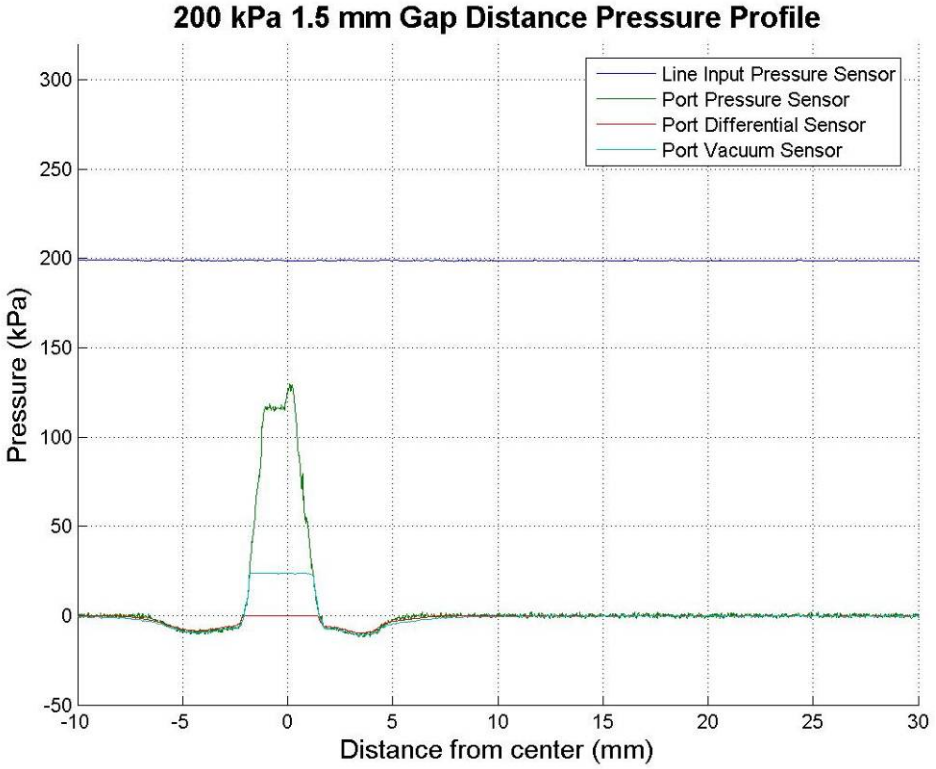
200 kPa 1.5 mm Gap Distance Pressure Profile
Line Input Pressure Sensor
Port Pressure Sensor
Port Differential Sensor
Port Vacuum Sensor
Pressure (kPa)
Distance from center (mm)
300
250
200
150
100
50
0
-50
-10
-5
0
5
10
15
20
25
30

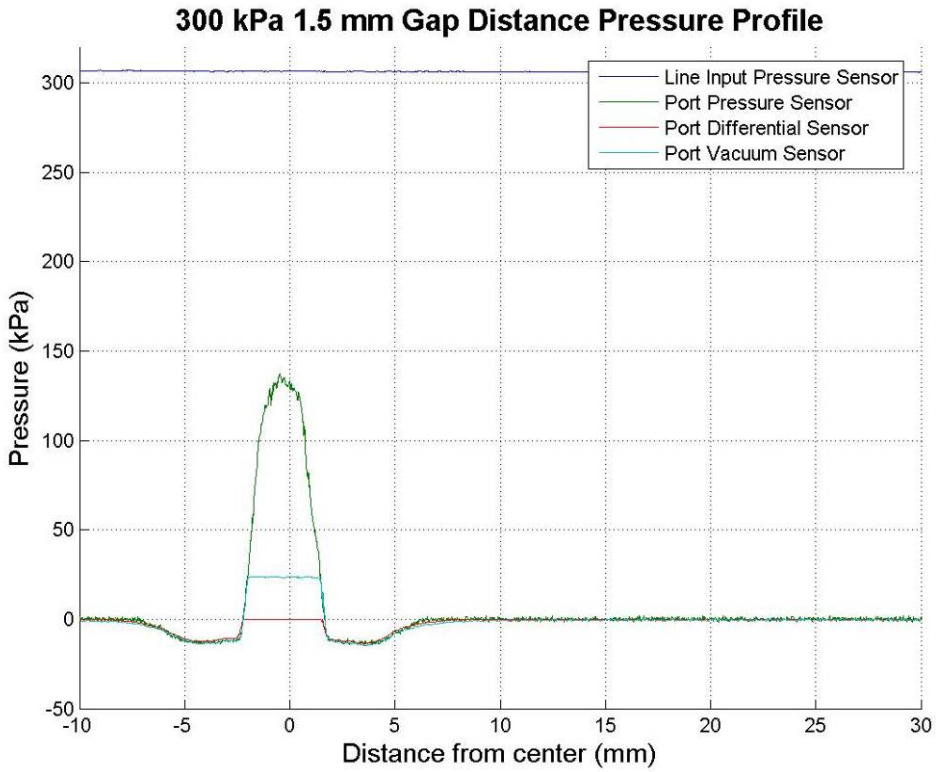
300 kPa 1.5 mm Gap Distance Pressure Profile
Line Input Pressure Sensor
Port Pressure Sensor
Port Differential Sensor
Port Vacuum Sensor
Pressure (kPa)
Distance from center (mm)
300
250
200
150
100
50
0
-50
-10
-5
0
5
10
15
20
25
30

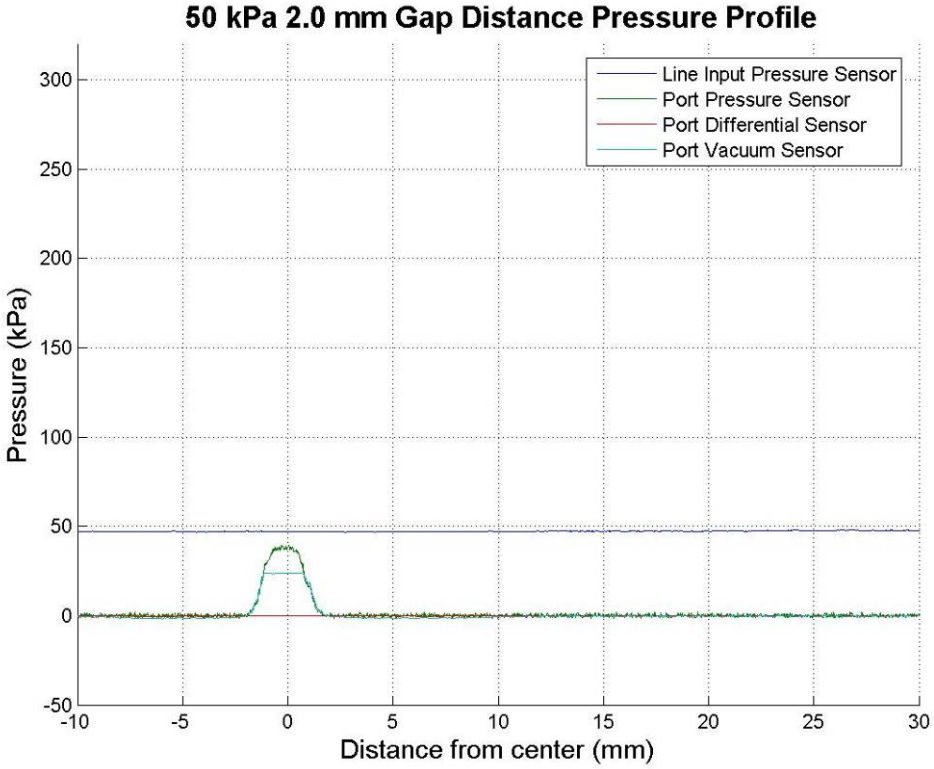
50 kPa 2.0 mm Gap Distance Pressure Profile
Line Input Pressure Sensor
Port Pressure Sensor
Port Differential Sensor
Port Vacuum Sensor
Pressure (kPa)
Distance from center (mm)
300
250
200
150
100
50
0
-50
-10
-5
0
5
10
15
20
25
30

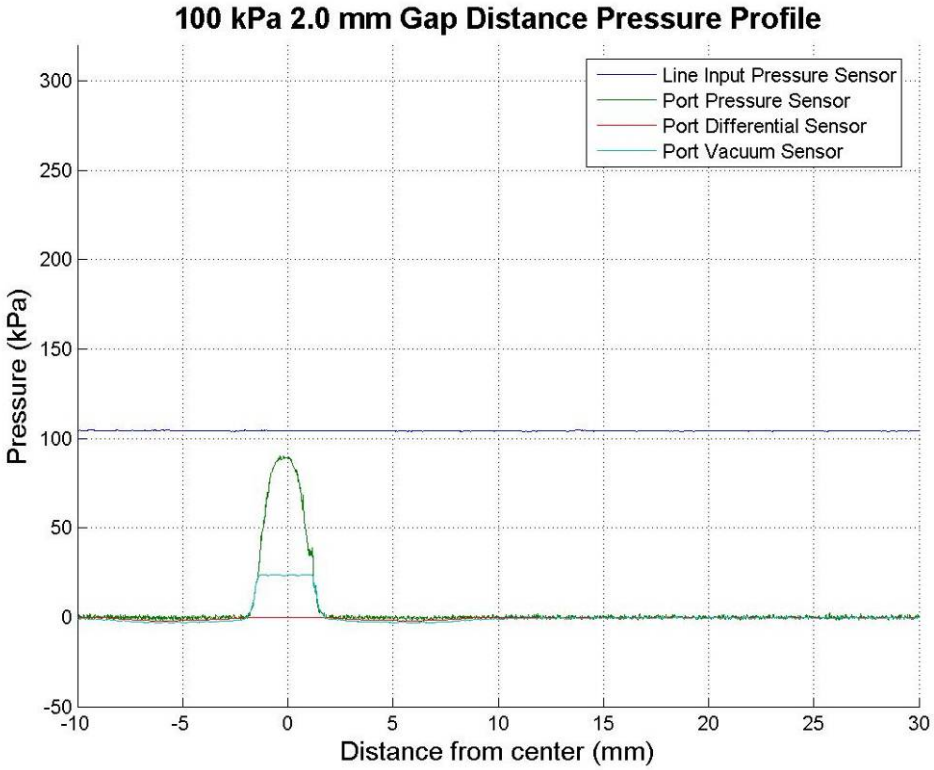
100 kPa 2.0 mm Gap Distance Pressure Profile
Line Input Pressure Sensor
Port Pressure Sensor
Port Differential Sensor
Port Vacuum Sensor
Pressure (kPa)
Distance from center (mm)
300
250
200
150
100
50
0
-50
-10
-5
0
5
10
15
20
25
30

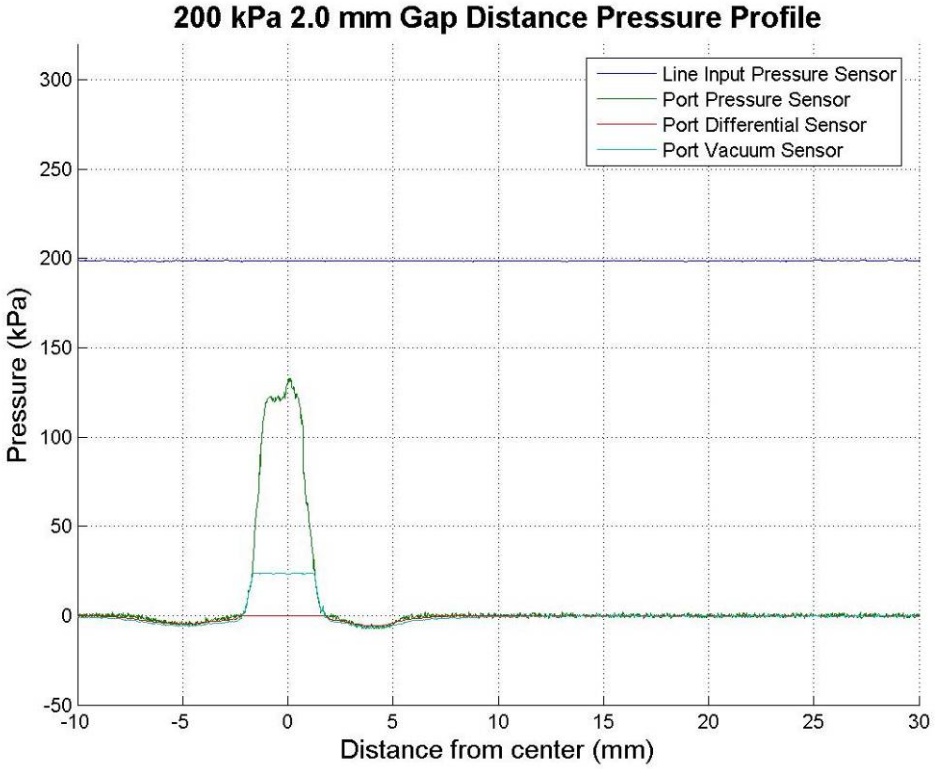
200 kPa 2.0 mm Gap Distance Pressure Profile
Line Input Pressure Sensor
Port Pressure Sensor
Port Differential Sensor
Port Vacuum Sensor
Pressure (kPa)
Distance from center (mm)
300
250
200
150
100
50
0
-50
-10
-5
0
5
10
15
20
25
30

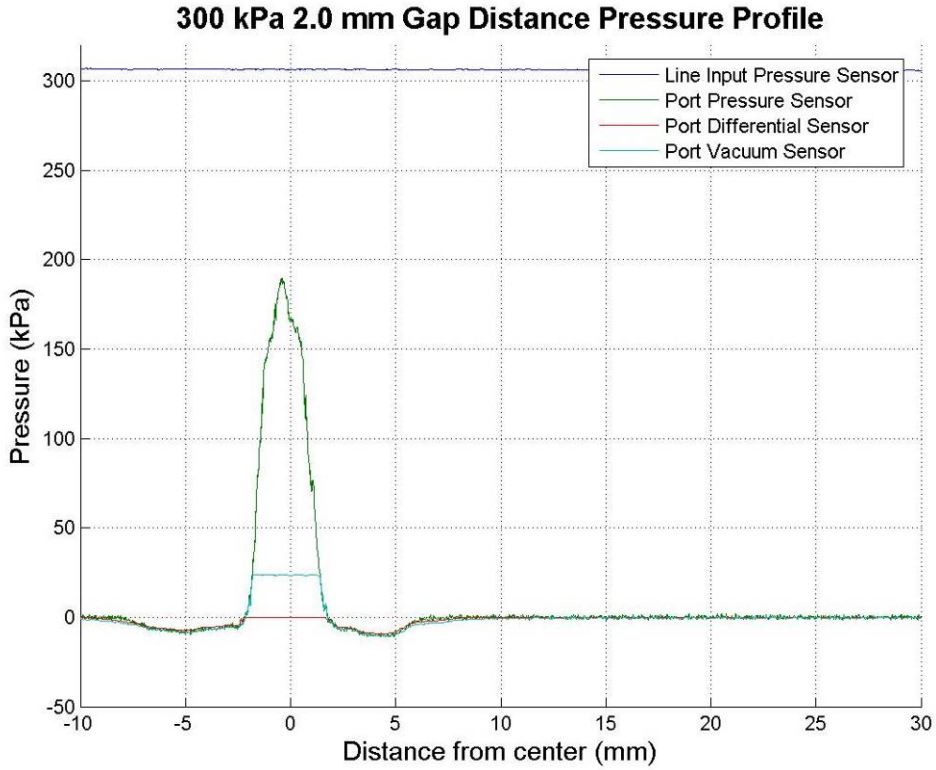
300 kPa 2.0 mm Gap Distance Pressure Profile
Line Input Pressure Sensor
Port Pressure Sensor
Port Differential Sensor
Port Vacuum Sensor
Pressure (kPa)
Distance from center (mm)
300
250
200
150
100
50
0
-50
-10
-5
0
5
10
15
20
25
30

REFERENCES

1. *Industrial Dryers and Ovens from Rostron Drying Systems.* 2005. J. Rostron Engineering Limited. 10 April, 2006. <http://www.rostron.co.uk/>.

2. Bernoulli, Daniel. *Hydrodynamica.* 1738.

3. Munson, Bruce R., Donald F. Yound, & Theodore H. Okiishi. *Fundamentals of Fluid Mechanics.* 4th ed. Hoboken: John Wiley & Sons, 2002.

4. Cengel, Yunus A. and Michael A. Boles. *Thermodynamics: An Engineering Approach*, 4th ed. McGraw-Hill, Boston 2002.

5. Schreier, Stefan. *Compressible Flow*. New York: John Wiley & Sons, Inc., 1982.

6. Srivastava, R.S. *Interaction of Shock Waves.* Boston: Kluwer Academic Publishers, 1994.

7. Handa, Taro, Mitsuharu Masuda, and Kazuyasu Matsuo. "Three-Dimensional Normal Shock-Wave/Boundary-Layer Interaction in a Rectangular Duct." *AIAA Journal*, 43.10 (2005): 2182-2187.

8. Normal, Michael L. and Karl-Heinz A. Winkler. "Supersonic Jets." Los Alamos Science, Spring/Summer (1985): 38-71.

9. Al-aqui, Osama M. A. *Heat Transfer Distribution on the Walls of a Narrow Channel With Jet Impingement and Cross Flow.* Dissertation. The University of Pittsburgh, 2003.

10. Angioletti, M., E. Nino, & G. Ruocco. "CFD Turbulent Modeling of Jet Impingement and Its Validation by Particle Image Velocimetry and Mass Transfer Measurements." *International Journal of Thermal Sciences*, 44 (2005): 349-356.

11. Moreno, O. A., R. H. Katyl, J. D. Jones, and P. A. Moschak. "Mass Transfer of an Impinging Jet Confined Between Parallel Plates." *IBM J. RES. DEVELOP.* 37.2 (1993): 143-155.

12. Baydar, Ertan. "Confined Impinging Air Jet at Low Reynolds Numbers." *Experimental Thermal and Fluid Science*, 19 (1999): 27-33.

13. Chiriac, Victor A., and Alfonso Ortega. "A numerical study of the unsteady flow and heat transfer in a transitional confined slot jet impinging on an isothermal surface." *International Journal of Heat and Mass Transfer*, 45 (2002) 1237–1248.

14. Donaldson, Coleman D. and Richard S. Snedeker. "A Study of Free Jet Impingement. Part 1. Mean Properties of Free and Impinging Jets." *Journal of Fluid Mechanics*, 45.2 (1971): 281-319.

15. Kim, Sung In, and Seung O Park. "Unsteady Flow Simulation of Supersonic Impinging Jet." 41st Aerospace Sciences Meeting and Exhibit, 6-9 Jan. 2003, American Institute of Aeronautics and Astronautics.

# BIOGRAPHICAL INFORMATION

Mr. James Huber holds a Bachelor of Science degree in Physics and a Bachelor of Music degree in Piano Performance from Ouachita Baptist University in Arkadelphia, Arkansas (2004). He has worked as a Graduate Research Assistant at the Automation and Robotics Research Institute (ARRI) of the University of Texas at Arlington since 2005, under the direction of Dr. Raul Fernandez. Mr. Huber has interest in systems integration, industrial automation, and product analysis. He can be reached via email at **jameshuber@gmail.com**.